88

NN-S-529

A Facsimile Report

Reproduced by
UNITED STATES
ATOMIC ENERGY COMMISSION
Division of Technical Information
P.O. Box 62 Oak Ridge, Tennessee 37830

SQT-63933R

NUCLEAR DIVISION

RN-S-0529

To AEC-NASA Space Nuclear Propulsion Office

FINAL REPORT

EVALUATION OF TEST RESULTS FOR
THIN-FILM PRESSURE TRANSDUCER

NERVA Program Contract SNP-1

September 1969

NUCLEAR ROCKET OPERATIONS

AEROJET-GENERAL CORPORATION
SACRAMENTO, CALIFORNIA

RN-S-0529

FINAL REPORT

EVALUATION OF TEST RESULTS FOR
THIN-FILM PRESSURE TRANSDUCER

NERVA Program Contract SNP-1

NUCLEAR ROCKET OPERATIONS

September 1969

CLASSIFICATION CATEGORY

UNCLASSIFIED

T. Smilanich 30 Sept 1969
CLASSIFYING OFFICER DATE

AEROJET-GENERAL CORPORATION
A SUBSIDIARY OF THE GENERAL TIRE & RUBBER COMPANY

DISTRIBUTION OF THIS DOCUMENT IS UNLIMITED

RN-S-0529

FINAL REPORT

EVALUATION OF TEST RESULTS FOR THIN-FILM PRESSURE TRANSDUCER

E. R. Sita

R. V. Evleth, Manager
NERVA Program Office
Nuclear Rocket Operations

PRECEDING PAGE BLANK NOT FILMED

CONTENTS

CONTENTS (continued)

TABLES

FIGURES

FIGURES (continued)

FIGURES (continued)

1. SUMMARY

Four, vapor-deposited, thin-film pressure transducers were irradiated in the ASTR 23/R512 test fixture, that simulated the NERVA engine mounted configuration. The test was conducted to determine the effects of gamma-rate and neutron damage on the performance characteristics of the test transducers, with radiation levels in excess of anticipated full-power engine requirements.

The transducers used in the experiment were Statham Model PA812 (P/N 50390-1). Several secondary experiments were included in the test. These experiments included evaluating the effect of a variable gamma flux on stainless-steel-sheathed magnesium-oxide insulated cables, of the type used with the transducers, and verification of the analytical thermal model of the transducer.

Table 1 summarizes the nuclear test conditions and test results. The data shown for transducer changes are expressed as percent of pretest full-scale output, except for the bridge input and output resistance, which are expressed as a percent of the pretest resistance values. Also shown are pretest values of the transducer temperature coefficient of resistance for correlation purposes.

Analysis of the data indicated that zero shifts caused by gamma-generated gradients were dependent on the TCR value of the transducer. A computer program used to correlate the data also indicated that a 99.4% correlation exists between observed zero shift, gamma rate, and transducer TCR. From this, the following expression was developed:

$$Z = \left[0.00738 + 0.3853\ (\gamma) + 21879\ (TCR) + 22865\ (\gamma \cdot TCR)\right]^2,$$

where Z = zero shift in percent of full scale,

γ = gamma rate in watts/gm(C)

TCR = Temperature coefficient of resistance in ohms per ohm per degree farenheit.

The test data agreed with the calculated expression with a standard deviation of 0.069.

Similarly, a correlation was found to exist between the neutron threshold damage level and the TCR of the transducer. The following expression agrees with the data within the interval of 1 to 10 x 10^{17} n/cm^2 (E > 1.0 mev).

$$\phi t = 1.14 \times 10^{17} e^{6.7 \times 10^4 TCR},$$

where:

ϕt = neutron fluence (E > 1.0 mev) n/cm^2

TCR = temperature coefficient of resistance ohms/ohm/°F

The damage mechanism associated with the TCR and threshold level appears to be caused by a fast-neutron-induced chemical reaction. Changes in other transducer characteristics such as bridge resistance and resistance sensitivity appear to be dependent on the thermal-neutron fluence. However, because of a manufacturing batch tendency of transducer characteristics, and the limited amount of data available, interpretation of the results are inconclusive.

Generally, radiation induced changes in transducer characteristics are small. Significant changes are the gamma-induced transient zero shift and the neutron threshold damage level. Both can be optimized by proper selection of the transducer TCR value.

TABLE 1

TRANSDUCER CHARACTERISTICS

Item	Characteristic	Units	Transducer S/N 47	50	63	61
1	TCR (pretest values)	Ω/Ω-°F	24 x 10^{-6}	16 x 10^{-6}	6 x 10^{-6}	2 x 10^{-6}
2	(E > 1.0 Mev) FAST (neutron fluence)	n/cm^2	5.8 x 10^{17}	4.9 x 10^{17}	5.6 x 10^{17}	5.1 x 10^{17}
3	(E < 0.48 ev) Thermal (neutron fluence)	$(nV_o)t$	7.4 x 10^{17}	7.4 x 10^{17}	8.6 x 10^{17}	6.7 x 10^{17}
4	Threshold damge level	n/cm^2	5.7 x 10^{17}	3.3 x 10^{17}	1.7 x 10^{17}	1.3 x 10^{17}
5	(2 watts/gm(C)) Gamma zero shift	% F.S.	5.8	3.5	1.4	0.8
6	Bridge resistance (input) (output)	% Pretest	0.39 0.39	0.38 0.38	0.21 0.19	- 0.14
7	Nonlinearity	% F.S.	-0.19	-0.10	-0.09	-0.09
8	Sensitivity	% F.S.	0.28	0	0.60	0.36
9	Zero set	% F.S.	-6.85	-16.50	-2.61	-1.91
10	(@ 2.0 w/gm(C)) Insulation resistance	Megohms	1.5	1.8	4.7	5.5

II. INTRODUCTION

A. PURPOSE OF EXPERIMENT

Four Statham Model PA812 (P/N 50390-1) thin-film pressure transducers were irradiated in the in-pile tube of the Aerospace Systems Test Reactor (ASTR) at General Dynamics, Fort Worth, Texas (GD/FW) on 21 August 1967. The 23/R512A test was a development irradiation test of a candidate pressure transducer type, to be used to monitor the nozzle chamber pressure of the NERVA engine control system. Statham Model PA812 (P/N 50390-1) is a redesign of Statham Model PA 812 (P/N 16647) that was previously tested in the Plumbrook Test Reactor and on the NRX-A5 engine.

The primary purpose of this experiment was to determine qualitatively, the performance characteristics of the redesigned candidate NERVA flush-mounted pressure transudcer. The test was conducted in a simulated engine-mounted configuration, with radiation and temperature environments in excess of anticipated full-power engine requirements.

Specific experimental objectives of the test were:

1. Evaluate the effects of a variable gamma-flux environment on the performance characteristics of the flush-mounted controls pressure transducer with respect to radiation-induced internal-temperature gradients in a nuclear-heating environment of 0 to 3.0 watts per gram carbon.

2. Determine the temperature environment extremes consistent with satisfactory operation of the pressure transducers.

3. Evaluate the effects of the integrated fast-neutron environment on the performance characteristics of the pressure transducers.

Several secondary experiments were incorporated into the test fixture. The objectives of these secondary experiments were:

1. Evaluate the effects of the variable gamma-flux environment on the stainless-steel-sheathed cables used with the transducers with respect to:

   a. Cable shunting
   b. Radiation-induced photo currents
   c. Conductor polarity orientation.

2. Provide data for verification of the thermal analytical model of the flush-mounted transducer.

B. DESCRIPTION OF TEST ITEMS

To meet the experimental objectives of the test, the items tested consisted of four active pressure transducers, two instrumented transducers, and three simulated transducer systems. In addition, two specially constructed thermocouple cables with internal ungrounded sensor junctions were incorporated into the test fixture.

The cable conductor temperature data were added to obtain correlating data for a similar cable test conducted in conjunction with the NRX-A6 test and are not important to the pressure-transducer test. The test components are tabulated in Table 2 together with their respective locations on the fixture.

1. Active Transducers

The Statham Model PA812 (P/N 50390-1) pressure transducer is a full active bridge, vapor-deposited, thin-film, strain-gage type, with a nominal 1500-ohm bridge resistance. The model is a generic descendant of the Statham Model PA810TC pressure transducers tested in the GTR-15 Irradiation

TABLE 2

TEST COMPONENTS

Test Item	Test Fixture Location	S/N	Resistance (ohms)	Range (psi)
Statham Model PA812	Boss 1	-	-	Instrumented
Statham Model PA812	Boss 2	61	1500	0-750
Statham Model PA812	Boss 3	47	1500	0-750
Statham Model PA812	Boss 4	-	-	Instrumented
Statham Model PA812	Boss 5	63	1500	0-750
Statham Model PA812	Boss 6	50	1500	0-750
Simulated transducer cable assembly	Bottom	1	1500	Inactive
Simulated transducer cable assembly	Bottom	2	1500	Inactive
Simulated transducer cable assembly	Bottom	3	1500	Inactive
Thermocouple cable	Bottom	A	-	
Thermocouple cable	Bottom	B	-	

Test in December 1964 (Reference 1). From the results of the GTR-15 test, Model PA812 (P/N 16647) evolved and was tested on the MRX-A5 reactor test and in the Plumbrook Radiation Facility. The results of these tests are reported in References 2 and 3, respectively. The results of both tests indicated that serious gamma-heating problems were experienced with the use of electrical connectors attached to the transducer housing. In addition, test results and thermal analysis indicated that the internal design of the transducer was inadequate for the efficient removal of gamma-generated heat.

The transducer was redesigned, with significant reduction in the height and mass of the unit, by replacing the electrical connector with integral, stainless-steel sheathed, magnesium-oxide insulated cable and by reducing the length of the threaded portion of the transducer body. Internal heat conduction paths were improved by machining the internal header into the one-piece transducer body and relocating the header closer to the threaded portion of the transducer body. A major evolutionary design change in the diaphragm and bridge configuration was made concurrently by the manufacturer that significantly improved transducer linearity and performance by providing mechanical, electrical and thermal symmetry in the sensing-element design. A comparison of the earlier and redesigned transducer models is shown in Figure 1.

The transducer sensing element is a four-active-arm Wheatstone bridge configuration that utilizes a thin-film, metallic strain gage, vapor deposited onto a similarly deposited ceramic substrate. Two 2-conductor, stainless-steel sheathed, magnesium-oxide insulated cables are incorporated as an integral part of the design. Copper and nickel-clad copper conductors were used in each cable for polarity identification, with the nickel-clad conductor signifying the positive lead in both the input and output cables.

2. Instrumented Transducers

Two Statham Model PA812 transducers were disassembled and chromel-alumel thermocouples were welded to the diaphragms. In one of the

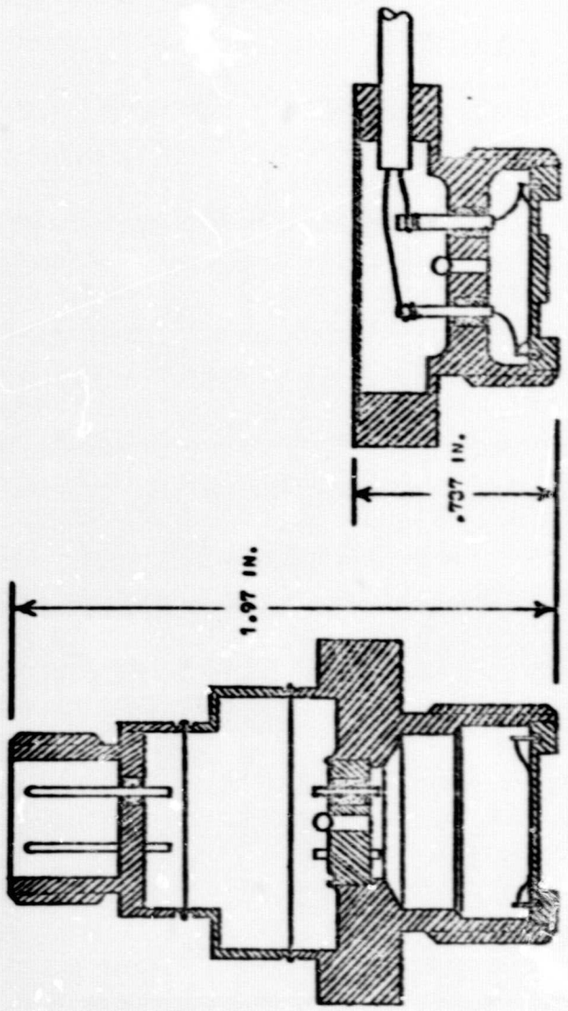

P/N 50390-1

P/N 16647

Figure 1 - Comparison of Statham Model PA812 Pressure Transducers

transducers, a thermocouple was installed in the center of and at the edge of the diaphragm. In the other, only the center was instrumented.

The instrumented transducers were incorporated into the test fixture to obtain temperature-gradient data from the center of the diaphragm to the heat sink and across the diaphragm. The active strain-gage materials used on the diaphragm are stable with temperature up to approximately 1060°R. At temperatures in excess of 1060°R, material changes occur in the alloyed strain material that result in catastrophic zero shifts. Gradient data at various heating rates are needed to define the maximum heat-sink temperatures. Temperature gradients across the diaphragm can produce an output error resulting from a temperature-induced resistive unbalance of the bridge. Analytical thermal and electrical studies indicate that small gradients are expected but that the resultant error can be significant. However, temperature gradient data are required to verify the analytical results.

3. Simulated Transducers

Several methods were employed to determine and separate the contribution of irradiated MgO insulated metal-sheathed cables on the pressure measurement system performance. In addition to monitoring the active transducer and cable parameters, several simulated transducer systems were incorporated where only the cables were exposed to the radiation environment. In normal operation, the transducer input and output leads are contained in separate cables. The simulated systems were designed to investigate radiation effects on:

a. The normal system.

b. The reversed system where the positive input and output, and negative input and output leads, are in respective cables.

c. Input cable only.

d. Output cable only.

A schematic showing the relationship of the input and output lead configuration for each system is shown in Figure 2.

The transducers were simulated in each system with resistors of unequal value connected in a full Wheatstone bridge configuration to provide a simulated full-scale output millivolt signal. The simulated bridges were located in the control panel in the control room. The cables used in each system were the same type used with the active transducers and contained copper and nickel-clad copper conductors for polarity identification.

The reversed system configuration was obtained by the use of reversing switches located within the control panel. For clarity, these switches are not shown in Figure 2.

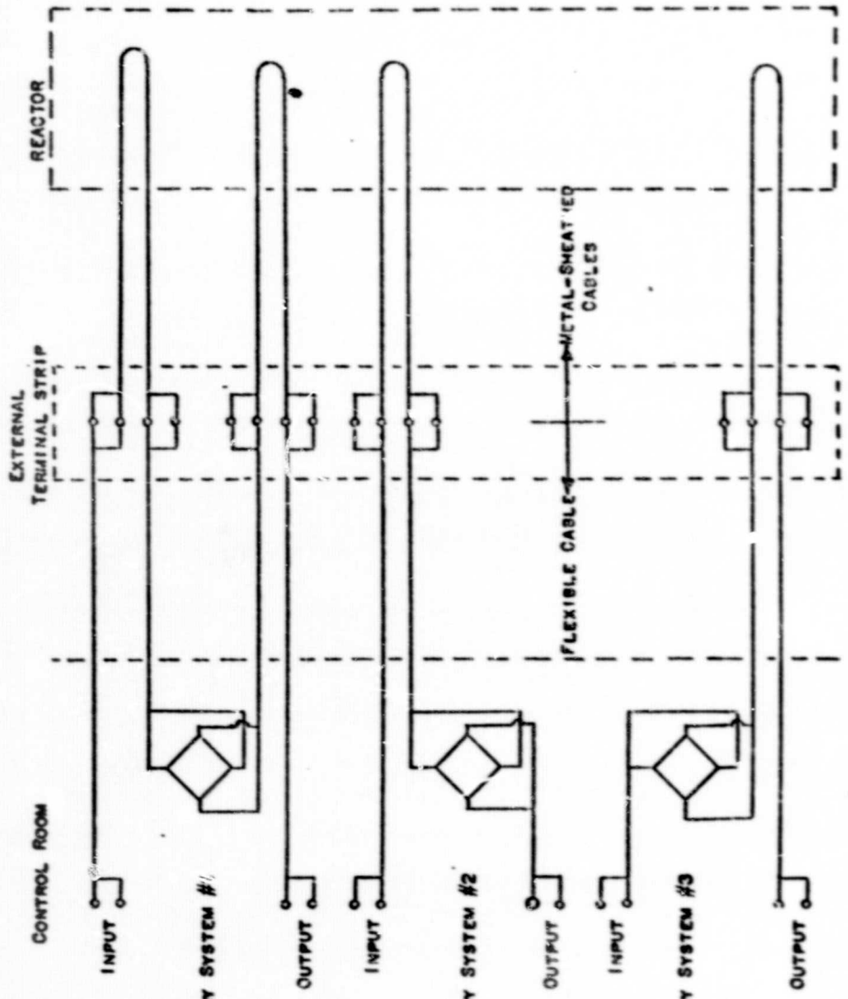

Figure 2 - Simulated Transducer Configuration

III. TEST SETUP

Detailed specifications for the assembly and checkout of the test items and associated hardware, as well as the test specifications and procedures, are set forth in Reference 4.

A. TEST FACILITY

The ASTR is a heterogeneous, enriched, light-water-moderated and cooled, thermal reactor. The design is roughly a right circular cylinder 76-in. long and 34 in. in diameter. The core is composed of 29 fuel elements, containing 155 gm each of U_{235}, four elements containing 104 gm each of U_{235}, and three control-rod assemblies. The fuel elements are arranged in a 7 x 7 matrix with the three elements in each corner missing. Aluminum grid plates support the core at each end.

The ASTR in-pile tube, located in core-lattice position 0-3, has a 4-in. OD and a nominal wall thickness of 0.125 in. and is constructed of 304 stainless steel. The bottom is welded closed with a 0.125-in. thick plate and the top closure is made with a Marmon V-clamp with an O-ring seal. The tube is held in the reactor by an O-ring flange and two captive bolts. The in-pile tube installed in the reactor is shown in Figures 3 and 4.

The tube extends 1.5 ft through the core into the aft plenum chamber. The upper, or forward, end of the tube extends 10 in. through the pressure plate. An aluminum extension tube 80-in. long was attached at the upper end by means of a Marmon clamp. The extension tube had two 1-in. vent lines that looped above the waterline and terminated 3 ft under water. A relief valve on each vent line provided additional protection against entry of water into the tube.

For these experiments, the ASTR was in the fully-lowered position with the forward end up. The extension tube extended upward and terminated a

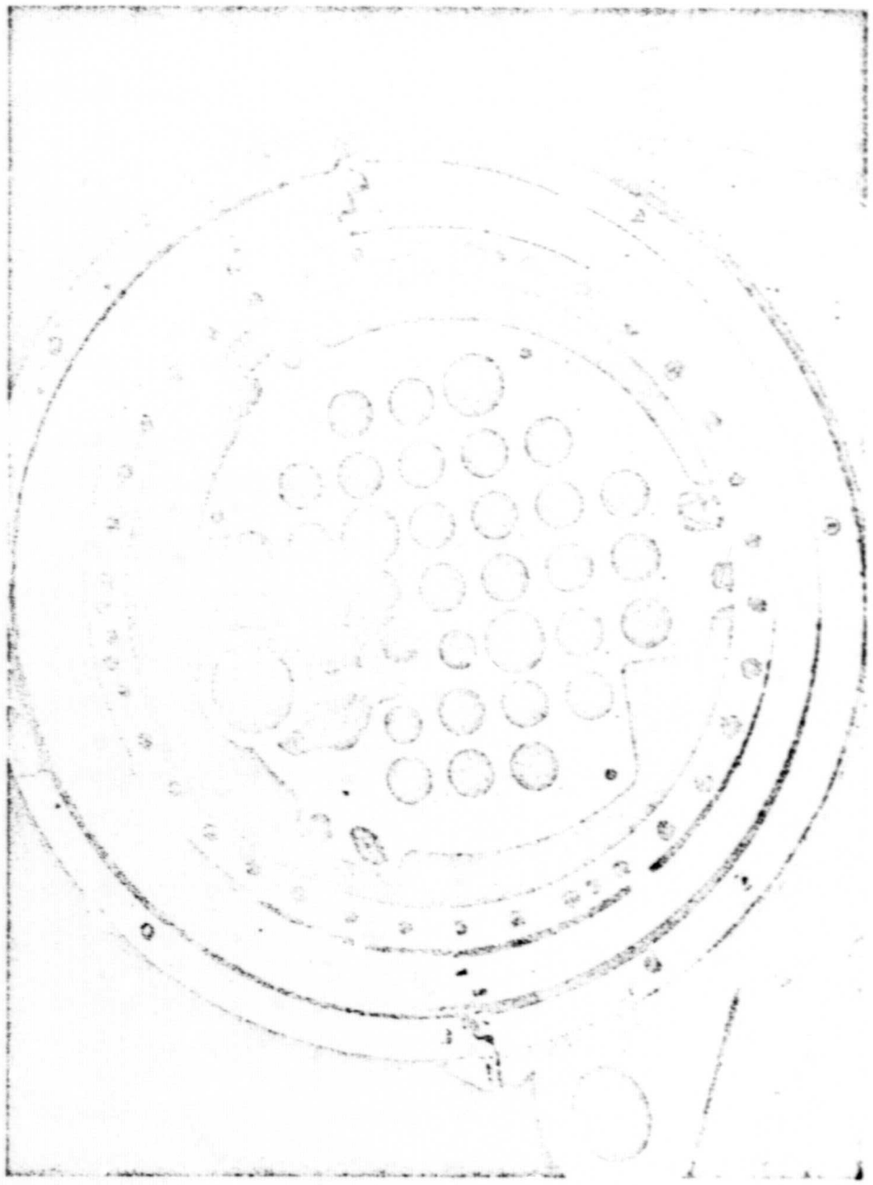

Figure 3 - In-Pile Tube Inserted in Reactor Grid Plate

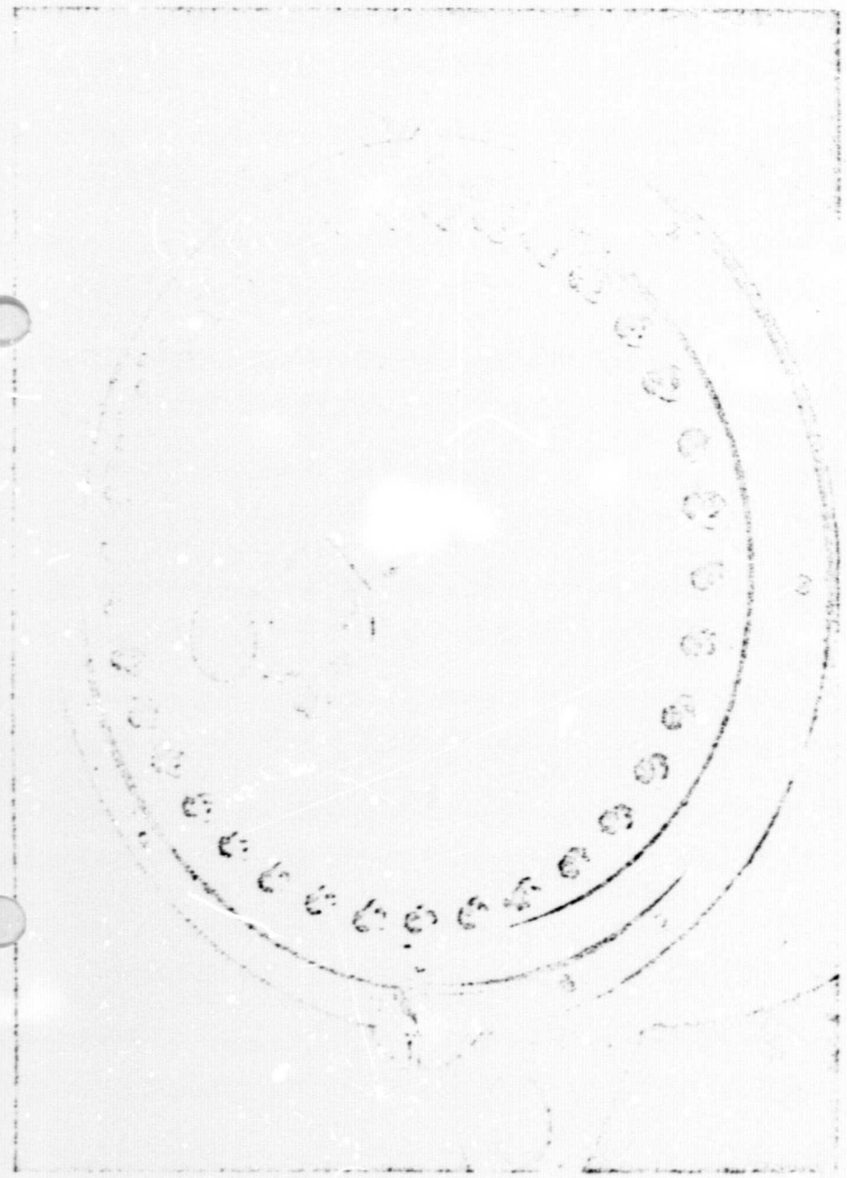

Figure 4 - In-Pile Tube Extending Through Forward Pressure Plate

few inches above the water level. The test fixture was installed in the in-pile tube and lowered into the core.

B. TEST ARRANGEMENT

1. Test Fixture

The test fixture design for irradiation test 23/R512A was based on the results of an extensive thermal analysis performed to establish the temperature control requirements for the test. The results of the thermal analysis are presented in Appendix A. The fixture, shown in Figure 5, consisted of an aluminum manifold with six transducer mounting bosses used on the NERVA Technology engine. The GN_2 coolant inlet line was a 1.38-in. aluminum tube welded to the hollow core of the manifold. After passing beneath the transducer bosses, the coolant flow was reversed in the fixture end cap, exiting from the fixture through two 1-in. aluminum tubes. Penetrations for thermocouples were made into five of the six transducer bosses. Pressurization for the six bosses was provided by a 1/4-in.-dia tube.

For ease of handling during the assembly, the length of coolant inlet and outlet tubes were shortened to approximately 7 ft until all of the test transducers, simulated cables, and thermocouple instrumentation were assembled in the fixture and the functional check was completed. After assembly and checkout, extensions were welded to the inlet and outlet tubes so that the final length of the fixture was approximately 12 ft. This was necessary to span the distance from the top of the ASTR water pool to the center of the core.

After fabrication, the fixture was assembled in the NRO Engineering Laboratory. The first attempt at installing the transducers was unsuccessful, due to incorrect alignment of the transducer integral leads relative to the fixture. Alignment of the integral leads was quite critical because of the confined space of the in-pile tube, and to ensure that the

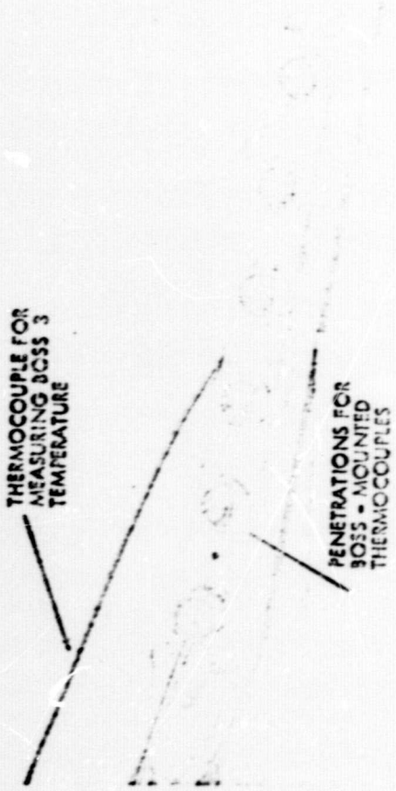

Figure 5 - Test Fixture Manifold

leads contacted the coolant tubes in the shortest length possible. The fixture transducer bosses were remachined to reposition the individual starting threads. In addition, it was necessary to use selected metallic K-seals to achieve the proper transducer alignment at the final assembly.

Following the assembly of the transducers into the bosses, the remaining boss and surface thermocouples and simulated transducer cables were attached to the fixture as shown in Figures 6 and 7. The simulated cables, and the two special cables with internal junction thermocouples, were attached to the bottom of the test fixture coolant manifold with thin-metal tabs resistance welded to the fixture. Thermocouples were installed in each of the bosses except No. 6 and a surface thermocouple was resistance welded to the hex head of each transducer body. The assembled test fixture with welded extensions and the secured electrical cables is shown in Figure 8.

2. Cooling System

The test fixture was cooled by GN_2 supplied by an evaporator fed from a 26,000 gal LN_2 storage tank. The evaporator utilized water as a heat source in a single-pass parallel-flow unit 44-ft long. Liquid nitrogen can be supplied to the evaporator either by storage tank pressure or, for larger flows, by a centrifugal pump rated at 100 gpm at 625 psig above storage tank vapor pressure.

The discharge of the pump is modulated by two pneumatically positioned 1-in. cryogenic valves that either route the flow through the evaporator or divert all, or part, of the flow back to the storage tank. The water flow through the evaporator is controlled by a remotely positioned 3-in. valve. A normally open precool vent was located at the output of the evaporator.

The temperature of the test fixture was monitored and controlled utilizing a Bristol circular-chart recorder-controller. The flow of the GN_2 coolant through the fixture was controlled manually.

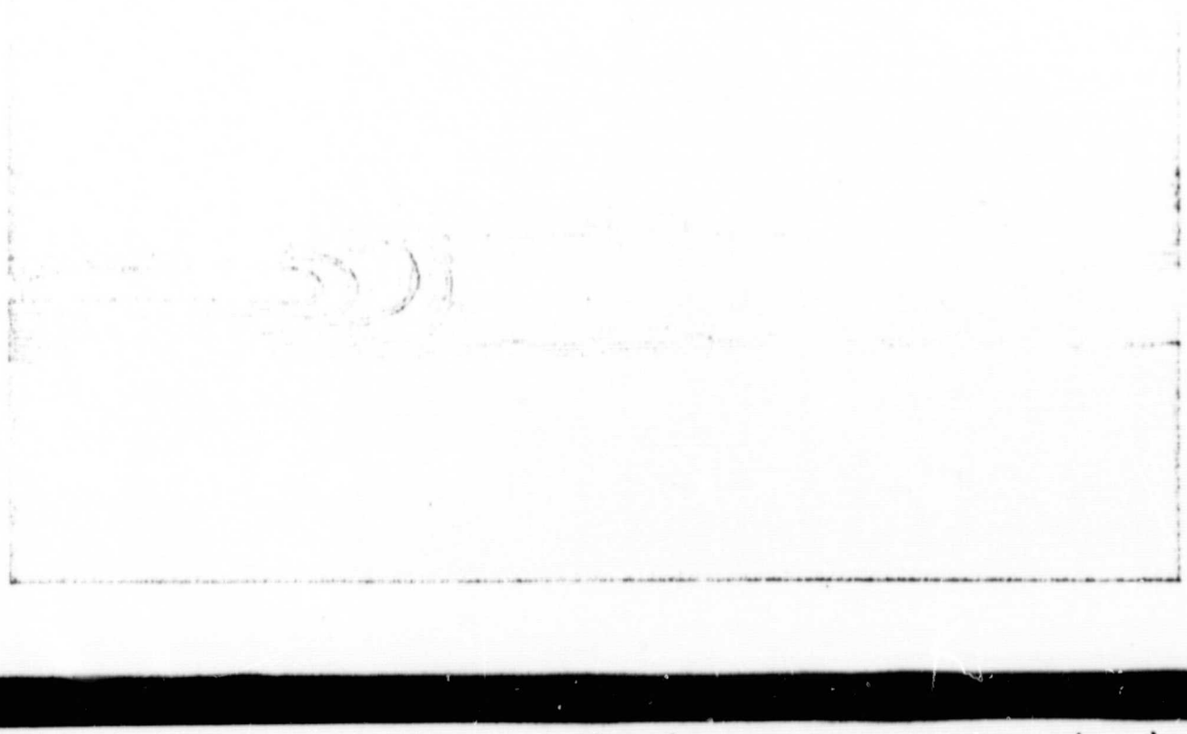

Figure 7 - Installation of Shielded Transducer Cables and Thermocouple Cables

Figure 6 - Installation of Pressure Transducers and Thermocouples

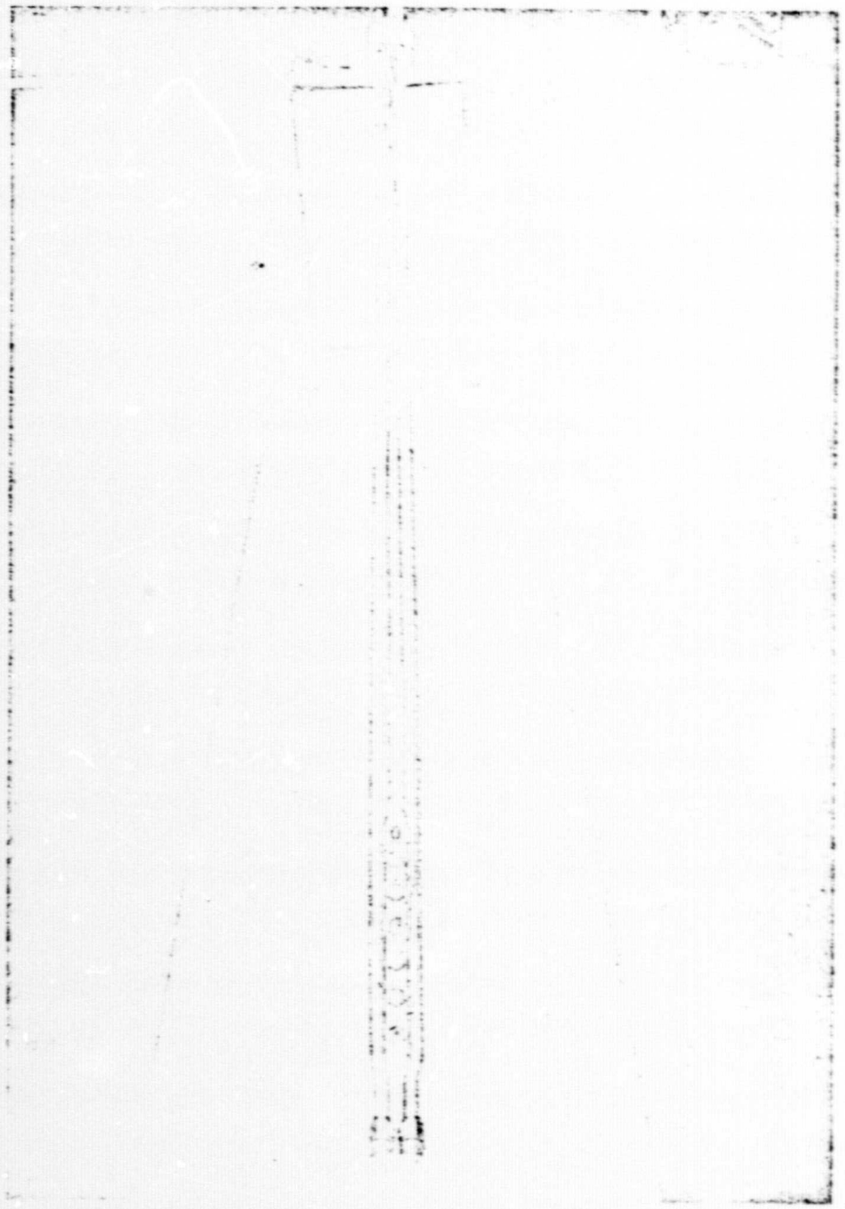

Figure 8 - Completed Test Fixture Assembly

The cooling system, its controls and instrumentation are shown schematically in Figure 9. Additional instrumentation was provided to monitor the LN_2 and water flow rates as well as system pressures and temperatures throughout the test.

C. DATA ACQUISITION

Two data systems were employed during the test. The bulk of the data was obtained by use of an automated system. Some pre and posttest data were obtained with a manual data system. With either data system, insulation resistance could be determined by measuring the leakage current with a Hewlett-Packard 412-B multimeter with 45 vdc applied with a battery. The output voltage and bridge resistance of each simulated bridge were measured manually with a Dana digital voltmeter and a Wheatstone bridge, respectively. The insulation resistance measurements were made with a Weston 50 vdc megohmeter.

1. Automated Data System

An AGC fabricated test-channel selector was used to perform all of the switching functions, through relays, on command from the Dynec Data System. The Dynec then scanned the measurements and recorded the outputs on printed and punched paper tape. Operating on a 3 sec sample period, the data system completed a data cycle of 40 channels in approximately 45 sec. Pressure was applied to the test transducers in successive steps of 0, 250, 500, and 750 psig by a Wiancko Digital Pressure Generator, Model Q-2738. A complete data cycle was obtained for each pressure step and also for the special test with zero applied voltage. The channel identification for a data cycle is listed in Table 3. A block diagram of the automated Dynec Data System is shown in Figure 10. The test channel selector is detailed in Figure 11.

2. Manual Data System

The manual data system, used during the preliminary checkout measurements and for some of the postirradiation measurements, employed a

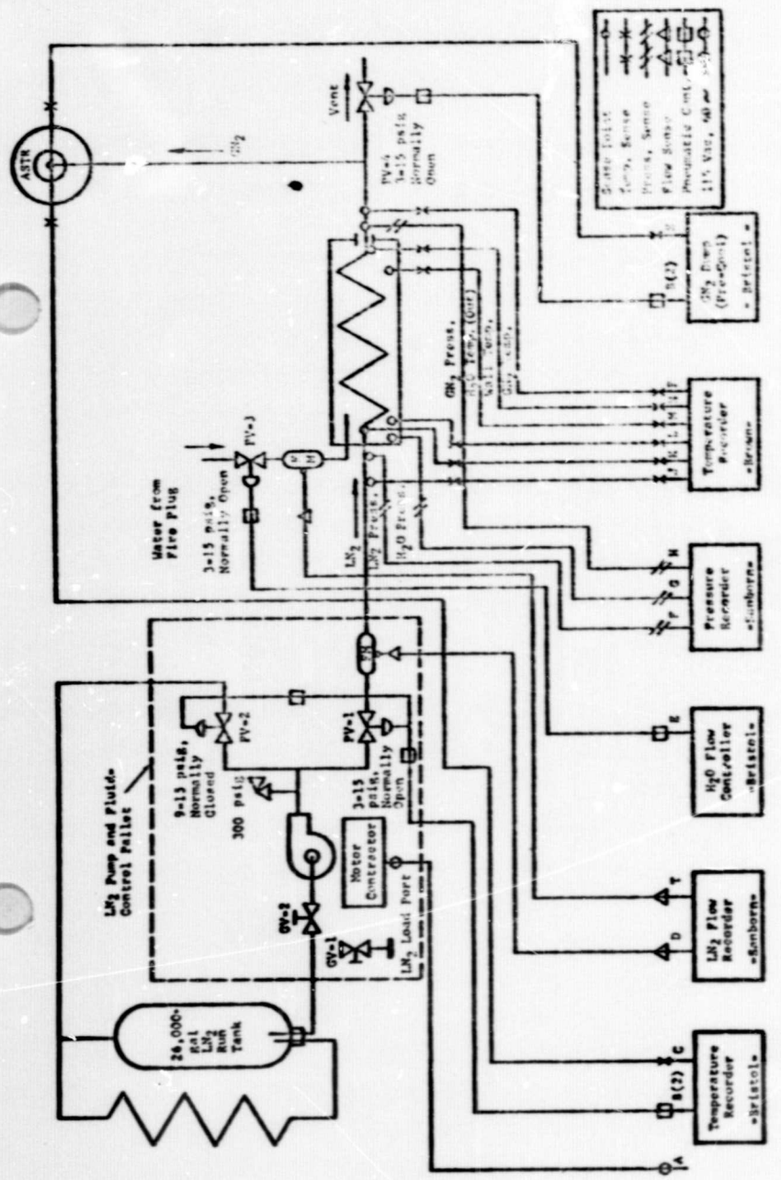

Figure 9 – Schematic of GN_2 Temperature Control System

manually operated test-channel selector and did not require the use of the Dymec. A stepping switch was used to select the function and channel, and the measurement was made with the appropriate instrument. Transducer outputs were measured with a Dana digital voltmeter, Model 5100-C1; Wiancko frequency with an Anadex counter-timer, Model CF-200R; and bridge resistance with a Rubicon Wheatstone bridge. Data obtained were manually recorded.

TABLE 3

SEQUENCE OF MEASUREMENTS WITH AUTOMATED DATA SYSTEM

Channel	Function	Item
000	Vdc	Excitation voltage
001	Frequency	Output, Wiancko pressure generator
002	mV	Output, transducer S/N 61
003	mV	Output, transducer S/N 47
004	mV	Output, transducer S/N 63
005	mV	Output, transducer S/N 50
006	mV	Output, dummy bridge No. 2
007	mV	Output, dummy bridge No. 3
008	-	Switching
009	-	Switching
010	kilohm	Bridge output resistance, S/N 61
011	kilohm	Bridge output resistance, S/N 47
012	kilohm	Bridge output resistance, S/N 63
013	kilohm	Bridge output resistance, S/N 50
014	kilohm	Bridge output resistance, dummy No. 2
015	kilohm	Bridge output resistance, dummy No. 3
016	-	Switching
017	kilohm	Bridge input resistance, S/N 61
018	kilohm	Bridge input resistance, S/N 47
019	kilohm	Bridge input resistance, S/N 63
020	kilohm	Bridge input resistance, S/N 50
021	kilohm	Bridge input resistance, dummy No. 2
022	kilohm	Bridge input resistance, dummy No. 3
023	-	Switching
024	-	Switching
025	-	Switching
026	mV	Temperature, hex-head instrumented transducer (Boss 1)
027	mV	Temperature, Boss 1
028	mV	Temperature, hex-head S/N 61 (Boss 2)
029	mV	Temperature, Boss 2
030	mV	Temperature, hex-head S/N 47 (Boss 3)
031	mV	Temperature, Boss 3
032	mV	Temperature, hex-head instrumented transducer (Boss 4)
033	mV	Temperature, Boss 4B
034	mV	Temperature, Boss 5A
035	mV	Temperature, hex-head S/N 50 (Boss 6)
036	mV	Temperature, internal junction A
037	mV	Temperature, internal junction B
038	mV	Temperature, instrumented transducer (Boss 1)
039	mV	Temperature, instrumented transducer (Boss 4)
040	mV	Temperature, instrumented transducer (Boss 4)

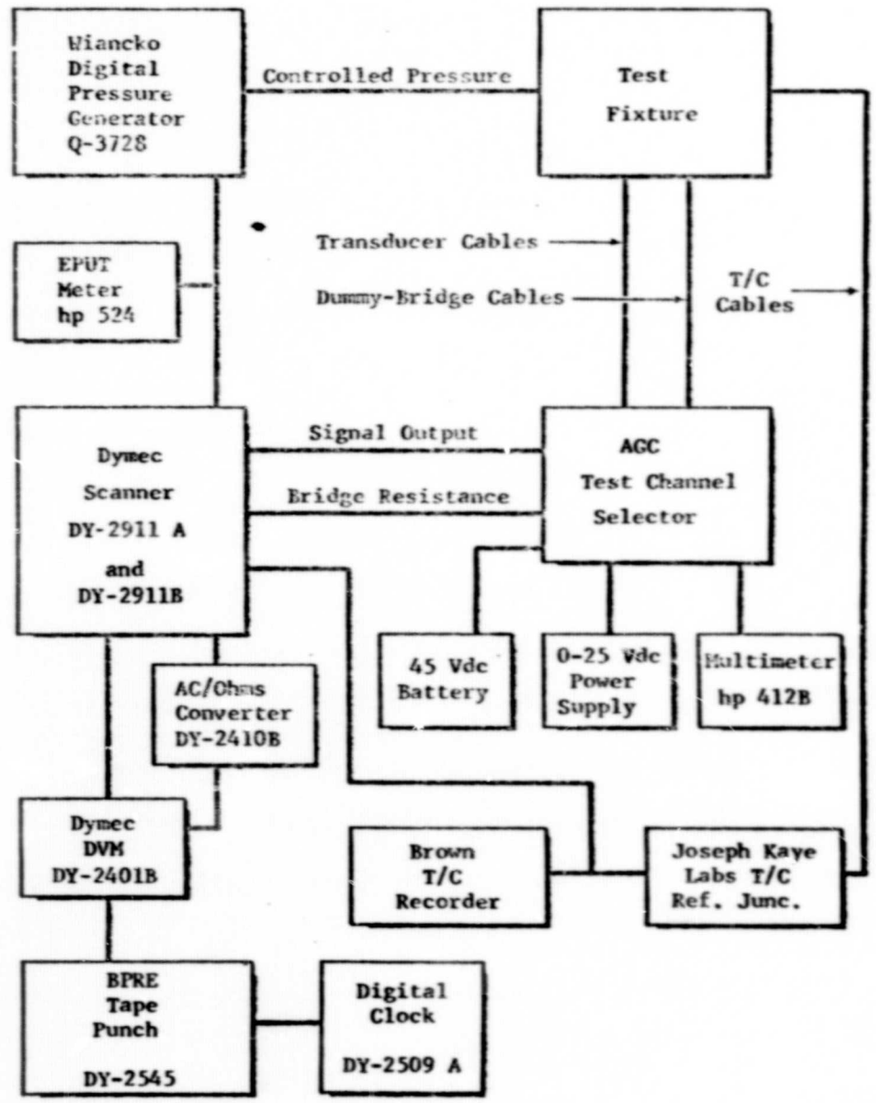

Figure 10 - Block Diagram of Automated Dymec Data System

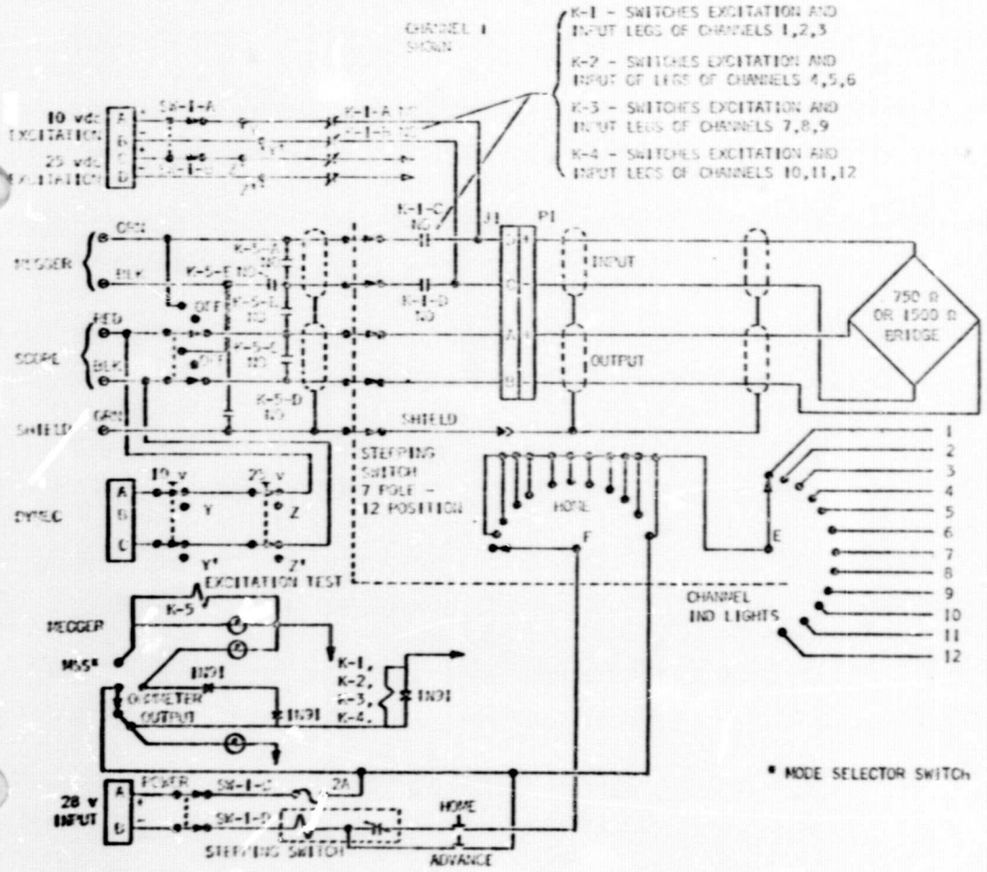

Figure 11 - Test Channel Selector Schematic

IV. TEST PROCEDURES

A. PRE-IRRADIATION

Following initial visual and electrical checks, the test fixture was set up in the CD/FW Irradiated Materials Laboratory (IML) with the Wiancko digital pressure generator and manual data system. The various data channels were checked (at all test pressures, where appropriate) to ensure proper operation of the system and to compare test results with those obtained by AGC in the NRO laboratory. No significant deviations in the data were observed and all channels were operational with the exception of one thermocouple (hex head of S/N 63 transducer), that had failed during tests at AGC.

Final assembly of the test fixture was completed after verification of satisfactory operation of all test channels and items. This consisted of welding the gas coolant lines to the spool, attaching fittings to the lines, and potting the electrical cables in the spool. The completed fixture was installed in the in-pile tube of the reactor and pressure checked to 50 psig. A small leak was observed around the electrical cable potting and was sealed with additional potting. A check of the coolant system revealed that the plenum fittings of the exhaust lines could not be tightened sufficiently to eliminate a small leak. A 1/4-in.-dia tube was added to the fixture through the spool to vent off the leakage.

On 10 August 1967, the complete test hardware was set up in the IML, using the automated test-channel selector with the Dymec system, including the 300-ft harness necessary to reach from the reactor area to the control room. A number of complete data cycles were obtained in the IML prior to transfer of the hardware to the reactor site.

Installation of the test hardware at the reactor and in the control room was made on 18 and 19 August. The test fixture was suspended in the

reactor pool and reconnected to the pressure and data systems. A complete system checkout early on 19 August was satisfactory; however, a check later in the day showed a decrease in the cable insulation resistance values. Measurements on the individual system components isolated the problem to the 300 ft extension harness, but no definite cause could be determined and it was decided to continue with the test.

Preirradiation data cycles were begun early in the morning on 21 August and continued for several hours prior to insertion of the test fixture in the reactor core. All measurements, including the insulation resistance were normal. After installation into the core, data cycles were again taken and a final checkout and connection of the coolant lines was completed with initiation of the cold gas coolant at a low flow rate. Measurements obtained just prior to reactor startup showed a decrease in all cable insulation resistances that was attributed to the effects of background radiation. The test was continued since all cables were in excess of 20 megohms.

B. IRRADIATION

Reactor startup was at 10:45 on 21 August. However, a scram occurred at a power level of approximately 30 KW. During preparations to resume operations, data cycles were periodically recorded (at zero psig). At 11:53 the reactor was again started and the first power level of 1.3 MW was reached at 12:12. Subsequent operation of the reactor was without incident. The sequence of operations and the various power levels are shown in Table 4, with reference to real and normalized time scales. The normalized time scale is shown for correlation since all subsequent data in the report are referenced to the normalized test time.

Two of the boss-temperature thermocouples (4A and 5B) were routed to Bristol temperature controllers and were used for the test fixture temperature control. The Bristol recorders were manually operated to maintain boss

TABLE 4

SEQUENCE OF EVENTS FOR TRANSDUCER IRRADIATION EXPERIMENT

Time (Normalized)	Time (CDT)	Event
0 - 3.2	04:16 - 07:30	Preirradiation data were taken with fixture in pool.
3.2 - 3.8	07:30 - 08:00	Fixture was installed in reactor.
3.8 - 6.5	08:00 - 10:45	Preirradiation data were taken with fixture in core.
5.6	09:54	GN_2 cooling system was started.
6.5	10:45	Reactor was started.
6.8	11:03	Reactor scrammed from 30 KW.
6.8 - 7.6	11:03 - 11:53	Preirradiation data were taken.
7.6 - 7.9	11:53 - 12:12	Reactor was started.
7.9 - 8.4	12:12 - 12:40	Power level was held at 1.3 MW.
8.4 - 8.5	12:40 - 12:44	Reactor power level was increased.
8.5 - 8.9	12:44 - 13:10	Power level was held at 1.98 MW.
8.9 - 9.0	13:10 - 13:14	Reactor power level was increased.
9.0 - 9.5	13:14 - 13:49	Power level was held at 3.62 MW.
9.5 - 9.6	13:49 - 13:51	Reactor power level was increased.
9.6 - 10.2	13:51 - 14:32	Power level was held at 5.83 MW.
10.2 - 10.3	14:32 - 14:35	Reactor power level was increased.
10.3 - 11.0	14:35 - 15:15	Power level was held at 7.3 MW.
11.0 - 11.1	15:15 - 15:17	Reactor power level was increased.
11.1 - 11.5	15:17 - 15:42	Power level was held at 9.4 MW.
11.5 - 11.6	15:42 - 15:46	Reactor power level was increased.
11.6 - 12.3	15:46 - 16:37	Power level was held at 9.9 MW.
12.3 - 12.4	16:37 - 16:42	Reactor power level was decreased.
12.4 - 14.2	16:42 - 18:30	Power level was held at 7.13 MW.
11.8	16:05	LN_2 pump was turned on.
12.8	17:00	Temperature was increased to 200°F.
13.2	17:33	Temperature was increased to 275°F.
14.2	18:30	Reactor was manually scrammed.
14.2 - 17.7	18:30 - 22:00	Postirradiation data were taken with fixture in core.
17.7 - 18.3	22:00 - 22:30	Fixture was removed from core.
18.3 - 18.5	22:30 - 22:50	Postirradiation data were taken with fixture in pool.

position 4E at the desired temperature. Generally, control was imprecise and severe temperature fluctuations occurred at each reactor power level.

Upon completion of the heating rate portion of the test, the reactor power level was reduced from 9.9 MW to 7.33 MW and the temperature at boss 4B was increased to 660°R. While attempting to increase the boss temperature to 760°R, an unstable temperature situation developed that was attributed to the time response limitation of the manually controlled system. After attempting to stabilize at 760°R, the control valves were set and the temperature was allowed to come to equilibrium at approximately 735°R. Data cycles were obtained at this temperature and having reached the nominal 40-MW-hr limit of reactor operation, the irradiation test was terminated.

C. POSTIRRADIATION

Data cycles were obtained at approximately hourly intervals until the test fixture was removed from the reactor core about 4 hr after shutdown. The coolant lines were disconnected and the in-pile tube was removed from the reactor core, lowered back into the water, and secured at the edge of the reactor pool. It was not necessary to disconnect the electrical cables or the gas pressurization line. After completion of the transfer operation, one additional data cycle was taken.

The following morning, 22 August, several data cycles were run with the automated data acquisition system. Then, because of a requirement for the Dymec on another experiment, data acquisition was switched back to the manual data system. One data cycle was taken each day with the manual system on 22, 23, and 24 August and two data cycles were taken on 25 August.

D. RADIATION LEVELS

In preparation for the 23/8512A rate-effects test, the radiation field within the in-pile tube of the ASTR was extensively mapped in experiments conducted in May and June 1967. An aluminum pedestal-type calorimeter, designed and fabricated by GD/FW, was used to measure the nuclear heating rates at several locations along the axis of the in-pile tube at reactor power levels from 0.273 to 6.78 MW. Gamma dose-rate measurements were obtained along the axis of the tube by a continuous traverse through the core of a 4-cc carbon ion chamber at power levels from zero to 165 KW. Gamma dose measurements were made with cobalt-glass and AGC supplied thermoluminescent dosimeters at low power levels (1.65 KW maximum). Simultaneously the neutron-flux distribution was mapped using standard irradiated foil techniques. The gamma-dose and neutron-flux data were obtained with an inactive perturbation test fixture installed in the in-pile tube. The calorimeter, ion chamber, cobalt-glass, and neutron foil mapping data are reported by GD/FW in Reference 5 and the thermoluminscent-dosimeter mapping data are reported by AGC in Reference 6.

1. Nuclear Heating Rate

Nuclear heating rates in the aluminum calorimeters were calculated for various locations along the in-pile tube and converted to give corresponding heating rates in carbon. The profile of the nuclear heating rates in carbon is shown in Figure 12 with the relative positions of the test transducers.

2. Gamma Dose Rates

The gamma dose-rate profile through the ASTR core as measured with the carbon ion chamber is shown by the solid curve of Figure 13. For comparison, the calorimeter data, converted to dose rate are also shown.

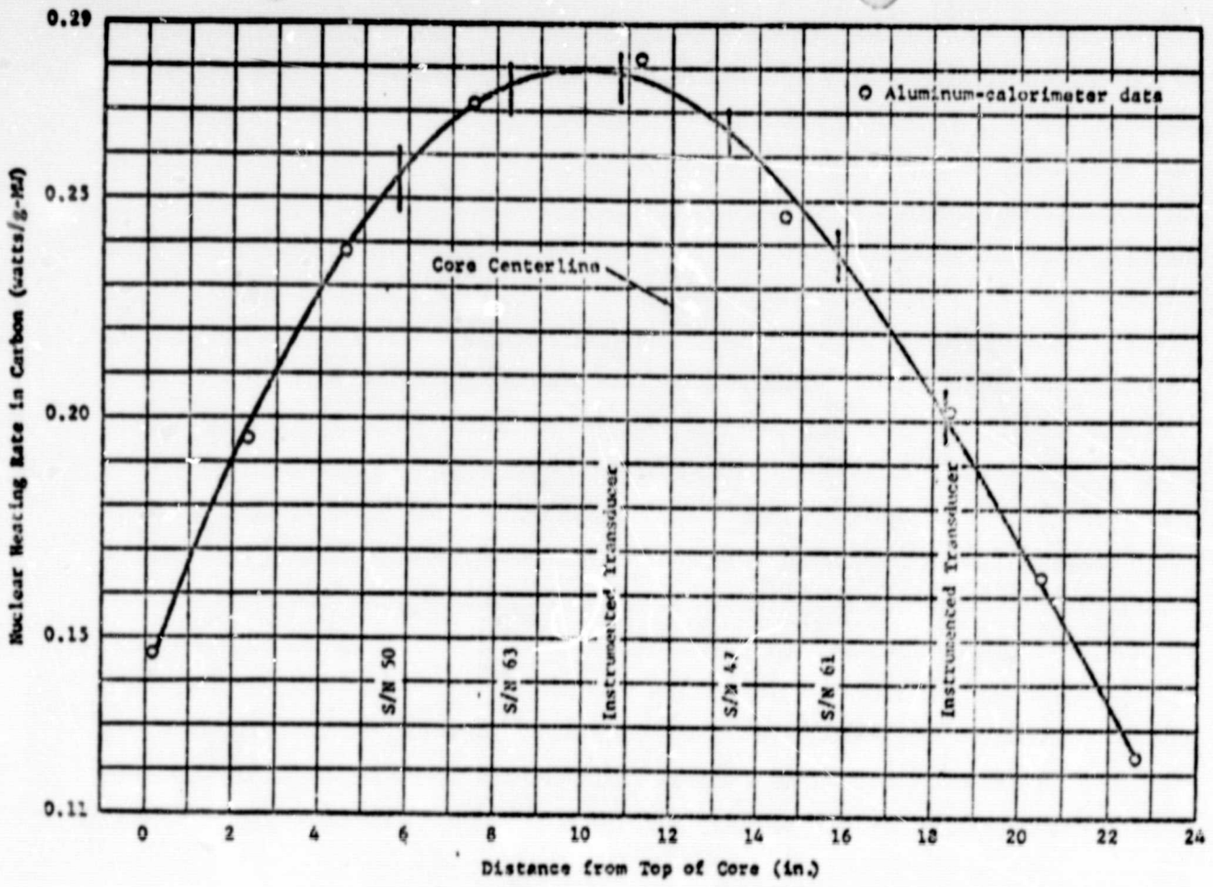

Figure 12 - ASTR Heating Rate Profile

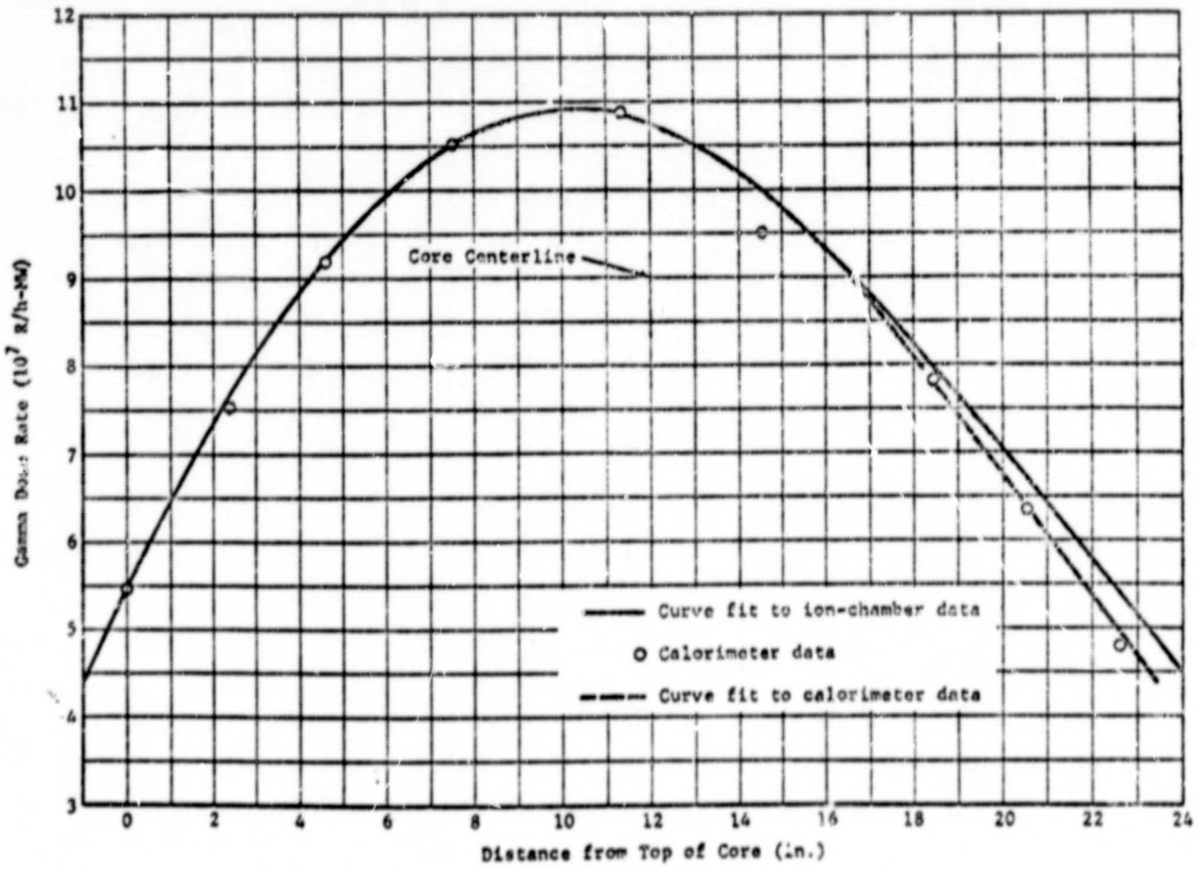

Figure 13 - ASTR Gamma-Dose-Rate Profile

Core background measurements obtained during the mapping runs indicated that the peak dose rate was 2×10^3 R/hr. The profile of the background dose rate through the case is essentially the same as the profile shown in Figure 13.

The core background following a reactor shutdown decreases quite rapidly with time and data obtained were insufficient to permit an accurate estimate of the dose rates during the decay time.

3. Neutron Flux

In the mapping experiment, neutron fluxes of energy greater than 2.9 Mev were measured with sulfur pellets in four separate low-power-level irradiations. A total of 36 pellets were exposed at seven axial distances into the reactor core. These data converted to fluxes above 1.0 Mev are presented in Table 5 with the standard deviations of the average values. Also shown in Table 5, for comparison, are the average fluxes obtained at three locations with the transducer-fixture simulation device (perturbation fixture).

TABLE 5

AVERAGE NEUTRON FLUXES FROM MAPPING EXPERIMENT

Axial Distance* (in.)	Average Flux (10^5 n/cm^2-sec-W)	Relative Std. Dev. (%)	Measurements in Average
2	23.00	4.8	5
4.5	32.8	---	1
7	37.7**	7.6	3
	37.1	5.3	8
12	39.2**	7.1	3
	38.8	5.3	8
17	30.9**	8.2	3
	30.5	5.8	8
19.5	25.4	---	1
22	16.5	2.9	5

* From top of core.
** Measurement with perturbation fixture

Neutron foil detectors were attached to the test fixture to measure the transducer neutron fluence as shown in Figure 14. Sulfur pellets in aluminum covers were used at seven fixture locations and phosphorus pellets in aluminum covers were placed at alternate positions starting at the fixture end, with cadmium-shielded phosphorus pellets located at the three remaining positions.

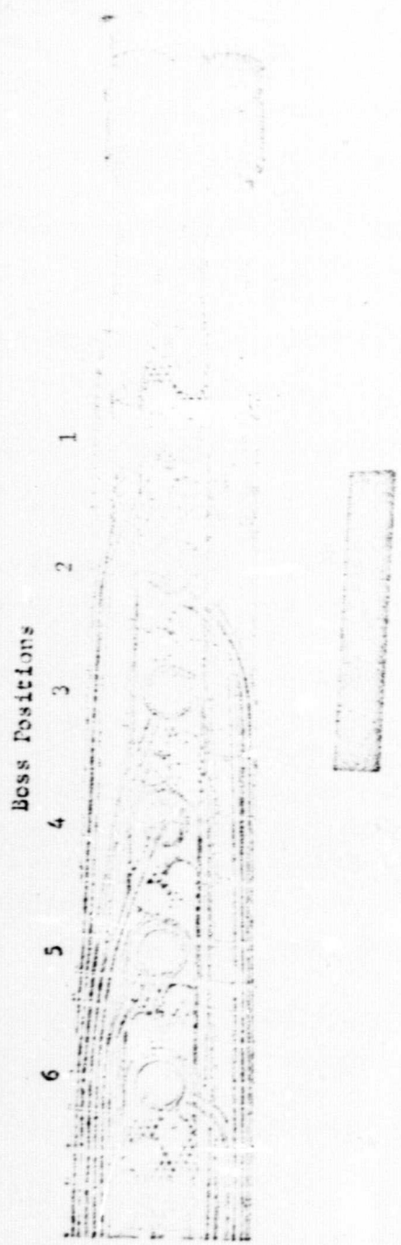

Figure 14 - Test Fixture with Foil Packets Attached

V. TEST RESULTS

With the expected test results, the data also contained unexpected results. These unexpected results require more extensive analysis to determine if they are valid data or malfunctions in the test monitoring instrumentation. The space limitations of the reactor test volume restrict the number of test measurements so that only a probable cause of the unexpected results can be set forth.

The analysis and discussion of the test results in this section are arranged in an increasing order of dependency of the subsequent data on the preceding data. As a result, the performance of the pressure transducers, the main objective of the test, are discussed last since their performance is dependent on all other factors combined.

The data from the test were reduced and reported by GD/FW in Reference 7. The data are not presented in their entirety and are summarized in the form of tables and figures that average the values for each experimental condition. Also included in the report are brief summary descriptions of the data with possible causes of obvious anomalies. Subsequent to the irradiation test, a re-evaluation of the nuclear heating rates was conducted and the results are reported in Reference 8.

Because of the bulk of data obtained during the test, all of the automated data, which were stored on punched paper tape, were programmed into an IBM 1130 computer for ease of manipulation and reduction. For programming purposes, the test time, recorded digitally in real time in 10-hour intervals, was normalized to reflect elapsed time such that 0.0 hours time in the computer data was equivalent to 04:14:00 hours real time. This adjustment must be made when comparing these data with real time data.

A. DOSIMETRY

1. Neutron Flux

During retrieval of the sulfur and phosphorus pellets from the irradiated fixture, the cadmium shield on the phosphorus pellets was found to be partially melted. These data were disregarded in the subsequent neutron flux determination, because it was believed that the activity levels of the shielded phosphorus pellets would be too high for useful correlation.

The neutron flux of energy greater than 1 Mev is shown in Figure 15, and is plotted as a function of axial position with the data obtained during the mapping experiment. The data obtained from the sulfur pellets (E > 2.9 Mev) were multiplied by 2.8 to convert to fluxes above 1.0 Mev. The averages and standard deviations of all mapping data are also shown.

The test data generally fall within the standard deviation of the mapping data, but appear to be displaced slightly toward the bottom of the core. This displacement may be the result of a true downward shift of the flux profile during long high-power-level irradiations. This would be a consequence of control rod withdrawal, which is from the bottom of the core.

Interpolating the average neutron fluxes for each of the active transducer locations indicates that the following neutron fluences (E > 1.0 Mev) were attained:

S/N 47	5.8×10^{17} n/cm^2
S/N 50	4.9×10^{17} n/cm^2
S/N 61	5.1×10^{17} n/cm^2
S/N 63	5.6×10^{17} n/cm^2

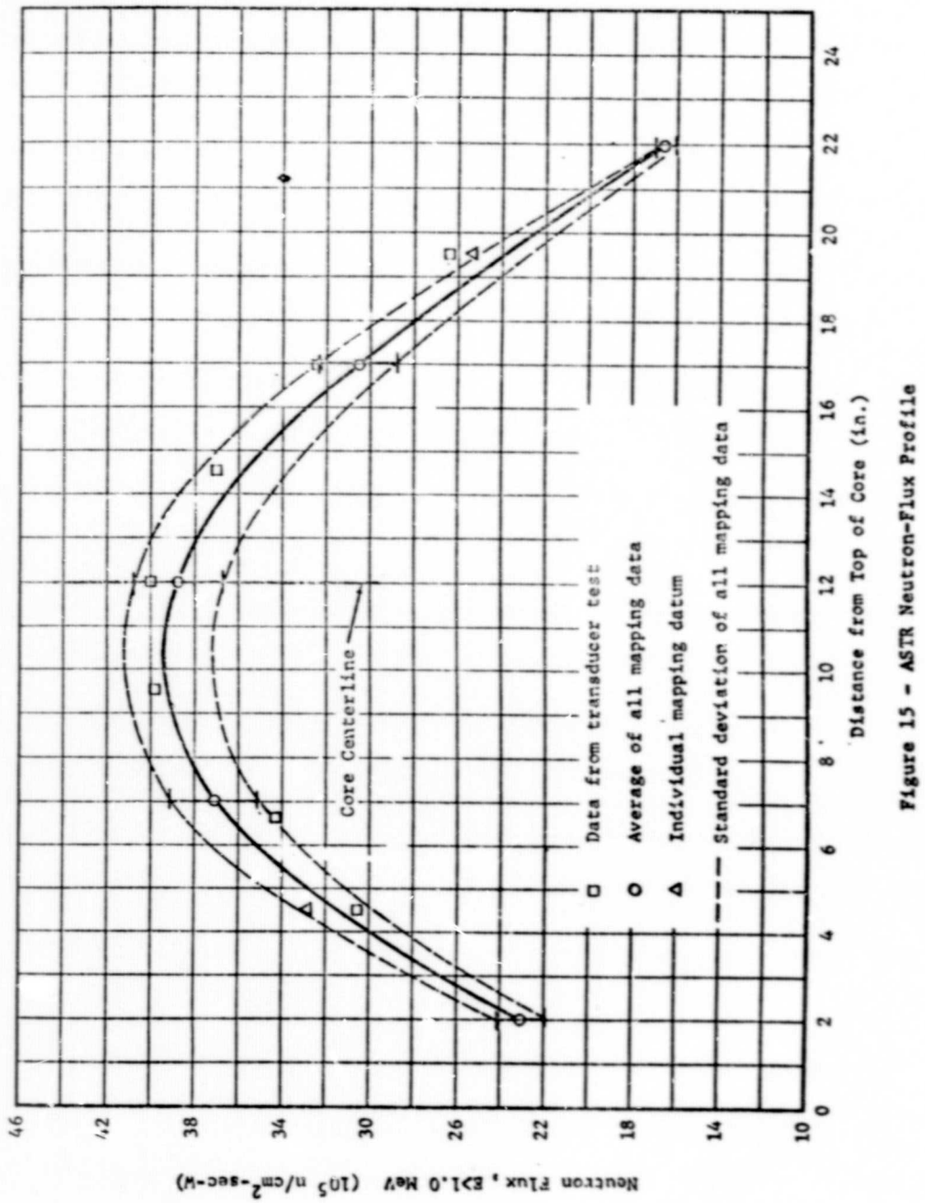

Figure 15 - ASTR Neutron-Flux Profile

2. Nuclear Heating Rates

The nuclear heating rates, based on the pretest mapping run data, for each of the transducer locations are shown in Table 6 for each of the reactor power-level holds. However, an uncertainty analysis of the heating rates conducted by AGC indicated that errors attributed to fission product buildup and the observed downward shift of the flux profile caused by control rod withdrawal were not considered and that the assigned flux uncertainty of ± 9.6% was too low. The uncertainty analysis indicates that an uncertainty of ± 14.1% with a 95% confidence level would be more realistic.

Subsequent to the AGC uncertainty analysis, GD/FW reexamined their method of specifying heating rates. Corrected flux data for the ASTR test that took into consideration fission product buildup and flux profile shift was reported in an addendum (Reference 8). The corrected heating-rate data are shown in Table 7 with estimated uncertainties.

B. TEMPERATURES

Temperature data were obtained during the test from 16 thermocouples located on the test fixture and transducers. Seven copper-constantan thermocouples monitored the transducer-boss temperatures, 6 copper-constantan thermocouples monitored the transducer hex-head temperatures, and 3 chromel-alumel thermocouples were used to monitor internal transducer-diaphragm temperatures in boss positions 1 and 4. In addition, 2 copper-constantan thermocouples monitored the internal-conductor temperatures in the two specially constructed thermocouple cables attached to the bottom of the test fixture.

Thermocouple data, recorded in millivolts, were reduced to temperatures by means of a polynomial conversion computer program shown in Table 8. The polynomial reduction in within 0.1°K of the KBS standard thermocouple tables.

TABLE 6.

HEATING RATE AT THE TRANSDUCER BOSS POSITIONS

Time Interval	Power Level (MW)	Heating Rate [Watts/gm (C)] Boss 1 Instrumented	Boss 2 S/N 61	Boss 3 S/N 47	Boss 4 Instrumented	Boss 5 S/N 63	Boss 6 S/N 50
Mapping Data*	1.0	0.200	0.238	0.265	0.279	0.276	0.255
1212-1240	1.30	0.26	0.31	0.34	0.36	0.36	0.33
1244-1310	1.98	0.40	0.47	0.52	0.55	0.55	0.50
1314-1349	3.62	0.72	0.86	0.96	1.01	1.00	0.92
1351-1432	5.8'	1.17	1.39	1.54	1.63	1.61	1.49
1433-1515	7.3	1.46	1.74	1.93	2.04	2.01	1.86
1517-1542	9.4	1.88	2.24	2.49	2.62	2.59	2.40
1546-1637	9.9	1.98	2.36	2.62	2.76	2.73	2.52
1642-1830	7.13	1.43	1.70	1.89	1.99	1.97	1.82
1830	0						

*Reference (FZK-343)

TABLE 7

HEATING RATE AT THE BEGINNING AND END OF DATA CYCLES
AFTER CORRECTION FOR PROFILE SHIFT AND GAMMA BUILDUP

Time Interval	Power Level (MW)	Heating Rate W/g(C) Boss 1	Boss 2	Boss 3	Boss 4	Boss 5	Boss 6	Uncertainty (2σ) (±%)
1213-1232	1.30	0.25-0.26	0.30-0.31	0.33-0.34	0.34-0.36	0.34-0.36	0.32-0.33	12.6
1246-1305	1.98	0.38-0.39	0.45-0.46	0.49-0.51	0.52-0.54	0.52-0.54	0.48-0.49	12.6
1323-1347	3.62	0.70-0.72	0.83-0.85	0.93-0.95	0.98-1.00	0.97-0.99	0.89-0.91	12.6
1402-1421	5.83	1.14-1.16	1.33-1.38	1.50-1.53	1.59-1.62	1.57-1.60	1.45-1.48	15
1442-1501	7.3	1.51-1.53	1.73-1.76	1.89-1.92	2.09-2.12	2.04-2.07	1.77-1.80	15
1526-1541	9.4	2.05-2.08	2.35-2.38	2.49-2.52	2.60-2.63	2.54-2.57	2.19-2.21	15
1553-1610	9.9	2.18-2.20	2.48-2.50	2.65-2.68	2.76-2.79	2.70-2.73	2.32-2.34	15
1643-1653	7.13	1.66-1.62	1.88-1.83	2.01-2.00	2.10-2.05	2.05-2.01	1.76-1.72	15
1705-1726	7.13	1.60-1.59	1.81-1.80	1.95-1.93	2.03-2.01	1.99-1.97	1.70-1.69	15
1804-1824	7.13	1.69-1.68	1.83-1.82	1.89-1.88	1.98-1.97	1.85-1.84	1.62-1.61	15

Boss 1 - Instrumented Transducer
Boss 2 - Transducer S/N 61
Boss 3 - Transducer S/N 47

Boss 4 - Instrumented Transducer
Boss 5 - Transducer S/N 63
Boss 6 - Transducer S/N 50

TABLE 8

POLYNOMIAL CONVERSION OF MILLIVOLTS TO TEMPERATURE

Thermocouple: Copper-Constantan

Range: 260 to 1200°R

Output (MV)	Polynomial	Variable Z
$-4.1222 < E < 9.5353$	$254.959 + 1001.86Z - 1193.32Z^2 + 2107.58Z^3 - 2530.13Z^4 + 1674.26Z^5 - 455.266Z^6$	$0.305306 + 0.072855E$
$9.5353 < E < 20.4741$	$855.003 + 374.320Z - 39.3126Z^2 + 12.2272Z^3 - 2.24450Z^4$	$-0.846676 + 0.0901957E$

Thermocouple: Chromel-Alumel

Range: 280 to 790°R

Output (MV)	Polynomial	Variable Z
$-4.0829 < E < 0.8396$	$274.715 + 318.897Z - 113.862Z^2 + 67.6887Z^3 - 17.7946Z^4$	$0.832107 + 0.199968E$
$0.8396 < E < 6.7567$	$529.628 + 265.642Z - 43.7906Z^2 + 187.050Z^3 - 542.002Z^4 + 815.612Z^5 - 574.055Z^6 + 151.569Z^7$	$-0.141894 + 0.169002E$

In general, all temperature data exhibited severe fluctuations throughout the test. These fluctuations were attributable to the imprecise control of the GN_2 fixture coolant. To facilitate the analysis, the temperature data were thinned to include only data recorded during the zero-pressure data cycles. The resultant thinned data more clearly illustrate the temperature treads throughout the test and permits better correlation of the data at selected times.

Even with the thinned data, however, the temperature fluctuations were still severe. Data obtained during any one cycle were representative of the fixture temperatures at that time, but would disagree with the preceding and succeeding cycles by many degrees depending on whether the temperatures were increasing or decreasing. Correlation temperatures reported in this section were obtained by averaging data from 10 to 20 successive cycles during selected heating rate or temperature hold periods. Although the averaged temperatures may not be indicative of the absolute fixture temperatures, they are relative to one another and represent comparative averages during the specified hold periods.

1. Boss Temperatures

Transducer boss temperature data obtained during the test are shown in Figures 16 through 20. Temperature data for boss thermocouples 4A and 5B were recorded on a Bristol Recorder (Figures 21 and 22) and were monitored visually throughout the test. These data were used to control the flow of coolant to the fixture to maintain the required fixture test temperatures throughout the test. No data are shown for position 6 boss because physical limitations precluded the installation of a thermocouple in that location.

In general, the temperature data are in good agreement with each other and clearly show the control of the test temperatures during Part I, i.e., constant temperature of 560°R and variable heating rates, and

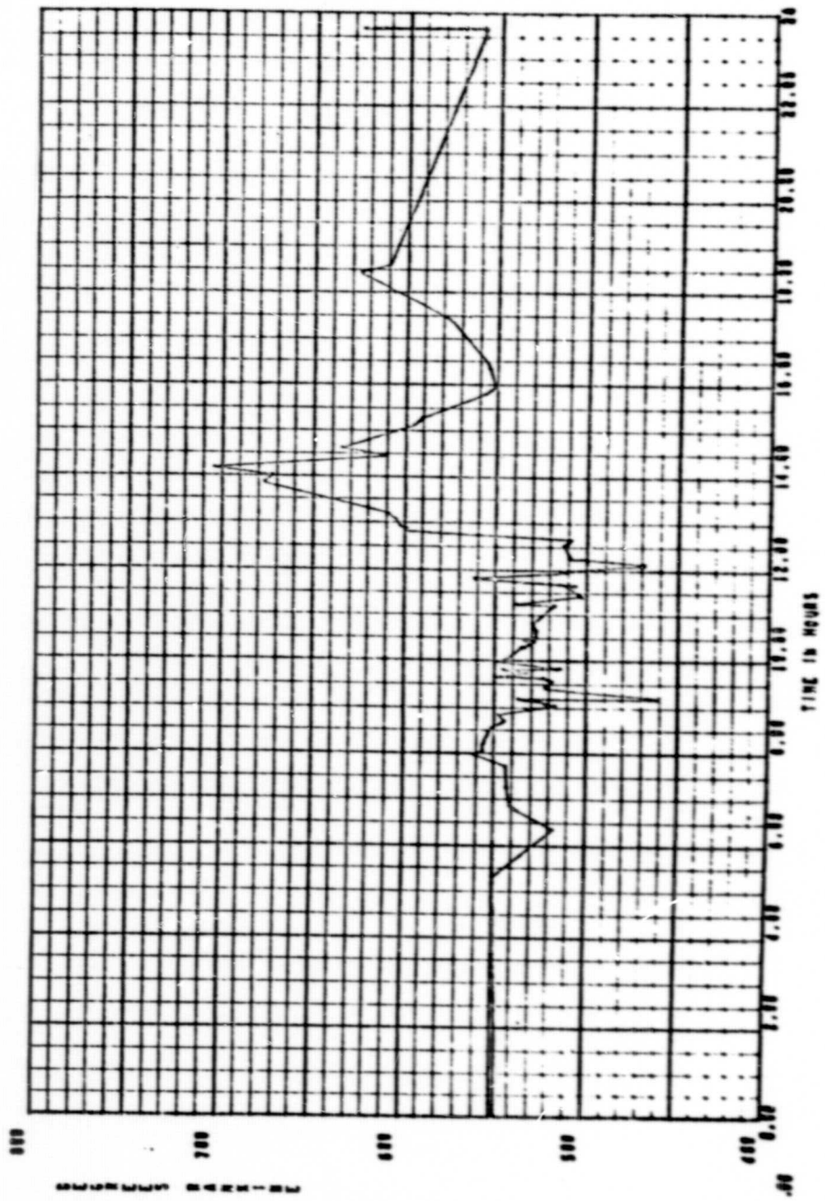

Figure 16 - Boss 1 Temperature

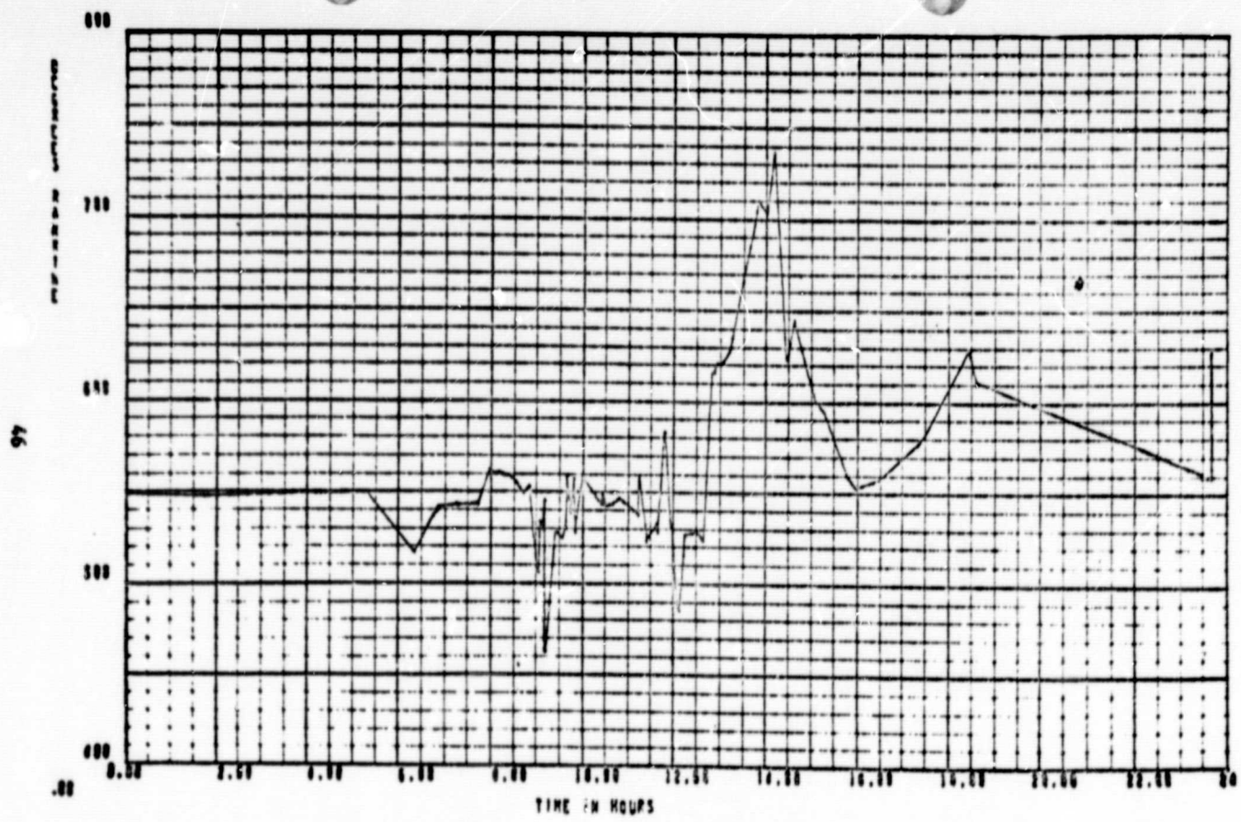

Figure 17 - Boss 2 Temperature

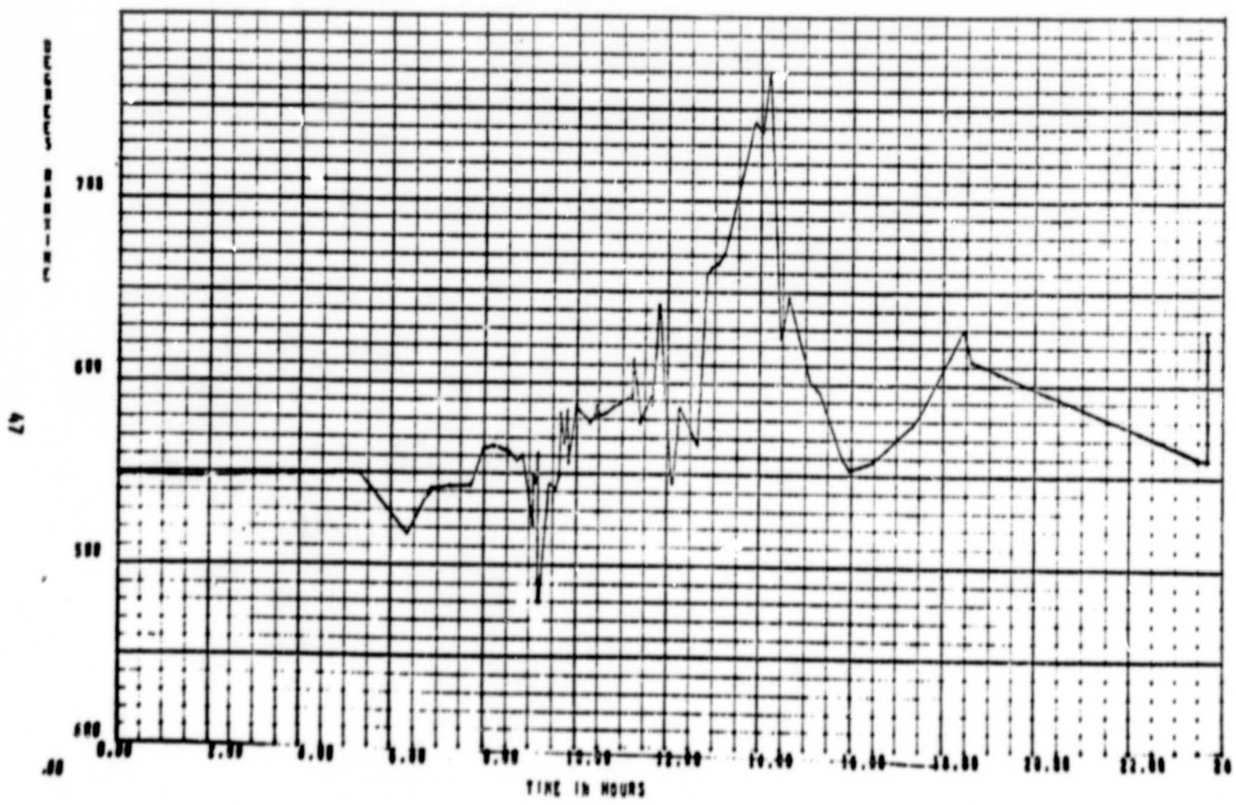

Figure 18 - Boss 3 Temperature

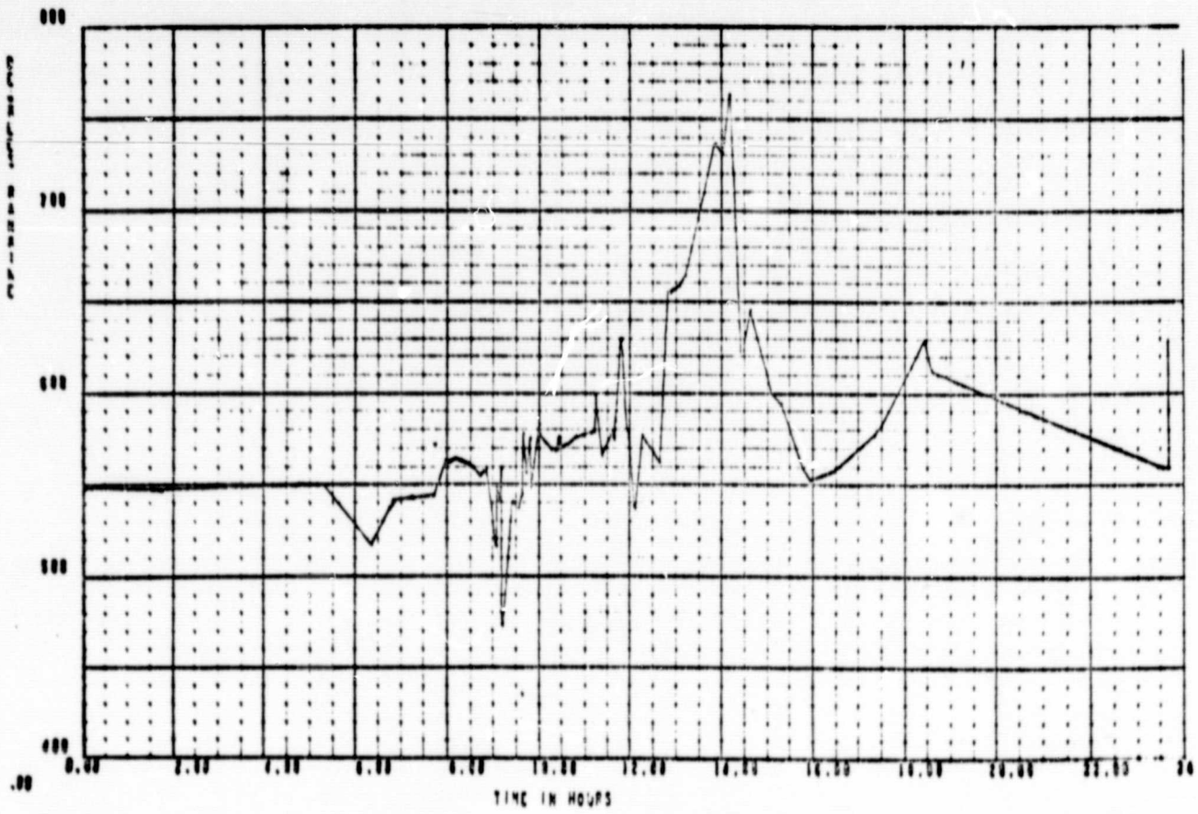

Figure 19 - Boss 4B Temperature

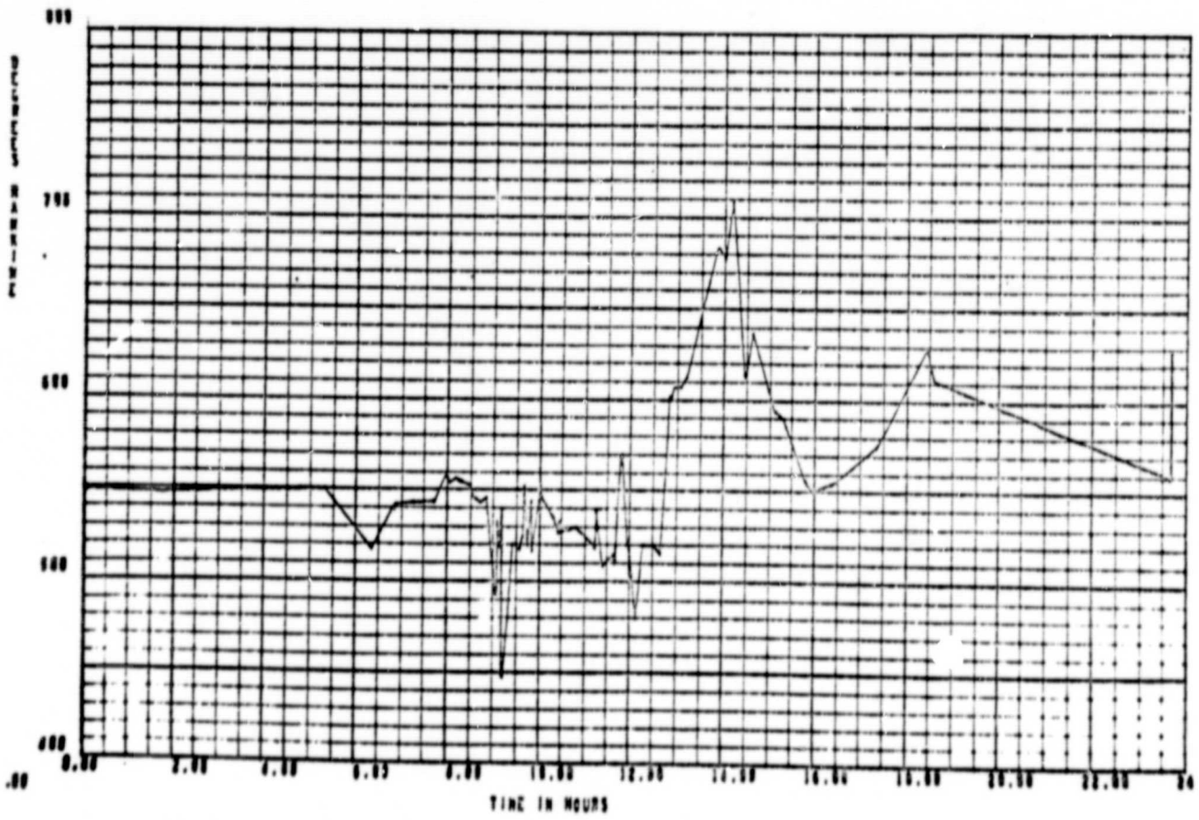

Figure 20 - Boss 5A Temperature

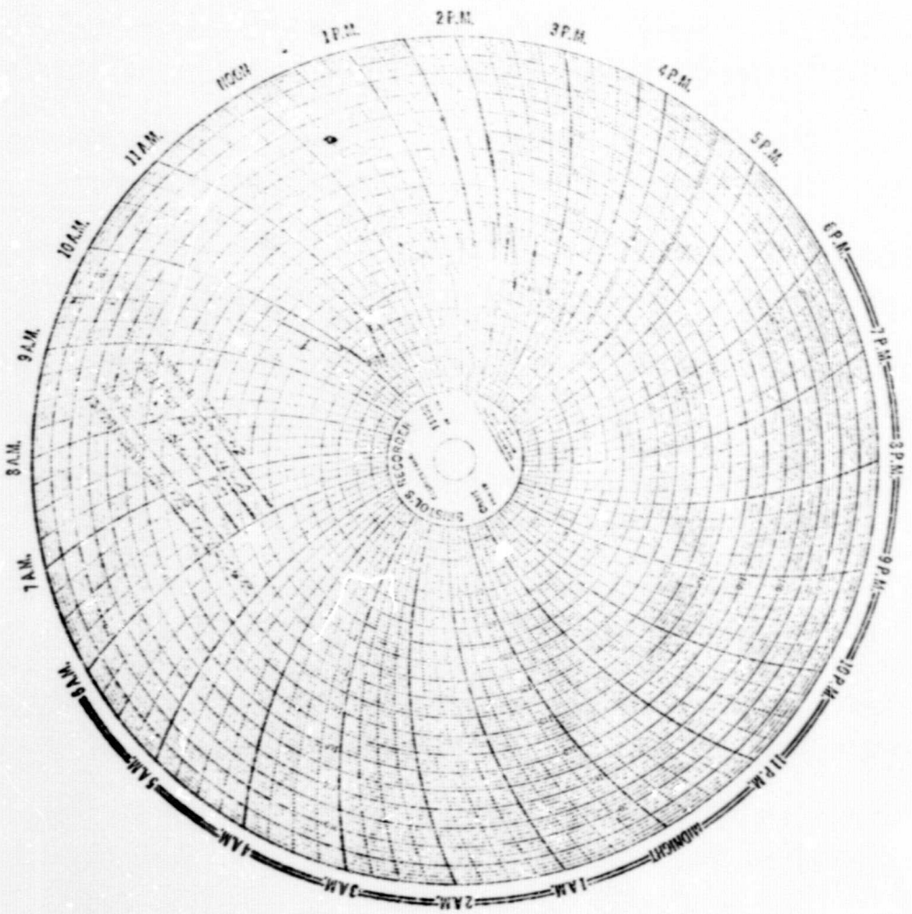

Figure 21 - Boss 4A Temperature, Bristol Recorder

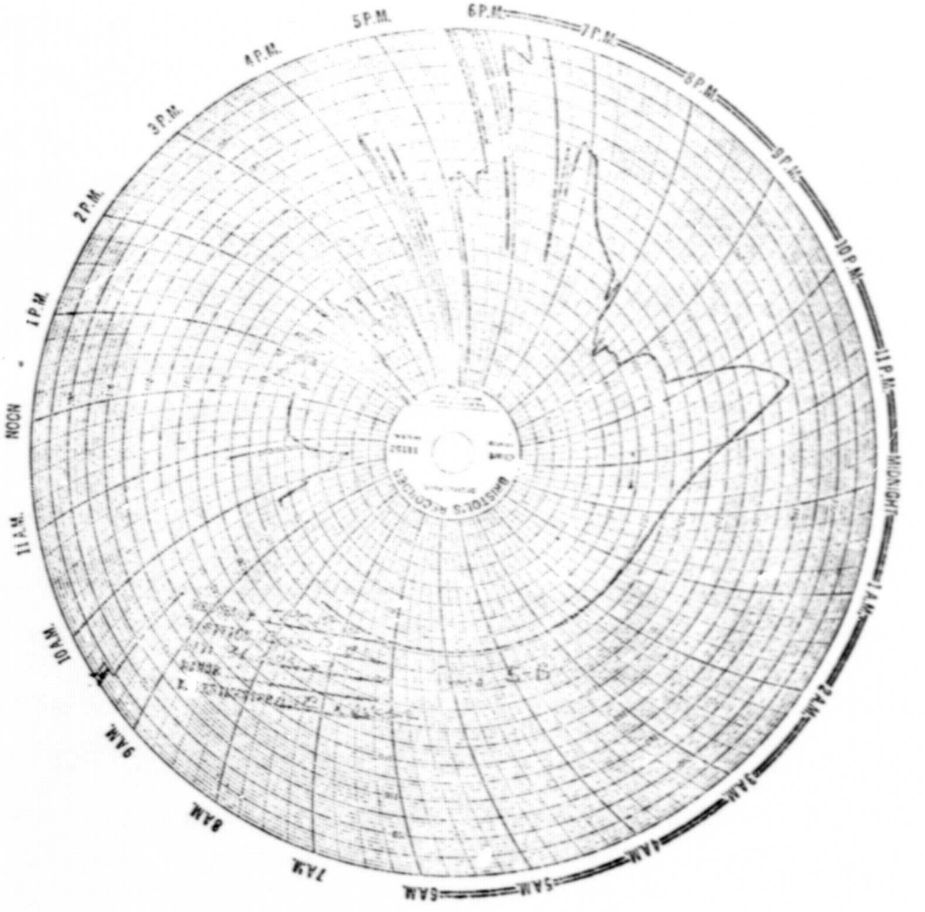

Figure 22 - Boss 5B Temperature, Bristol Recorder

Part II, i.e., constant heating rate of 2 watts/gm(C) and variable temperatures. The difference in temperature along the fixture is due to the fact that the fixture temperature could only be controlled at one location (Boss 4A) and all other positions attained their own equilibrium values which corresponded to the nuclear heating rates and fixture coolant flow conditions.

The boss temperatures at selected times during Part II of the test are shown plotted as a function of the distance from the top of the core in Figure 23. An apparent anomaly exists at the Boss 3 position since the data differ from predictions based on the heating rate profile (Figure 12). The most probable cause of the anomaly is that the thermocouple junction was not in good contact with the fixture. The fixture, machined out of aluminum, is an excellent thermal conductor, and a localized higher temperature in the center of the fixture does not appear probable based upon the heating rate profile. However, this conclusion implies that the validity of the remaining thermocouple temperature data is difficult to assess without a reference standard.

Since the forcibly cooled aluminum fixture is the heat sink for the thermocouples, gamma generated heat in the cables will flow towards the sensing junction as well as toward the coolant exhaust tubes. A poor contact between the junction and the fixture will result in a positive unidirectional error, i.e., the thermocouple will indicate a higher temperature than the actual fixture temperature. The possibility exists that all boss thermocouples are not in good contact with the fixture.

Even though the aluminum is an excellent thermal conductor, at the heating rates experienced during the test, gradients, proportional to the gamma-flux profiles would be expected along the length of the fixture. Comparison of the temperature data in Figure 23 shows correlation of all temperatures except for Boss 3. This indicates that Boss 1, 2, 4, and 5 thermocouples have essentially the same degree of contact. The dashed lines

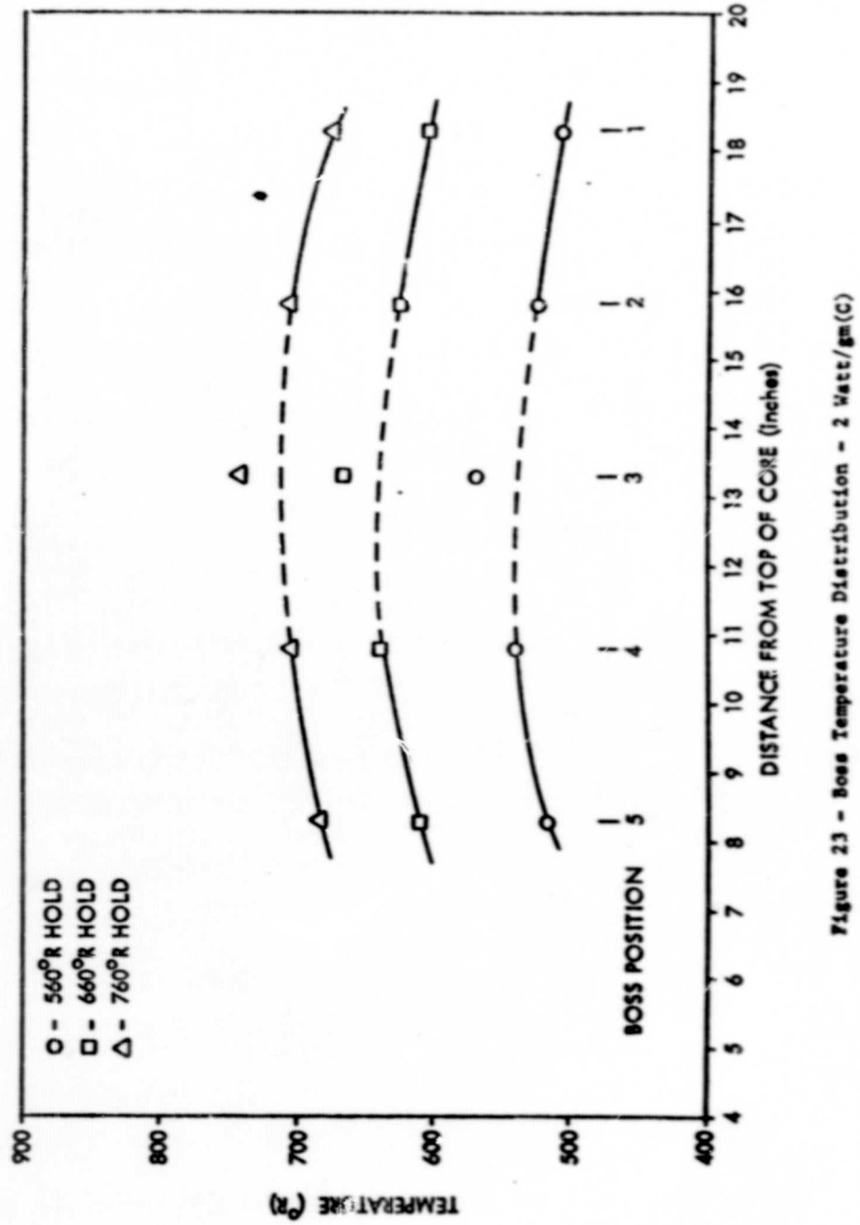

Figure 23 - Boss Temperature Distribution - 2 Watt/gm(C)

in Figure 23 indicate the extrapolated temperature distribution between Boss 2 and 4 locations assuming that the Boss 1, 2, 4 and 5 temperature data are valid.

2. Hexagonal Head Temperatures

A copper-constantan thermocouple was welded to the hexagonal head of each test transducer. Temperature data obtained during the test for each of these thermocouples are shown in Figures 24 through 28. No data are shown for Boss 5 hex-head thermocouple which had failed during the pretest checkout.

Located further from the fixture coolant source, the hex-head thermocouples clearly show the rise in temperatures during the step increases in gamma rates during Part I of the test. The data are in good agreement with each other and, like the boss thermocouple data, reflect the gamma-heating-rate profile through the reactor core. However, comparing the readings of the respective thermocouples at selected times throughout the test reveals an apparent anomaly in hex-head 3 temperature data.

To illustrate this anomaly, hex-head temperature data obtained during Part I of the test are shown plotted in Figure 29. Examination of the data shows a temperature inflection at the Boss 3 position that is not consistent with the boss temperature profile (Figure 23) or the nuclear heating-rate profile shown in phantom lines. Various possible causes of the anomaly were investigated and the most probable cause was determined as the thermocouple junction having poor thermal contact with the hex-head surface. The observed temperature reflects the equilibrium temperature between the sensing junction and the exhaust coolant tube for the various heating rates.

Similar to the boss temperature, this conclusion also implies that an uncertainty exists in the remaining hex-head temperature data. However, in this case, a poor contact between the junction and the hex-head results in

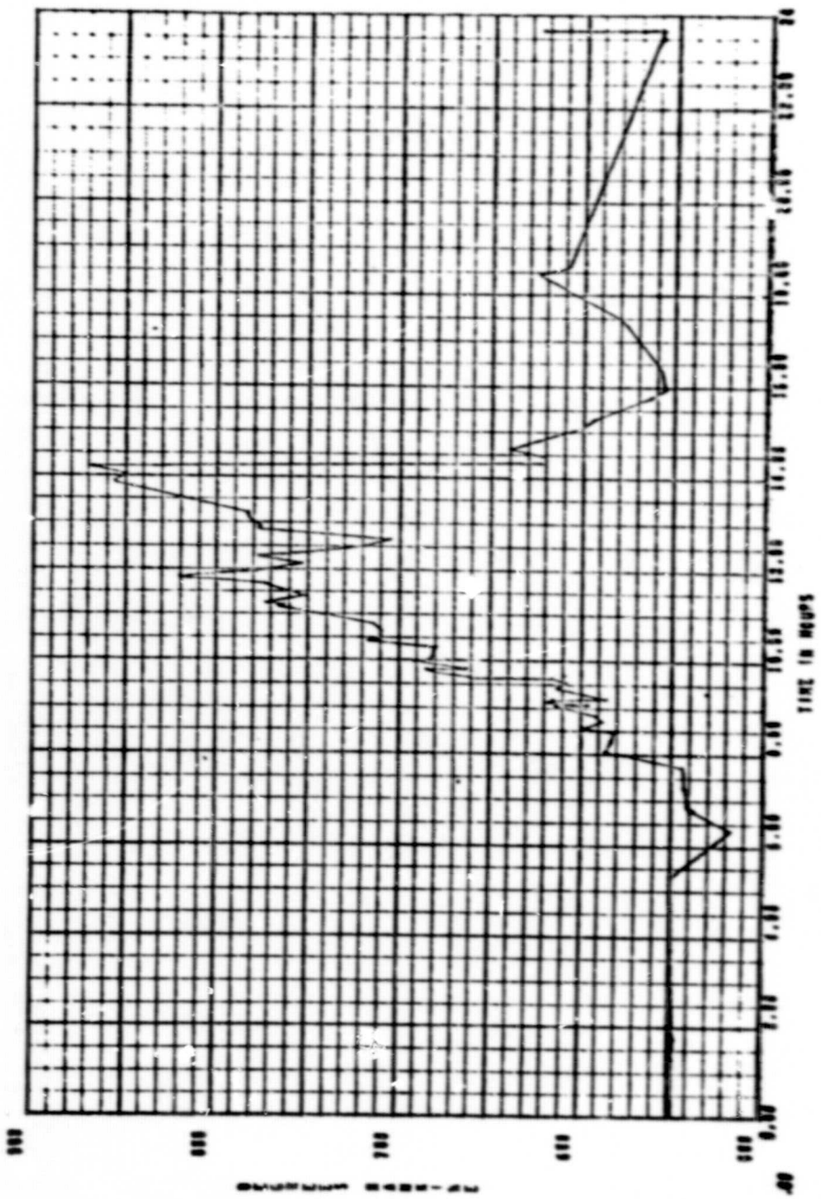

Figure 24 - Hex-Head 1 Temperature, Instrumented Transducer

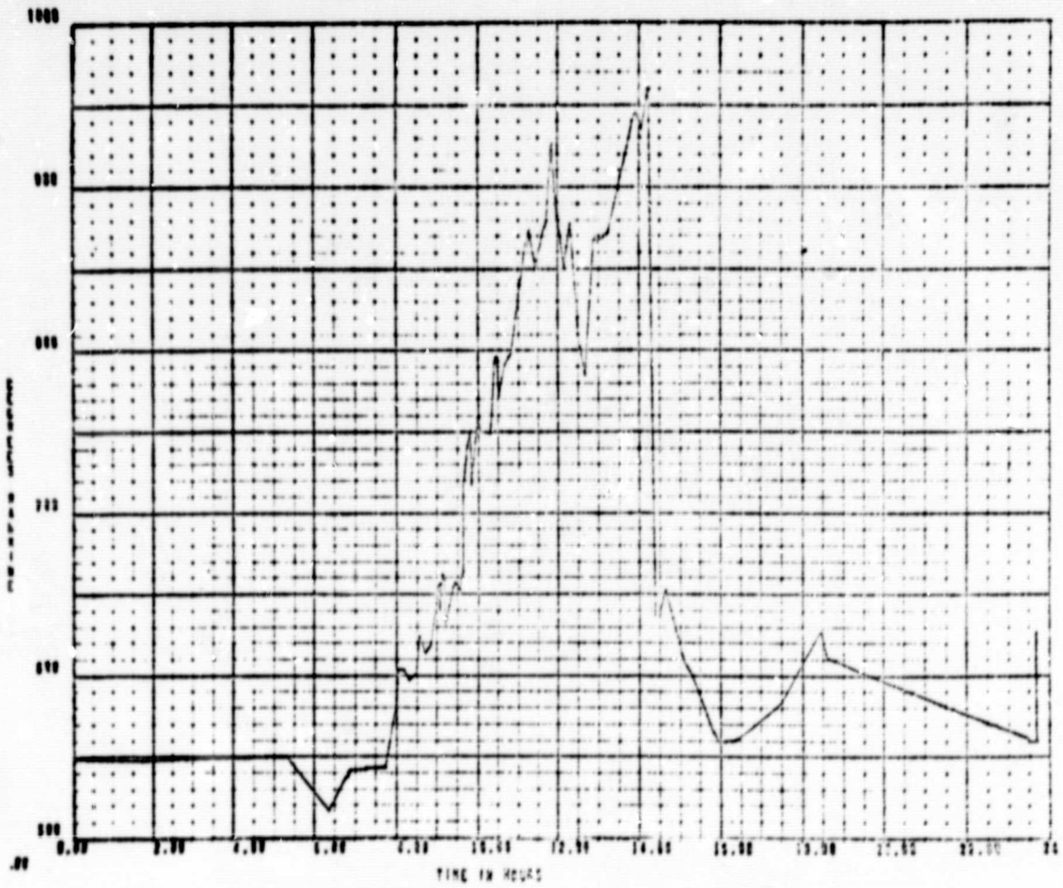

Figure 25 - Hex-Head 2 Temperature, S/N 61 Transducer

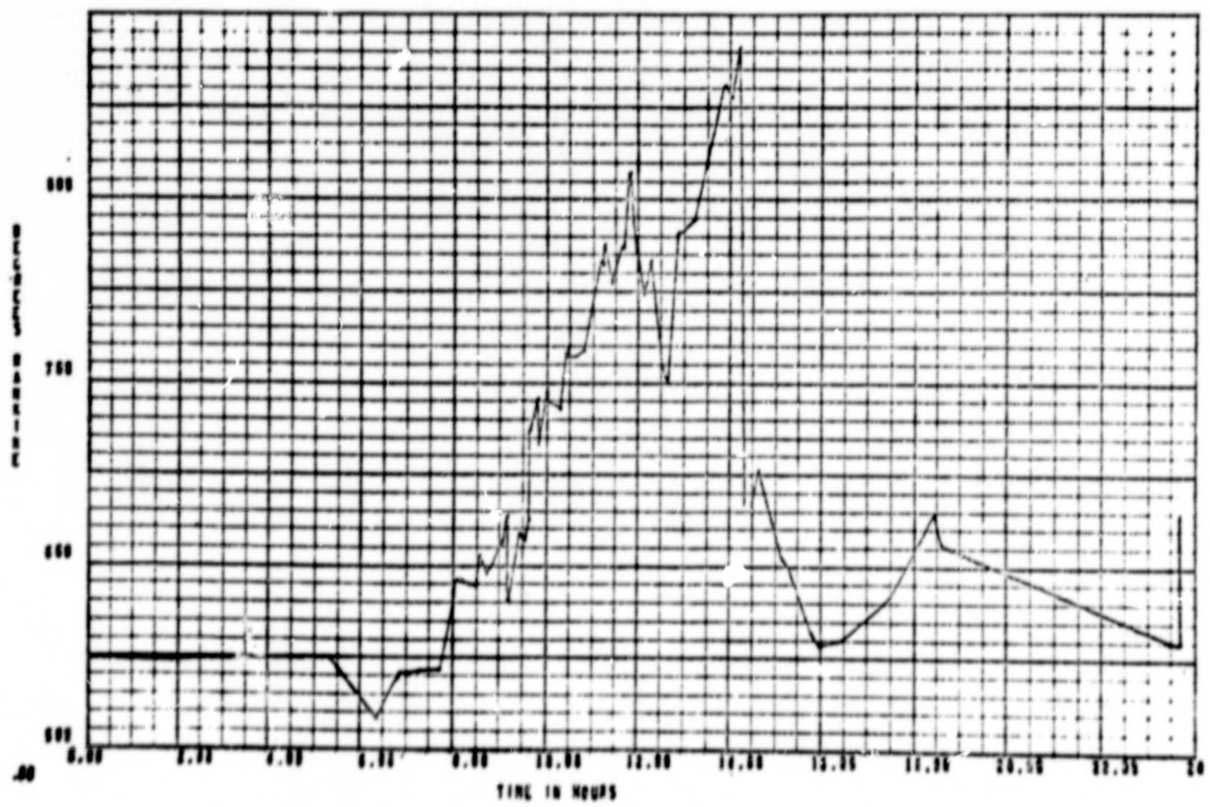

Figure 26 - Hex-Head 3 Temperature, S/N 47 Transducer

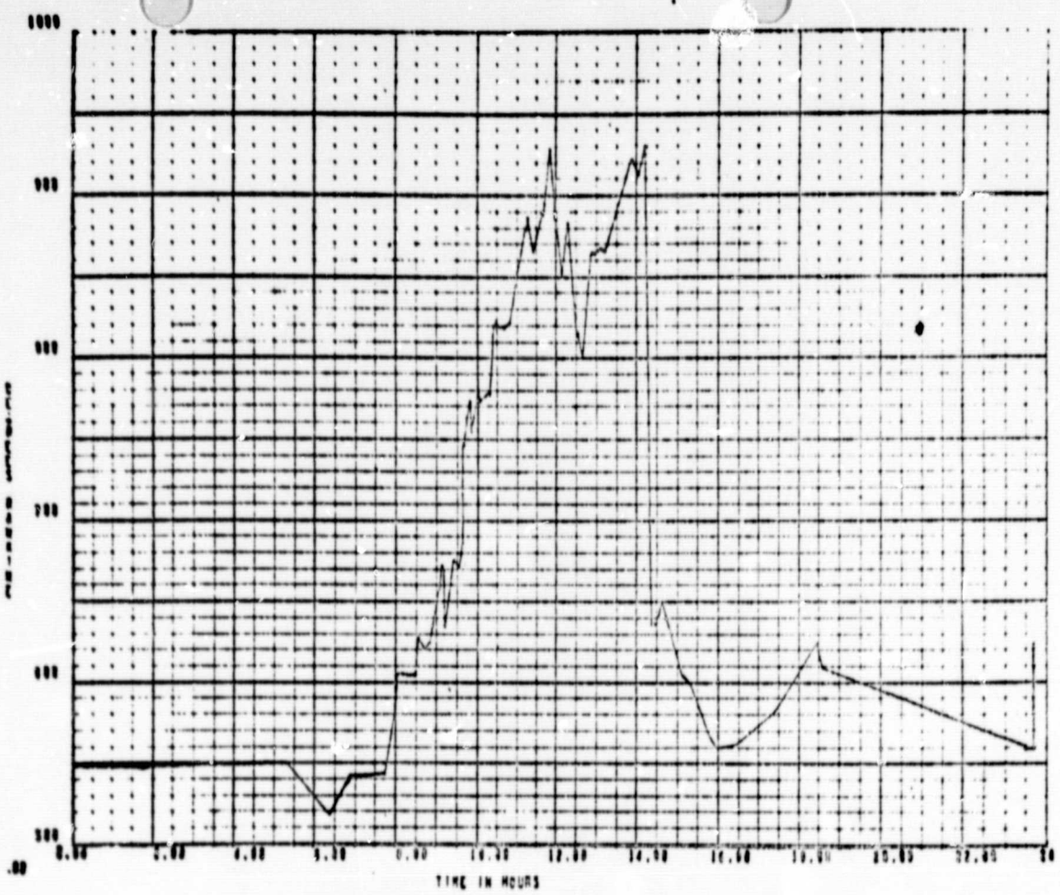

Figure 27 - Hex-Head 4 Temperature, Instrumented Transducer

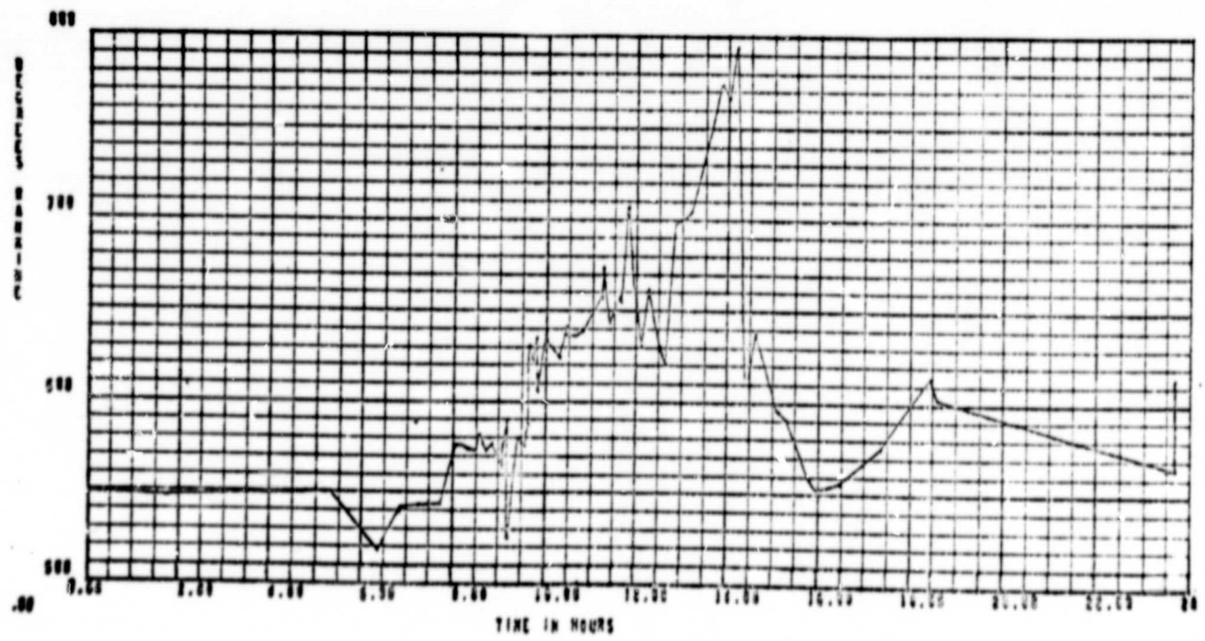

Figure 28 - Hex-Head 6 Temperature, S/N 50 Transducer

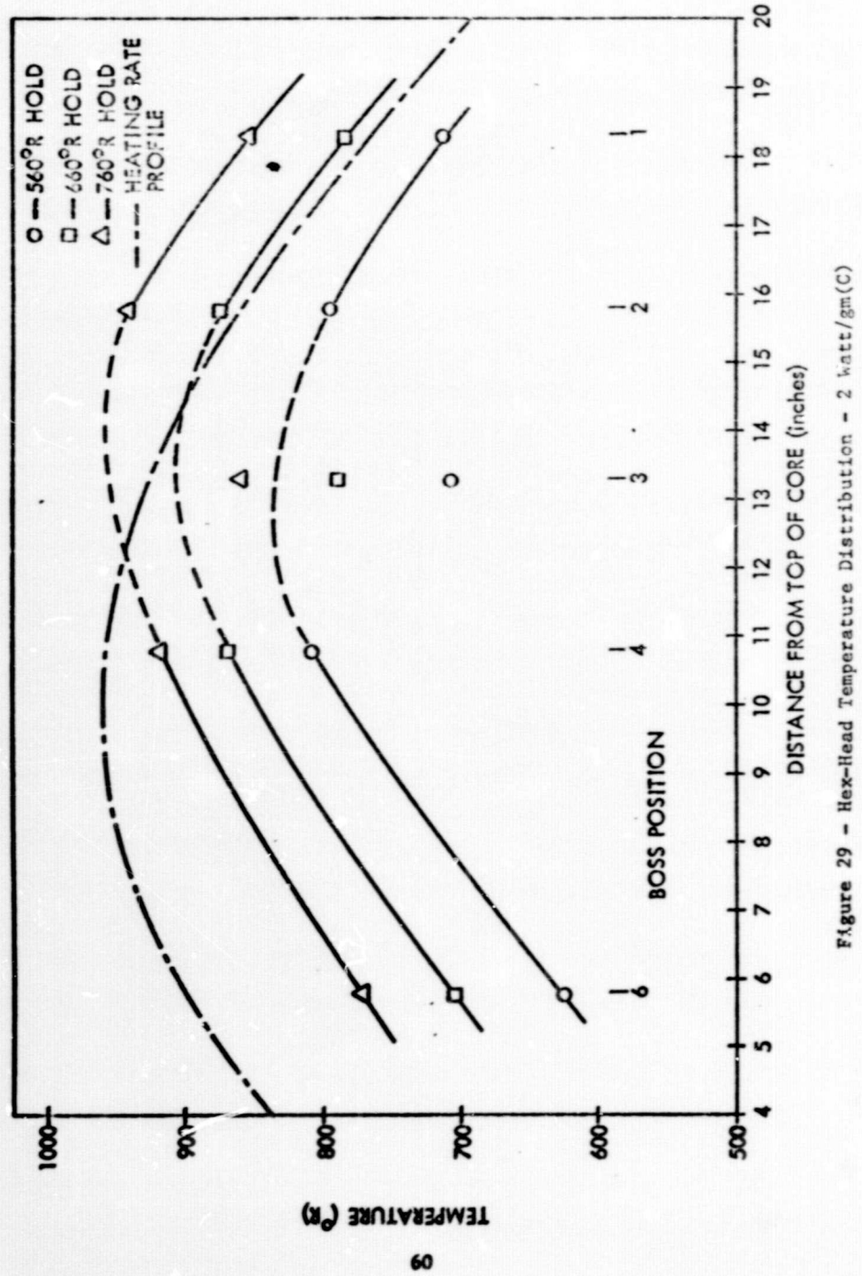

Figure 29 - Hex-Head Temperature Distribution - 2 watt/gm(C)

a negative unidirectional error. The data shown in Figure 29 appear to be in good agreement with the exception of hex-head 3 temperatures, but may represent lower than actual temperatures. The dashed lines in Figure 29 indicate the approximate temperature of position 3 hex-head based on the extrapolation of other hex-head data.

Comparison of the hex-head temperature distribution and the heating-rate profile shows a significant difference in the location of the profiles with respect to distance from the top of the core. If the heating rate profile is assumed to be correct then it must be concluded that the thermocouple data are grossly in error. However, the converse can also be assumed implying that the downward shift of the flux profile was greater than predicted. Correlation of temperature gradient data and transducer zero shift data, discussed in subsequent sections with the corrected heating rate values, indicate that the corrected heating rate values are valid. It must be concluded that the hex-head thermocouple data are in error and that the shift in profile is coincidental.

3. Diaphragm Temperatures

Transducer internal temperature data were obtained during the test from the two instrumented transducers located in fixture boss positions 1 and 4. The instrumented transducers were included in the test to obtain information of the temperature gradients across the diaphragm as a function of nuclear heating rate and to verify the pretest thermal analysis model. The internal thermocouples 38, 39, and 40 were installed to monitor the center diaphragm temperature of 1 and 4 transducers and the edge of transducer 4 diaphragm respectively. The temperature data for the three thermocouples are shown plotted in Figure 30, 31, and 32 and are similar in profile to the boss temperature data shown previously in Figures 16 through 20.

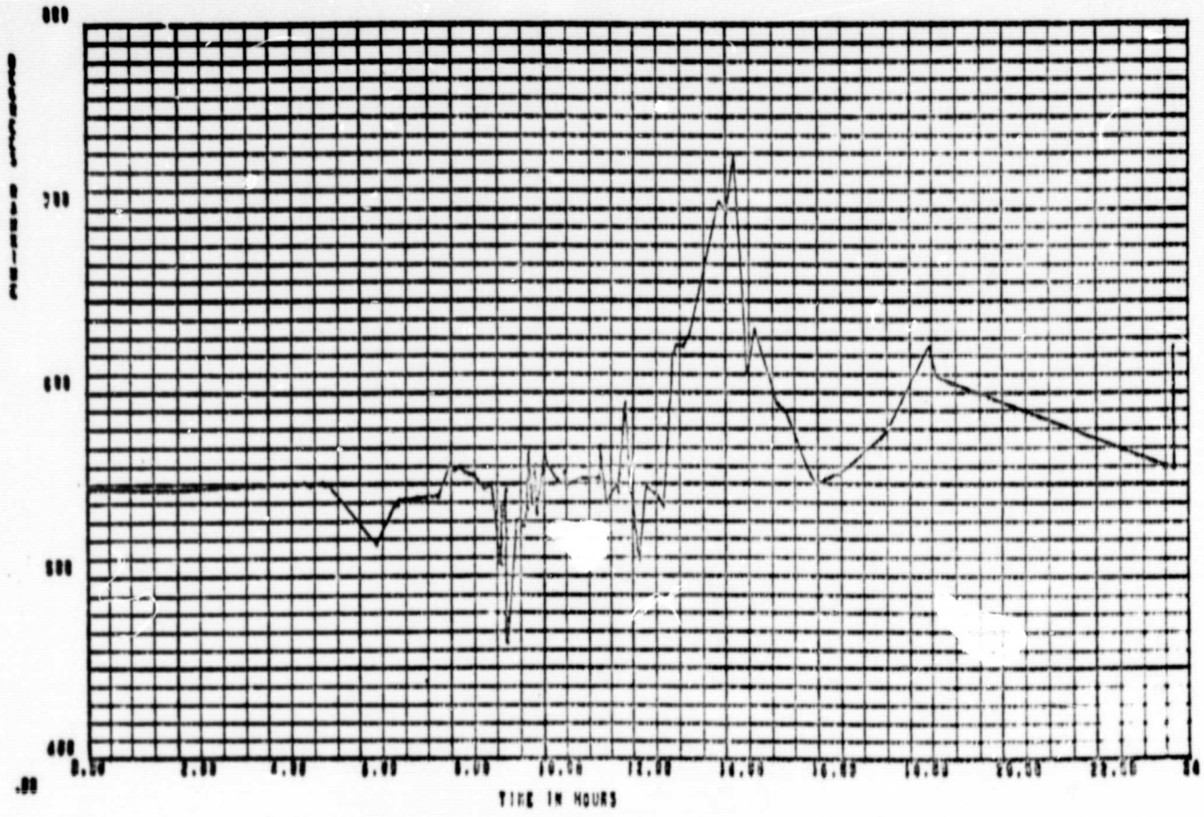

62

Figure 30 - Internal Temperature 38, Instrumented Transducer Boss 1

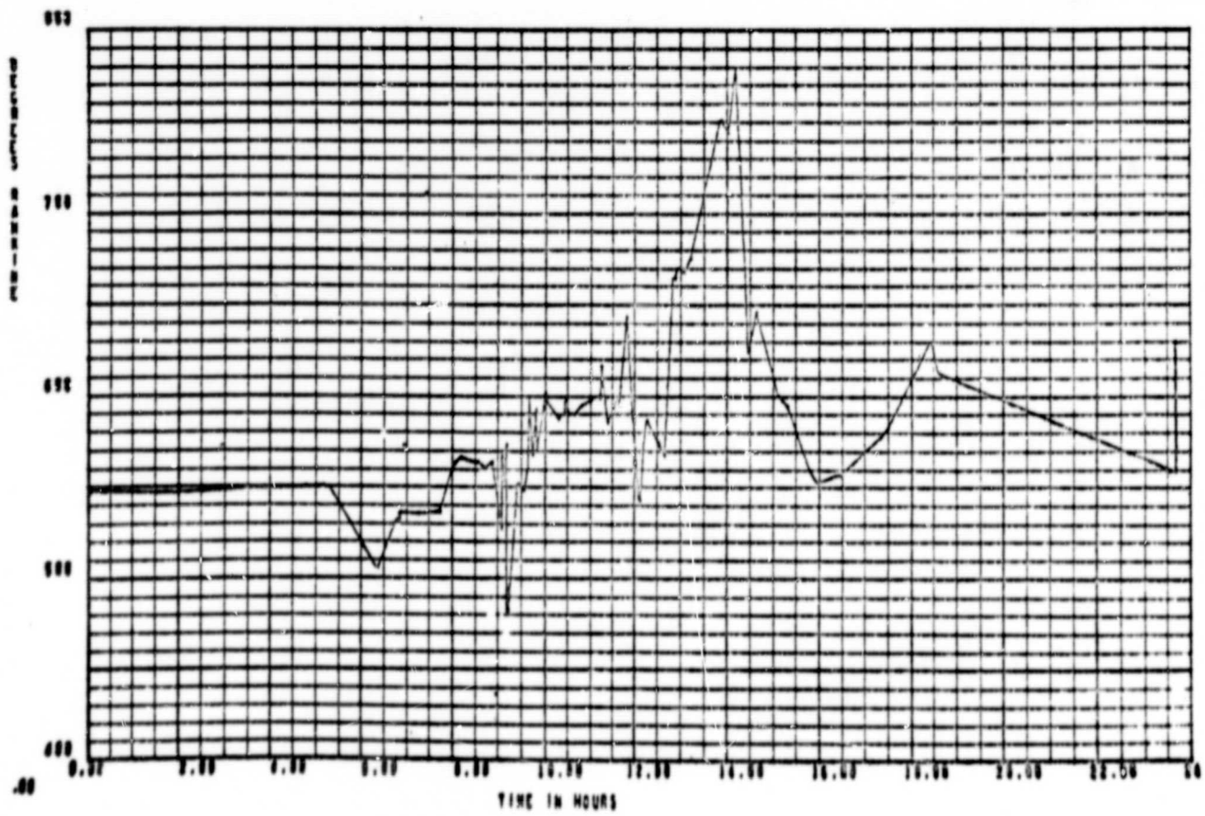

63

Figure 31 - Internal Temperature 39, Instrumented Transducer Boss 4, Diaphragm Center

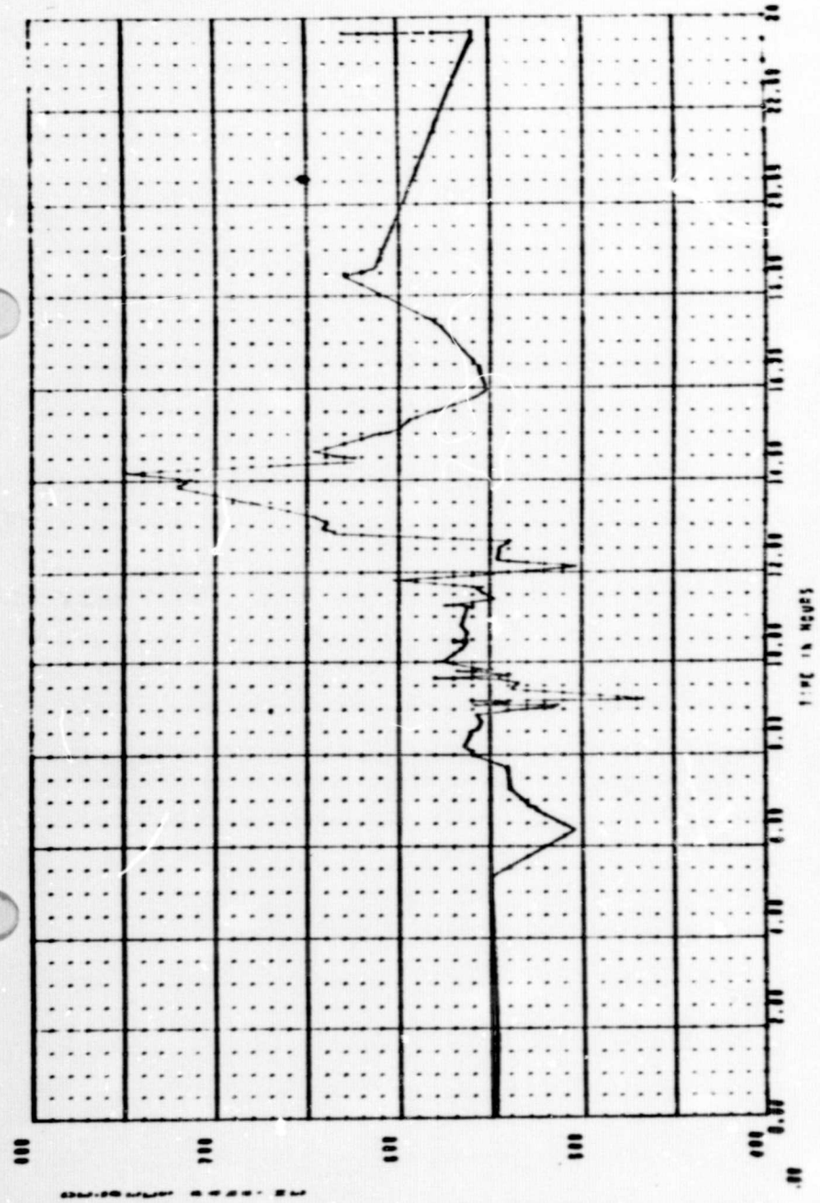

Figure 32 - Internal Temperature 40, Instrumented Transducer Boss 4, Diaphragm Edge

Correlation of the internal temperatures with the corresponding boss temperatures indicates that an anomaly is present in this portion of the test data. The data indicate a greater temperature gradient from the edge to the center of transducer 4 diaphragm than the gradient from the boss thermocouple to the center of the diaphragm. Figure 33 shows the respective locations of boss 4 thermocouples.

From the theory of heat conduction, it would not appear possible for the temperature of the boss to be greater than the temperature at the edge of the diaphragm that is further from the coolant. Selected data from the boss thermocouples 4A and 4B, and from the transducer internal thermocouples 39 and 40 are shown tabulated in Table 9. The temperatures noted in Table 9 show the boss temperature 4B to be consistently higher than the diaphragm edge temperature, 40. In addition, the gradient across the diaphragm, 40 to 39, is greater than the total gradient from the boss temperature, 4B, to the center of the diaphragm.

The conclusion that the leads from thermocouple 4B and those from 40 were inadvertently interchanged or mislabeled is supported by the following arguments.

a. Since the boss thermocouples 4A and 4B were symmetrically located with respect to heat generation, similar temperatures were expected. Examination of the data in Table 9 shows that there is closer agreement between the temperatures indicated by 4A and 40 than there is with 4A and 4B.

b. In the pretest thermal analysis, a conservative film coefficient was used between the threads of the transducer and the boss with the result that the measured gradient in this region would be expected to be smaller than the analytical gradient. Comparison of the data in Table 9

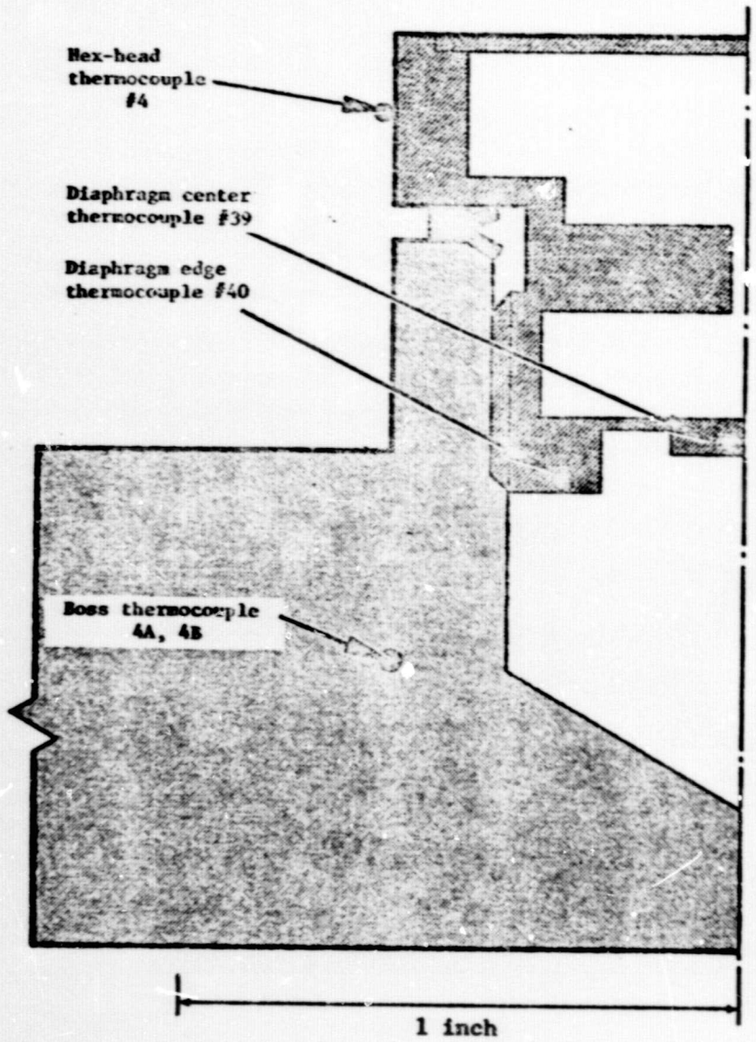

Figure 33 - Location of Boss 4 Thermocouples

TABLE 9

COMPARISON OF BOSS 4 TEMPERATURES

CDT Time hr:min	Elapsed Time Hours	Heating Rate W/GM(C)	Thermocouples 4A[a] °R	4B °R	40 °R	39 °R
1440	10.4	2.04	555	573	566	593
1445	10.5	2.04	552	572	562	586
1450	10.6	2.04	550	572	562	590
1500	10.8	2.04	553	572	562	591
(Analytical)		(2)	(560)	(560)	(590)	(610)
1523	11.2	2.62	560	580	562	575
1530	11.3	2.62	535	563	543	576
1540	11.4	2.62	533	566	540	575
1551	11.6	2.76	544	575	554	595
1605[b]	11.9	2.76	-	558	529	563
1620	12.1	2.76	497	535	503	541
1629	12.2	2.76	538	569	543	582
(Analytical)		(3)	(560)	(560)	(603)	(603)
1645	12.5	2.00	529	564	538	565
1651	12.6	2.00	526	562	538	568

(a) Readings from Bristol Controller record.

(b) At 1600 the LN_2 pump was turned on causing decreases in all temperatures.

shows that the difference between 4A and 40 is negligible while the difference between 4A and 4B (assuming 4B is the edge of the diaphragm) is nearer the predicted gradient.

c. Since transducer 1 was also instrumented, it would be expected that the gradient between the boss thermocouple and the center of the diaphragm would be similar for both 1 and 4 except for possible differences in magnitude resulting from the differences in heating rates. Figure 34 shows the gradient between 4B and 39 during the test. Figure 35 shows the gradient between boss 1 and 38, the center of transducer 1 diaphragm. Comparison of the two shows little correlation. Figure 36 shows the gradient between 40 and 39, assuming 40 is the boss temperature. Comparison of the resultant gradient with the gradient shown in Figure 35 for transducer 1 shows very close agreement both in profile and magnitude. The gradient for 1 is slightly lower throughout the test because of the lower heating rates at the end of the fixture.

Therefore, all further discussion and analysis is predicated on the assumption that thermocouple 4E and 40 were interchanged.

4. Temperature Gradients

Within the temperature range of the test, temperature gradients between various parts of the transducer and the heat sink are approximately linear functions of the thermal path lengths and heating rates at each location. If the thermal path lengths are assumed to be equal for each of the transducer locations, then it should be possible to correlate the observed temperature gradients and heating-rate data with the analytical thermal model presented in Appendix A.

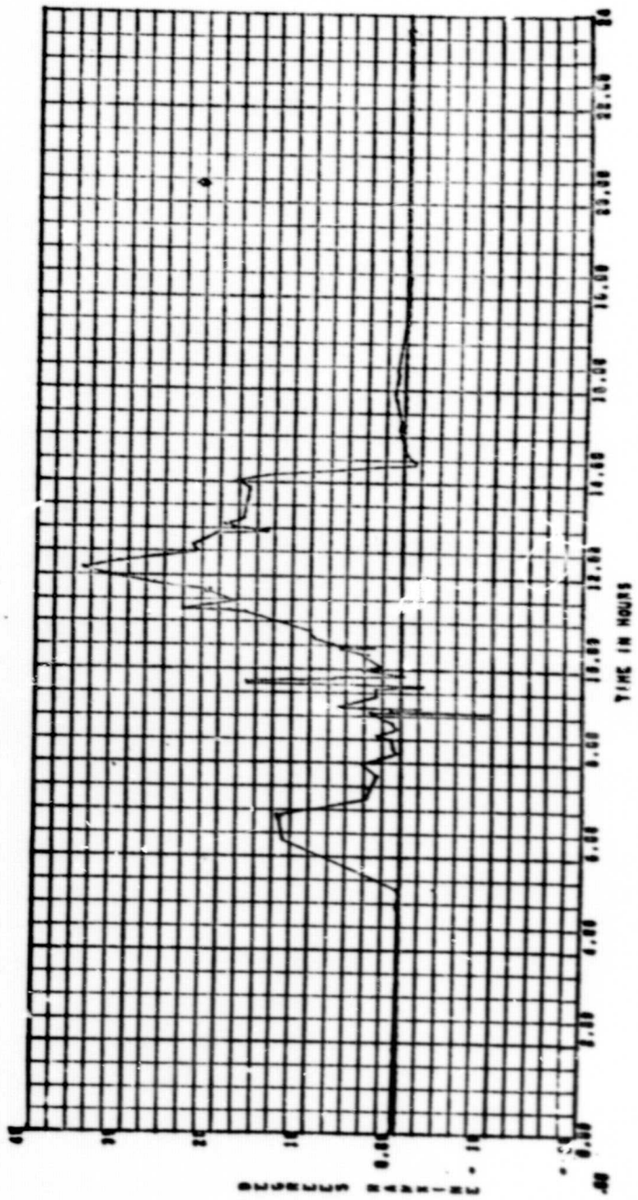

Figure 34 - Temperature Gradient, 4B and 39

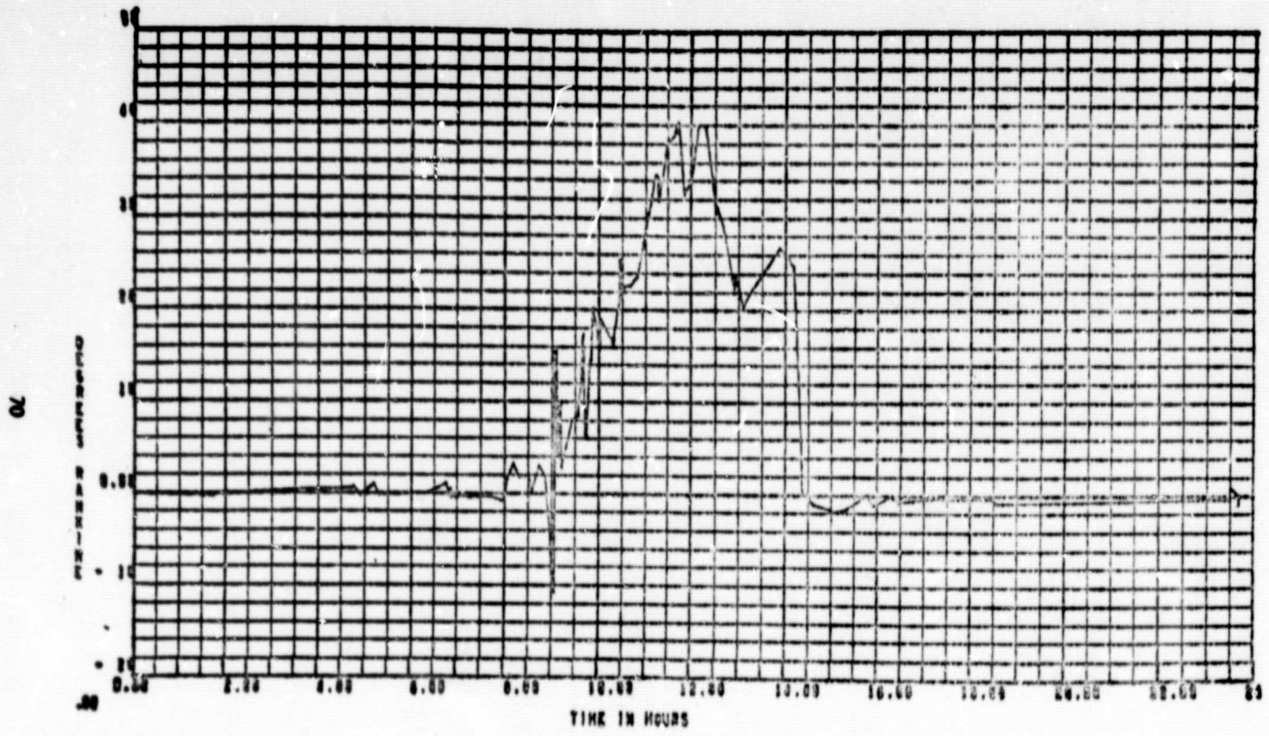

Figure 35 - Temperature Gradient, Boss 1 and 38

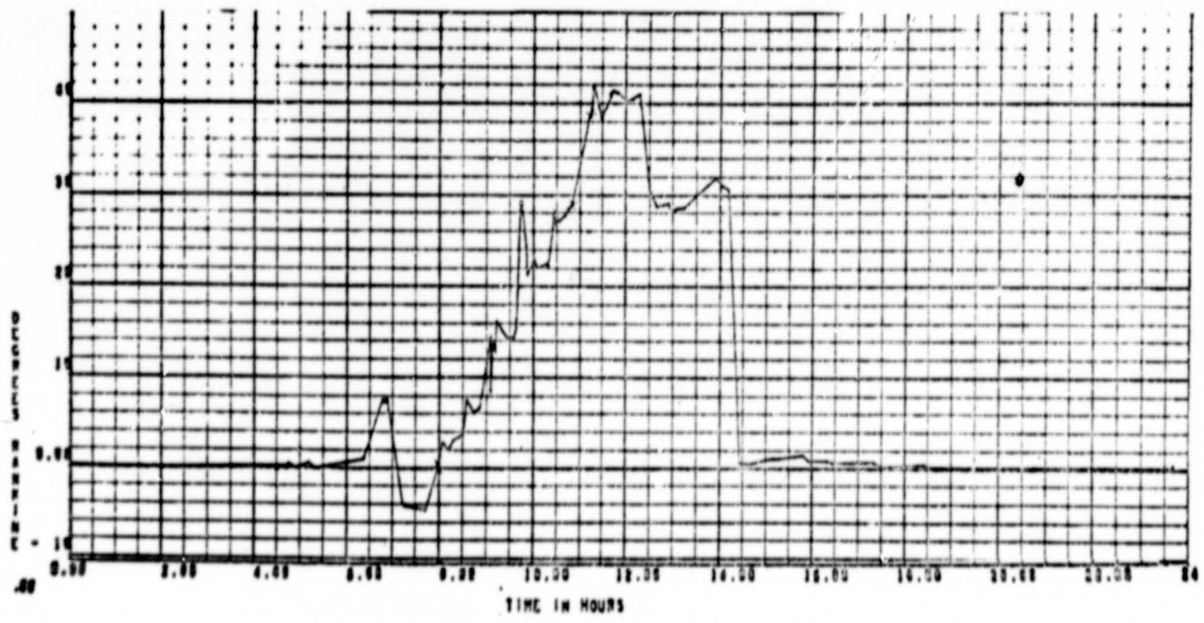

Figure 36 - Temperature Gradient, 40 and 39

Measured temperature gradients determined from the various combinations of thermocouples are shown tabulated in Table 10 and are plotted in Figures 37, 38, and 39 as a function of the corrected heating rates from Table 7, with the corresponding predicted temperature gradients from Appendix A. With the assumptions stated, correlating the measured gradients with the heating rates should produce a single straight-line curve with all data points on or near it. However, examination of the data in Figures 37 and 38 shows a significant divergence of the data and, with the exception of Boss 2 gradient, poor correlation with the predicted gradient curve.

The most probable cause of the poor correlation is the uncertainty of the boss and hex-head temperature measurements, as noted previously. Both sets of measurements include errors of unknown magnitude that, when added together, decrease the magnitude of the observed gradient. The gradient for Boss 3, shown in Figure 37, is known to be grossly in error and, as expected, shows the greatest deviation from predictions.

The boss-to-diaphragm-center gradients shown in Figure 38 also indicate that the boss thermocouples are in error. Since the diaphragm thermocouple junctions are welded to the diaphragm material, the resultant temperature is a fairly accurate representation of the true temperature. Errors in the boss measurements will decrease the observed gradient resulting in poor correlation with the predicted gradient, and also between gradients if the errors are not equal.

The diaphragm center-to-edge gradient shown in Figure 39 shows good correlation with the predicted gradient for heating rates up to 1.6 watts/gram(C). The good correlation is because both thermocouple junctions are welded to the diaphragm, thereby minimizing errors. However, above 1.6 watts/gram(C), the data show a decreasing trend that deviates from the predicted linear relationship. Since the other gradients do not reflect a corresponding decrease, the cause is attributed to a decrease in the diaphragm

TABLE 10

MEASURED TEMPERATURE GRADIENTS

Reactor Power (MW)	Boss to Hex-Head					Boss to Diaphragm Center		Diaphragm Edge to Center
	#1	#2	#3	#4	*#5	#1	#4	#4
1.3	28	43	26	42	34	7	4	3
1.98	42	64	40	66	53	7	9	6
3.62	87	124	71	123	98	13	14	12
5.83	139	194	106	196	157	21	23	18
7.3	184	248	132	256	200	27	29	18
9.4	247	325	175	320	247	38	38	16
9.9	261	348	178	340	258	39	40	9

*Based on interpolation of hex-head temperature.

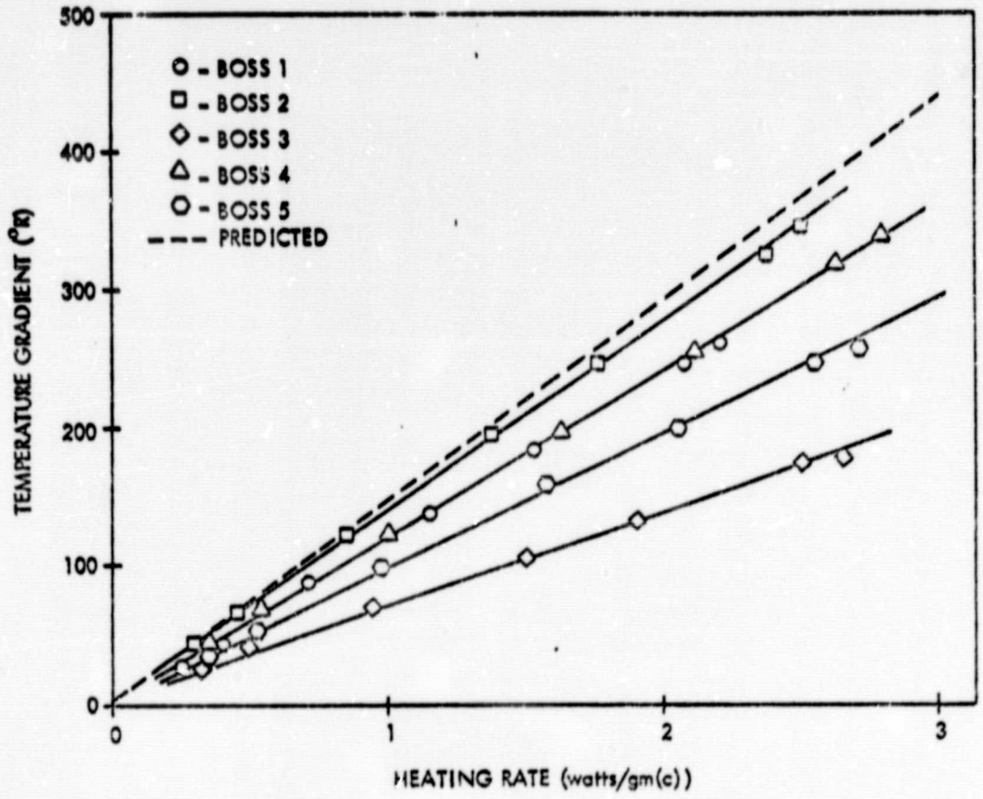

Figure 37 - Temperature Gradients, Boss to Hex-Head

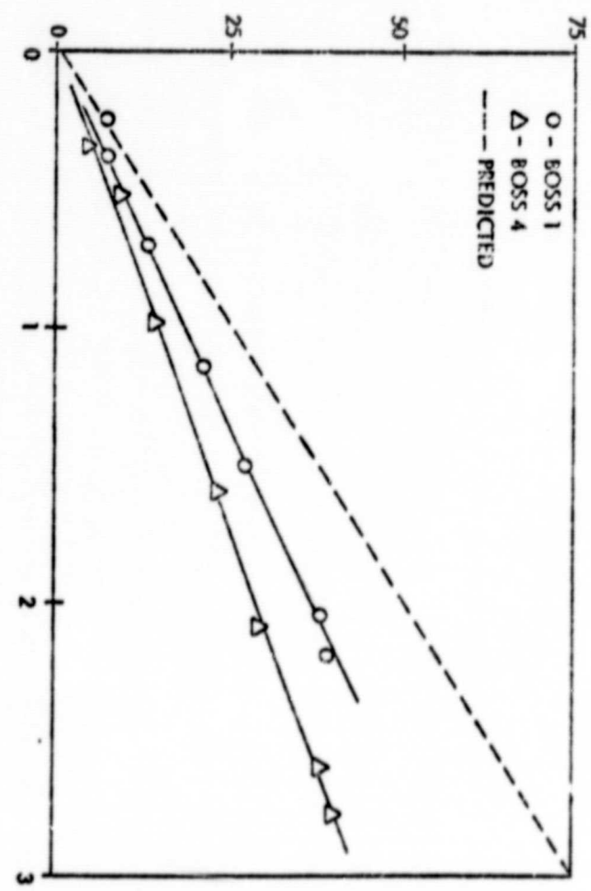

Figure 38 - Temperature Gradients, Boss to Diaphragm Center

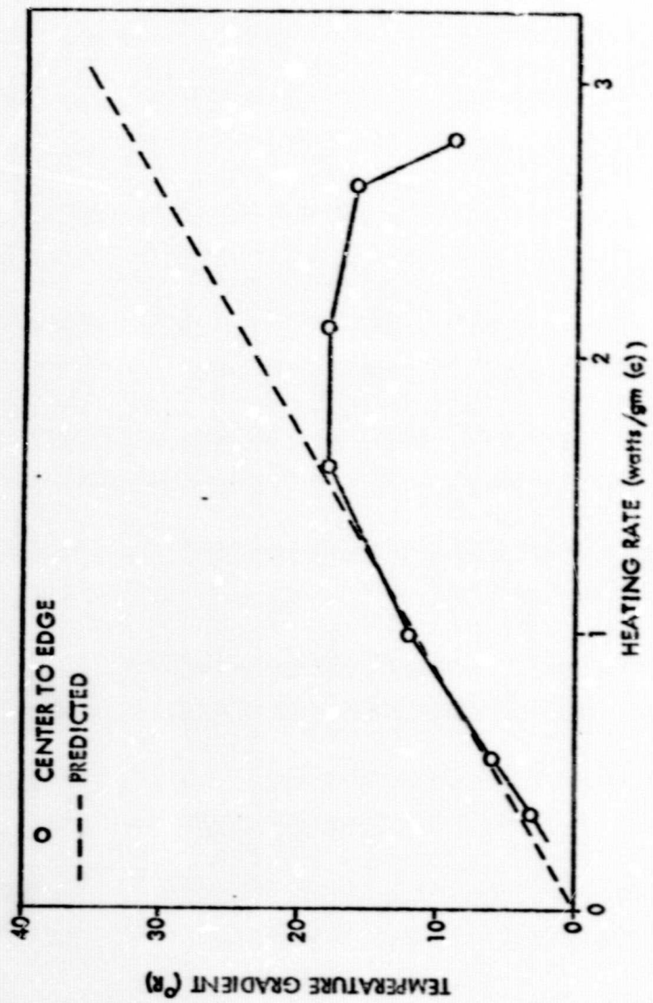

Figure 39 - Temperature Gradients, Diaphragm Center to Edge

center temperature caused by heat loss through conduction to the pressurization gas in the fixture. The decrease in temperature gradient corresponds to the increase in cryogenic gas coolant flow to the fixture during the higher heating rate portion of the test.

5. Cable Temperatures

Temperature data obtained from the two internal junction thermocouple cables that are mounted on the bottom of the test fixture are shown plotted in Figures 40 and 41. Each cable had an ungrounded thermocouple junction located approximately 1 ft from the cable end and was attached to the fixture with weldable thin-metal strips as shown previously in Figure 7.

The difference in the two measurements is attributed to the difference in the thermal paths from the sensor junction to the coolant manifold, relative to the position of the thin-metal strip. The metal strips were located approximately 2 in. apart and with a tolerance of ± 0.5 in. on the sensor junction position within the cable, the thermal path length could vary up to an inch between cables.

6. Conclusions

Temperature data obtained during the test were not of good quality except for the data for the three chromel-alumel thermocouples that were welded to the two instrumented transducer diaphragms. The poor control of the fixture temperature during the test introduced severe fluctuations in the temperature data, limiting comparison of temperatures during specified times to relative averaged values.

The possibility was investigated that the heating-rate data shown in Table 7 were in error and that the power profile had shifted downward as indicated by the hex-head temperature distribution profile shown in

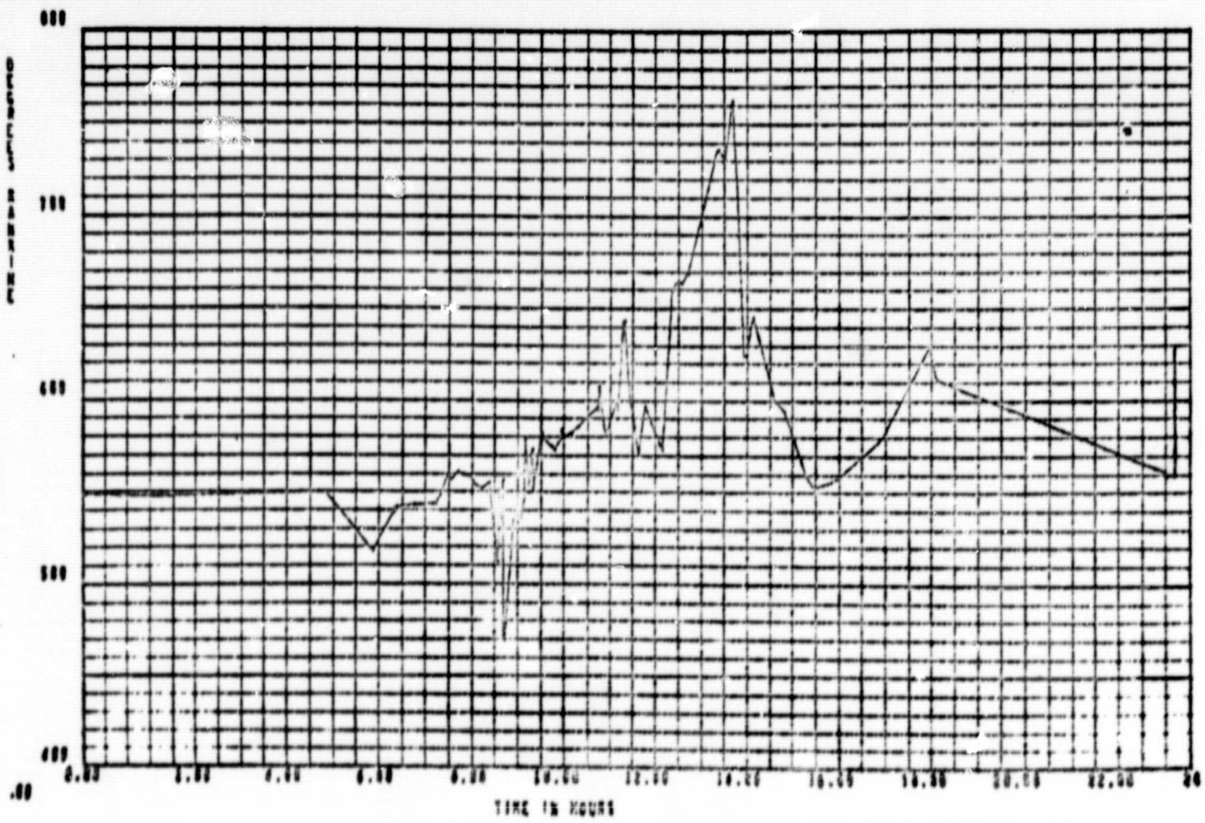

Figure 40 - Internal Temperature, Cable A

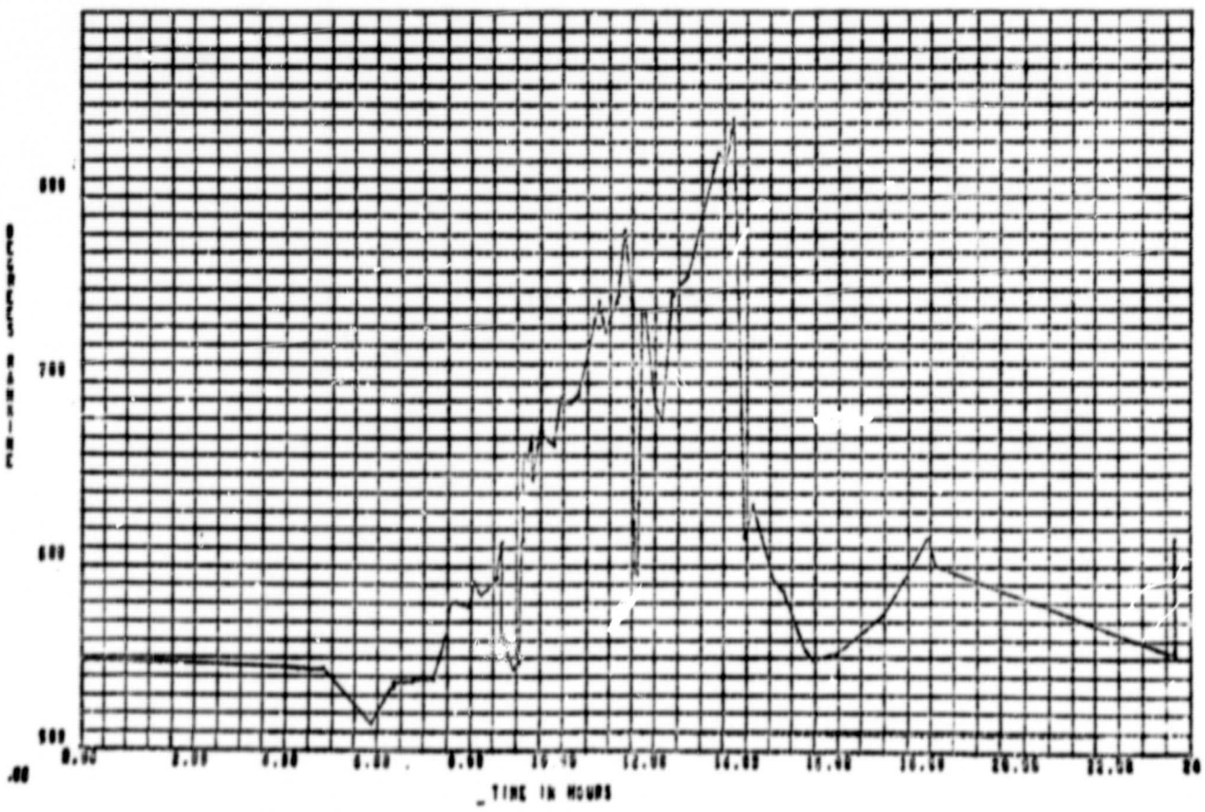

Figure 41 - Internal Temperature, Cable B

Figure 29. Heating rate data obtained from this assumption were used to correlate the gradient data shown in Table 10. However, no better correlation was obtained and it must be concluded that because of errors of unknown magnitude in the boss and hex-head temperature measurement, correlation of the observed gradients with heating rate data is inconclusive.

C. SIMULATED TRANSDUCERS

Performance measurements of an active transducer system provide total measured values that include the effects of radiation and temperature on both the cable and transducer. Since it is difficult to assess transducer characteristics without the use of cables, the transducer performance can only be inferred by subtracting the contribution of the cables in the same environment. However, measurements obtained with cables exposed to the nuclear environment will only provide data describing the radiation effect on the electrical properties of the cable but not necessarily the effect on a total instrument system. Previous test results have indicated that observations are dependent on the characteristics of the instrument and of the signal conditioning and monitoring equipment used.

The principal radiation effect on electrical cables is the decrease of insulation resistance with increasing radiation levels. Experiments conducted by Gerald C. Huth (Reference 9) indicate that the increase in the electrical conductivity of the insulating material is a transient gamma induced phenomenon that is proportional to the gamma level.

The interaction of gamma rays and matter results in the generation of free electrons attributed to three primary effects; photo-electric, Compton, and pair production (Reference 10). The free electron contribution of each effect is highly dependent on the irradiated material and the energy spectrum of gamma photons, but all effects are directly proportional to the gamma rate. In the field of an impressed voltage, the excess electrons are carried away as they are generated and the combined effects can be observed as an increase in the conductivity of the material. In materials that exhibit high electrical conductivity, such as metals, the excess electrons pose no problem. In low conductivity materials, such as the MgO insulation used in the metal sheathed cables, the increase in conductivity can cause shunting of the transducer affecting its accuracy, and makes possible generation of spurious signals.

In the absence of an impressed voltage, the free electrons will eventually recombine until a state of equilibrium is attained between the generation and recombination of electrons that is proportional to the gamma rate. In effect, the cable and transducer become charged like a capacitor. The application of a high voltage will carry out the excess electrons and may be observed as a surge in the output current, resulting in an erroneous or spurious signal.

1. Insulation Resistance

All insulation resistance measurements, with the exception of simulated System No. 1, were obtained by applying a 45 vdc potential between the cable sheath and the conductors, and monitoring the leakage current with a Hewlett-Packard 412-B multimeter. A 50 vdc Weston Megohmmeter was used throughout the test to measure the insulation resistance of simulated System No. 1. The insulation resistance values, calculated from the current-voltage relationship are presented in Table 11 for the active and simulated transducer output cables, with the respective reactor power levels and test times. In addition, the insulation resistance data for the two ungrounded thermocouple cables, A and B, are also included.

The data for the simulated system cables and thermocouple cables A and B are shown plotted in Figure 42. The data show the effects of the core residual-gamma radiation from time 3.7 hr, when the fixture was inserted into the core, to 6.5 hr, the aborted start. Also evident is the recovery of the insulation resistance after termination of irradiation at 14.0 hr. During the period of irradiation, between 8.0 hr and 14.0 hr, the data show the insulation resistance of cables to be increasing while the gamma level is also increasing. This apparent anomaly is contrary to expected behavior of the cable insulation resistance in a high-gamma field.

The anomaly can be explained by considering the location of the cables on the fixture. All of the simulated system cables were

TABLE 11

INSULATION RESISTANCE OF CABLES WITH 300-FT EXTENSIONS

Time Hours	Power (Mw)	Insulation Resistance (Megohm) S/N 47	S/N 50	S/N 61	S/N 63	Dummy 1[B]	Dummy 2	Dummy 3	Cable A	Cable B
-2.6	0	190	99	111	117	7.4K	50	157		
-2.3	0	190	99	114	117	8.6K	50	157		
-0.9	0	198	103	117	117	7.4K	58	163	300	250
0.3	0	198	111	114	120	8.6K	49	169	321	264
0.9	0	217	114	120	123	$>10^4$	60	169	375	300
1.5	0	217	114	120	123	7.4K	60	175	346	321
1.8	0	217	111	120	123	8.6K	64	175	346	321
2.8	0	207	108	126	120	$>10^4$	66	182	333	321
4.1	BKG	207	103	130	126	$>10^4$	41	198	321	346
4.9	BKG	147	75	91	86	$>10^4$	38	111	225	264
5.3	BKG	142	73	78	86	$>10^4$	46	106	236	250
6.3	BKG	64	38	33	33		22	35	195	204
6.6	Start Up	53	27	23	25		21	38	92	68
7.1	BKG	53	27	23	27	8.6K	20	41	83	62
7.5	BKG	67	28	28	30		23	41	90	68
8.3	1.30	5.2	5.5	8.0	9.9	$>10^4$	23	38	71	72
8.8	1.98	4.1	4.3	6.7	7.3		23	33	66	80
9.3	3.62	2.6	3.1	5.5	6.5	$>10^4$	33	57	107	150
10.1	5.83	1.9	2.5	5.1	5.8		52	73	214	250
10.8	7.3	1.6	2.1	4.6	5.5	$>10^4$	46	61	173	204
12.3	9.9	1.2	1.6	4.3	4.3		33	38	100	125
12.6	7.13	1.6	2.1	4.5	6.1	$>10^4$	33	46	107	122
13.2	7.13	1.6	2.0	4.6	4.8	$>10^4$	38	58	112	132
14.1	7.13	1.2	1.8	3.5	3.5		41	58	132	145
14.3	BKG	12	13	38	27	$>10^4$	50	71	187	167
14.6	BKG	17	27	38	31		70	100	250	225
15.9	BKG	35	31	75	66	$>10^4$	85	128	320	300
16.5	BKG	38	35	85	77	$>10^4$	98	153	375	320
17.5	BKG	46	38	70	77	$>10^4$	96	200	264	320
18.6	0	90	64	82	87	$>10^4$	71	230	320	375
27.7	0	139	96	115	124		62	230	320	346
28.5	0	170	98	164	124		65	230		
29.3	0	164	92	139	118		90	209		
29.9	0	164	98	153	121		75	242		
30.4	0	170	96	135	124		84	230		
31.1	0	167	92	125	125		60	166		

[B] Measured with 50 vdc Megger

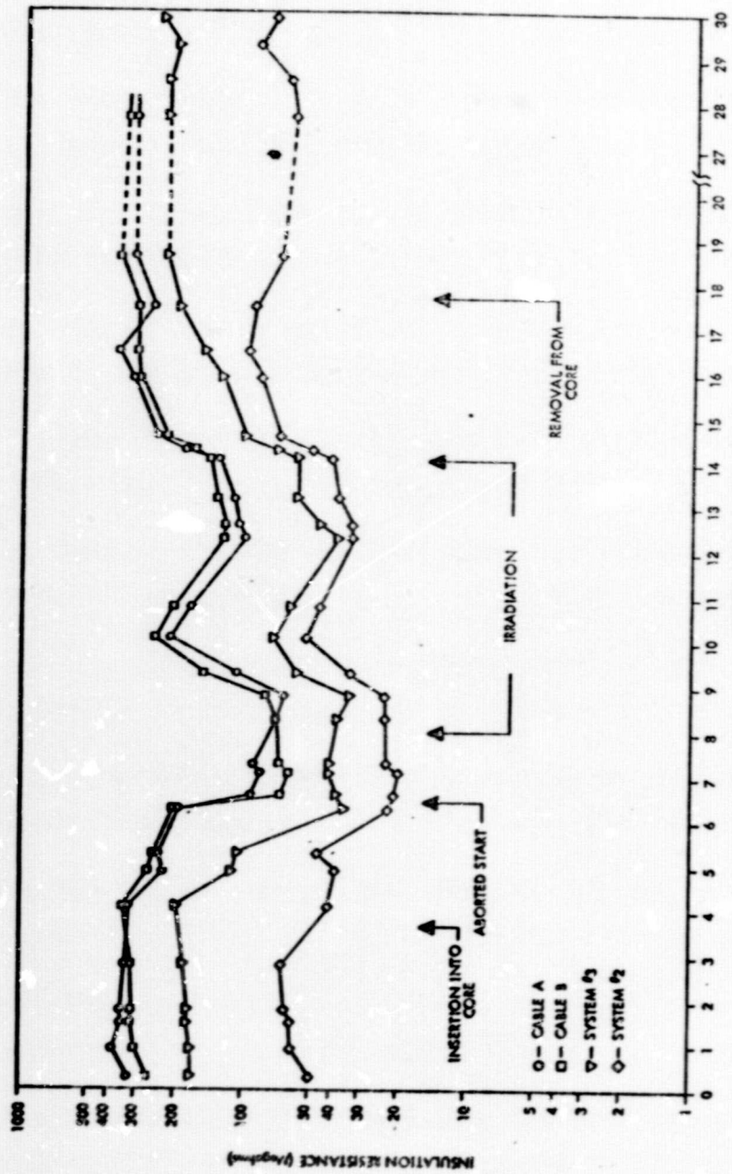

Figure 42 - Simulated Transducer Cable Insulation Resistance

attached to the GN_2 coolant inlet manifold on the bottom of the test fixture as shown previously in Figure 7. Table 12 is the GN_2 coolant system data and the insulation resistance values indicate that decreases in GN_2 coolant temperatures coincide closely with the observed increases in insulation resistance values. Since cable insulation resistance varies inversely with temperature, the most probable cause of the observed anomaly is that the effects of the cryogenic coolant masked the effects of gamma radiation on the cable MgO insulation material. As a result, the masking of the irradiated cable data by the cryogenic temperatures during the test invalidates the original intent of subtracting the simulated cable effects from the active transducer data. However, the results are significant since they show that the effects of gamma radiation and temperatures on the MgO insulation are independent and additive. By controlling the cable temperature through cryogenic cooling, insulation resistance values are 5 to 10 times higher.

The data for simulated System No. 1 insulation resistance (Table 11) appear to be invalid because of the complete lack of radiation effects. The cause is suspected to be a discontinuity between the metal sheath of the test cable and the braided shield of the flexible extension cable.

2. Bridge Resistances

Input and output bridge resistance data for simulated System No. 1 are presented in Table 13. Input and output bridge resistance data for simulated Systems No. 2 and No. 3, obtained with the automated data system, exhibited two anomalous characteristics throughout the test. The first is the occurrence of periodic spikes in the data and the second, decreasing trend of the resistance data during the test. The significance of the data spikes is discussed in a subsequent section. To illustrate the decreasing trend, the data were thinned to include only those values corresponding to the zero pressure cycles. These data are shown in Figures 43 to 46 as deviations in percent of the pretest averages for Systems No. 2 and No. 3 input and output bridge resistances, respectively.

TABLE 12

COOLING-SYSTEM DATA

Time	Power (Kw)	LN_2 Flow Rate (gpm)	GN_2 Temp[a] (°F)	GN_2 Pressure[a] (psig)	Boss 4-A Temp (°F)
1217	1.30	8.5[b]	33	20	90
1219	1.30	11.0[b]	43	16	104
1300	1.98	9.5[b]	17	20	98
1346	3.62	6	-35	44	68
1405	5.83	7.5	-35	41	116
1431	5.83	8.5	-76	9	95
1447	7.3	9.0	-105	25	92
1512	7.3	10.0	-110	44	98
1537	9.4	11.5	-160	59	77
1600	LN_2 pump turned on				
1609	9.87	13.2	-135	59	82
1633	9.87	10.5	-125	59	72
1650	7.13	9.5	-90	44	66
1721	LN_2 pump turned off (Boss Temp 200°F)				
1730	7.13	7.5	-55	34	152

[a] Sensors located in the elbow at test fixture inlet.
[b] Dump valve at exit of heat exchanger partially open.

TABLE 13

INPUT-OUTPUT BRIDGE RESISTANCE DATA, SYSTEM NO. 1

Applied Voltage = 20V Heating Rate = 0.28 W/g(C)-MW

TIME (CDT)	HEATING RATE [W/g(C)]	BRIDGE RESISTANCE INPUT (ohm)	OUTPUT (ohm)
0416	0	-	-
0426	0	-	-
0544	0	-	-
0559	0	-	-
0903	BKG	1512	1512
0925	BKG	1512	1512
1100	BKG	1514	1514
1220	0.364	1514	1514
1226	0.364	1514	1514
1250	0.554	1514.5	1514.5
1324	1.01	1514	1514
1408	1.63	1514	1514
1446	2.04	1514	1514
1530	2.63	1514	1514
1617	2.77	1514	1514
1647	2.0	1514	1514
1715	2.0	1514	1514
1810	2.0	1512	1512
1845	BKG	1514	1514
1925	BKG	1514	1514
2005	BKG	1514	1514
2041	BKG	1514	1514
2151	BKG	1514	1514
2245	0	1514	1514
0748 *	0	1514	1514
0944 *	0	1514	1514
1010 *	0	1514	1514

* 22 August 1967

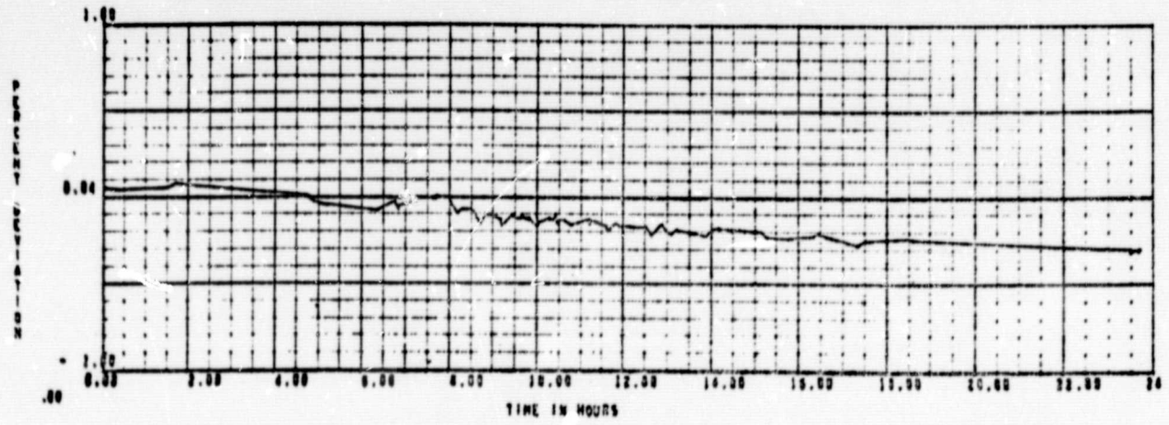

Figure 43 - Resistance Deviation, System 2 Input

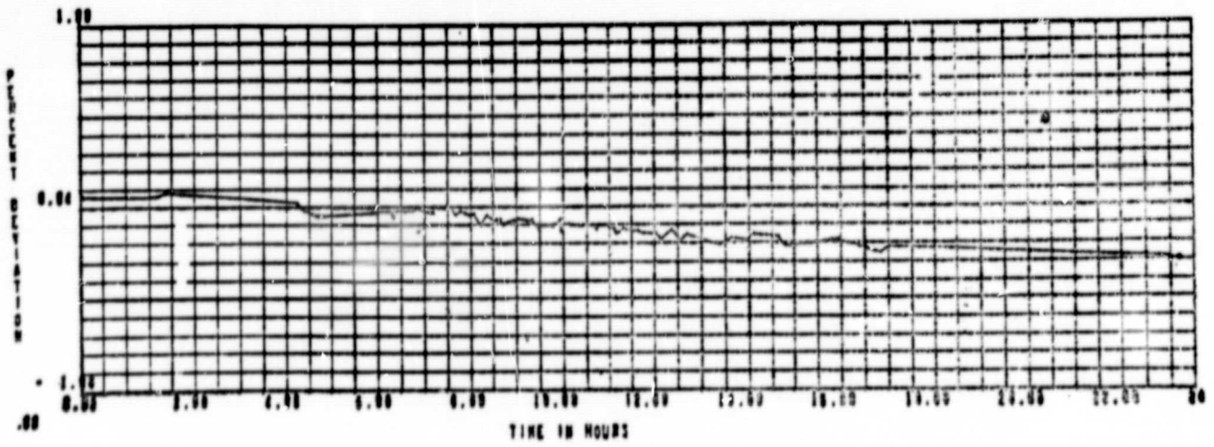

Figure 44 - Resistance Deviation, System 2 Output

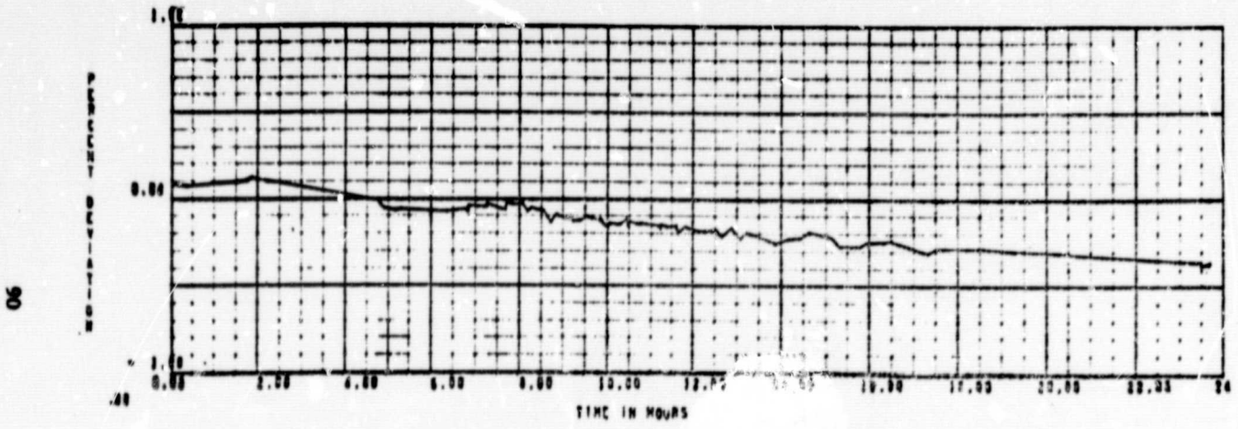

Figure 45 – Resistance Deviation, System 3 Input

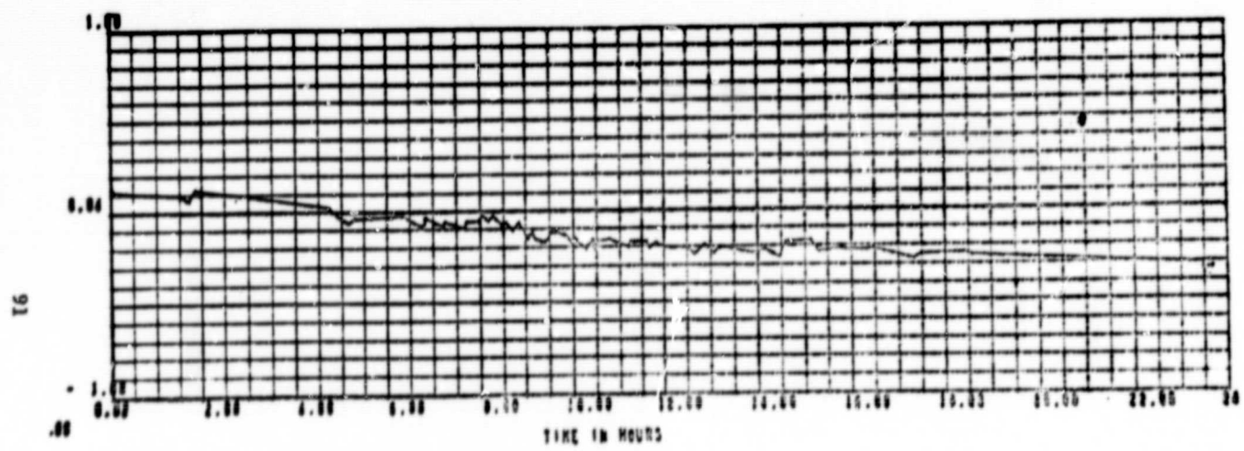

Figure 46 - Resistance Deviation, System 3 Output

Comparison of pretest and posttest resistance values in Systems No. 2 and No. 3 indicates an actual change in bridge resistor values while the bridge resistance values for System No. 1 remained the same throughout the test as expected. The difference between Bridge 1 and Bridges 2 and 3 is that Bridge 1 was built into the channel selector panel and potted, while Bridges 2 and 3 were unpotted and mounted on exposed terminal strips.

The cause of the drift of the bridge resistors cannot be ascertained from the available test data. The explanation presented by CD/TW (Reference 7) is possible, i.e., the measured resistances reflect true changes in resistance of the bridge resistors due to lowering of the temperature in the reactor control room. However, because the test data were obtained over a 30-hr period, a cyclic change would be expected in the data if the temperature control were the cause. In addition, the data indicate that the changes are permanent. Another possibility is that the resistor values drifted with aging during the repeated data cycling. Examination of the data in Figures 43 to 46 shows that the rate of drift is greater during the irradiation period from 8.0 to 14.0 hours than during the pretest and posttest period. However, this could be the result of the larger number of data cycles during the irradiation test, rather than during the pre- and posttest period.

3. Induced Voltages

At the conclusion of the data acquisition for each heating rate, the 20 vdc transducer power supply was disconnected from the input terminals of the active and dummy transducers. Voltage measurements were obtained for each output cable with no applied pressure or voltage. The data obtained were manually recorded and are presented in Table 14.

In the absence of an impressed voltage, no induced voltages would be expected. However, examination of the data in Table 14 indicates measured induced voltages of significant magnitudes, especially for the active

TABLE 14

"INDUCED" VOLTAGES FOR SIMULATED AND ACTIVE TRANSDUCER CABLES

Time (Elapsed)	Power (%)	Output (μv) S/N 47	S/N 50	S/N 61	S/N 63	Dummy 1	Dummy 2	Dummy 3
5.5	BKG	0	8	0	7		0	21
7.3	BKG	4	44	-5	8		0	43
8.3	1.36	-82	-94	-4	-12		0	3
8.8	1.98	-111	-121	9	-25	-21	0	8
9.5	3.62	-187	-164	19	-34	-39	0	32
10.1	5.83	-316	-429	59	-89	-41	0	28
10.8	7.3	-364	-544	96	-102	-101	0	18
11.4	9.4	-570	-568	74	-107	-60	-2	28
12.3	9.9	-522	-644	67	-114	-31	0	30
12.6	7.13	-323	-394	28	-66	-20	0	28
13.2	7.13	-490	-768	57	-126	-20	0	31
14.1	7.13	-700	-1208	78	-195	-31	-2	22
15.3	BKG	-	-129	7	-12	-10	-2	0
15.9	BKG	-10	-18	-6	0	0	-1	0
16.5	BKG	-19	-46	-6	0	-5	-	-
17.5	BKG	-62	-144	4	-10	-5	-1	-4
18.6	0	-97	-229	14	-22	-36	-2	-2

transducer output cables. These voltages are not proportional to the respective reactor power levels.

Figure 47 shows the induced voltage for the active transducers plotted against the elapsed test time. The polarity of transducer S/N 61 data is shown inverted for consistency with the other data. It will be shown later that the reversed polarity has significance. The resultant plotted data show a marked similarity to the transducer boss and hex-head temperature data presented in Figures 26 through 28. The similarity between the induced voltage curve and the recorded temperatures indicates that the observed voltages are apparently caused by thermal emf in the system and are not radiation induced.

In the description of the test transducers, it was noted that nickel cladding was used in each of the two 2-conductor cables for the purpose of identifying the positive lead. Laboratory temperature tests have shown that the use of nickel cladding generates a thermal emf that is consistent among cables from a given lot and proportional to the cladding thickness. Three manufacturers' cables were used in the construction of the transducers. They were: Scientific Engineering and Manufacturing Co. (SEMCO), Aero Research Inc. (ARI), and Continental Sensing Inc. (CSI). The thermal response curves determined from laboratory tests for each of the three lots of cables used are shown in Figure 48.

To correlate the data, it is necessary to know the temperature at the transducer end of the cable and at the opposite end of the cable (reference junction). During the test, temperature gradients existed between the internal header connections and the respective transducer monitoring thermocouples on the fixture. However, between test times 15 to 18.5 hr, the reactor was shutdown and all fixture temperatures were in equilibrium to within ±5°R. During this time period, all internal temperatures were also in equilibrium and were approximately the same as the monitored temperatures. The opposite or reference junction end of each cable was exposed to the

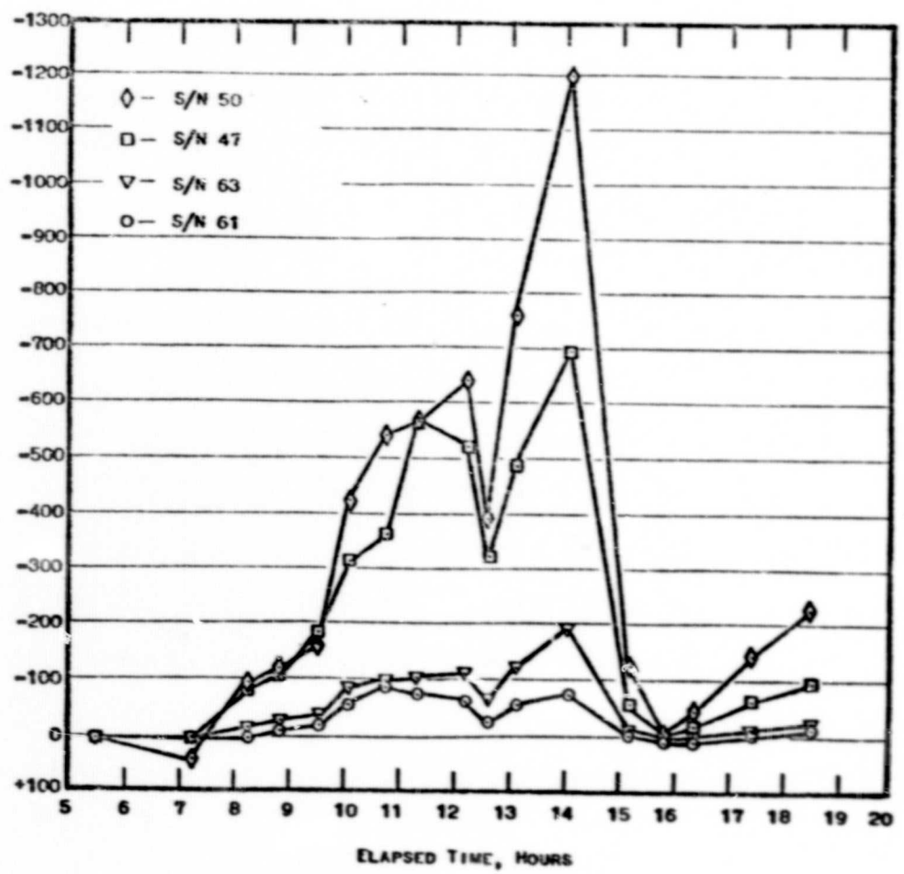

Figure 47 - Active Transducer Induced Voltages vs Time

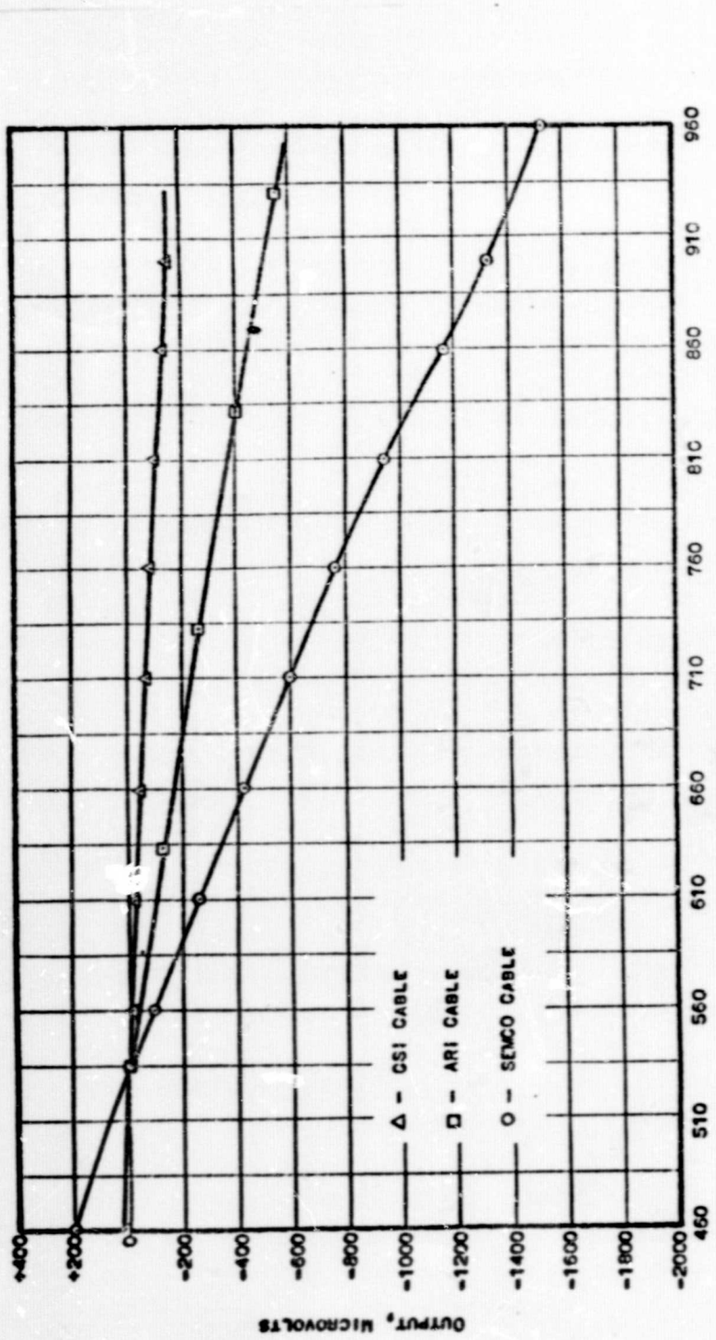

Figure 48 - Response Curve for Nickel Clad Copper vs Copper Conductors

atmospheric ambient temperature which varied throughout the test. At time 18.5 hr, the atmospheric ambient temperature was reported to be 70°F (535°R) which is approximately the reference temperature used during the laboratory tests. Table 15 shows the correlation between the observed voltages and the voltages calculated from the recorded transducer temperatures at time 18.5 hr and the thermal-response data.

It is apparent from the correlation that the induced voltages are thermal emf voltages generated by the nickel cladding on the positive conductor in the output cable. The results also infer that the thermal emf voltages were subtracted from all of the transducer outputs during the test. However, S/N 61 was manufactured with the output cable termination reversed in the transducer, i.e., the nickel-clad conductor indicated the negative output lead. This accounts for the reversed polarity of the observed voltages and also means that the thermal emf voltage was added to the transducer output during the test.

The induced voltage data for the simulated transducer systems are not as readily explained by the temperature correlation of the cables. As shown previously in Figure 2, the electrical termination for all metal sheathed cables is located in the external ambient atmospheric environment. With both ends of the cable at the same temperature, no thermal emf would be expected. However, the midsection of each cable passes through the radiation field and temperature gradients will exist along the conductors which can produce thermal emfs from the Thomson effect.

Since the voltages were monitored on each system output cable, the lack of System 2 voltage data is readily explained by referring to Figure 2 that shows the output cable totally in the control room. The data for Systems 1 and 3 shows no discernable pattern other than increasing and decreasing in amplitude when the reactor is brought to power and scrammed. Apparently the observed voltages are Thomson effect thermal emfs, but because of the combined effects of the radiation field and the cryogenic cooling of the fixture, no quantitative analysis is possible.

TABLE 15

COMPARISON OF OBSERVED AND DETERMINED VOLTAGES AT TIME 18.5 HR

Transducer	Temperature °F	Calculated Thermal emf Voltage (μv)	Observed Voltage (μv)	Response Curve
S/N 47	609	-98	-97	ARI
S/N 50	601	-225	-229	SEMCO
S/N 61	608	-20	-14	CSI
S/N 63	609	-20	-22	CSI

4. Spurious Signals

The acquisition of the induced voltage data was performed by the automated Dymec. This system also measured the active and dummy transducer input and output bridge resistances. The bridge measurements obtained during the zero-voltage cycle differed significantly from those measurements obtained during a normal pressure-calibration cycle. Figure 49, showing the input bridge resistance data for simulated System No. 3, is typical for all of the input and output bridge resistance measurements obtained. The data spikes occurring throughout the data coincide with the zero-voltage data cycles.

The observed data abnormalities appear to be examples of the previously described effect of cables accumulating an electron charge in the absence of an impressed voltage. The spikes are conspicuously missing during the preirradiation test period and only occur during the irradiation and post-irradiation period. The magnitudes of the spikes vary considerably and appear to be dependent upon the gamma rate and the elapsed time between removing the 20 vdc power and making the measurement. It was also observed that whenever two data cycles were obtained in rapid succession, the magnitude of the second data spike was significantly reduced. The charging and discharging of the transducer system appear to require several seconds to stabilize. The automated data system samples each channel for 1 sec and requires approximately 45 sec to sample 41 channels. The same effect was not observed during the insulation resistance measurements, since the data acquisition was manually performed and time was allowed for the instruments to stabilize before recording the measured value.

Care should be taken when using automated data acquisition systems. For measurements in a radiation environment the power-supply voltage must be maintained while sampling the output data or sufficient data sampling time allowed to stabilize the excess charge on the instrument system.

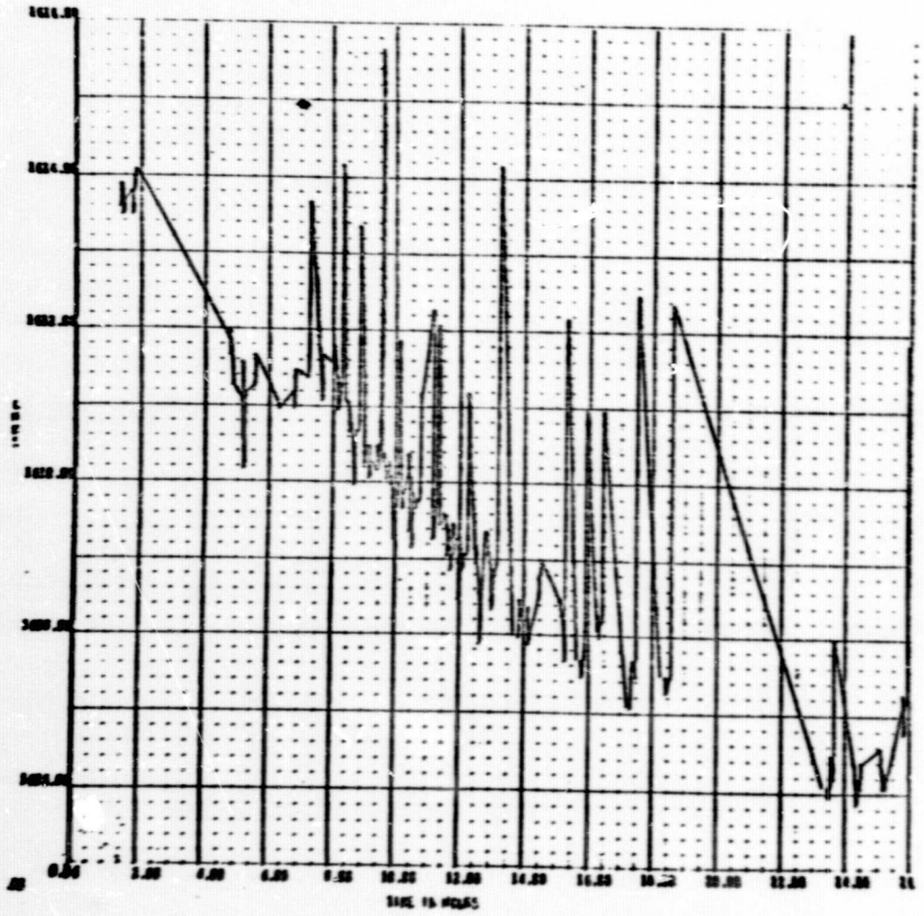

Figure 49 – Bridge Input Resistance, System 3

5. Conductor Orientation

One of the secondary objectives of the test was to determine the significance of various conductor polarity orientations on the overall system performance. To accomplish this purpose, three simulated systems with various combinations of cables in the radiation environment were included in the test fixture as shown in Figure 2. System 1, that had both the input and output cables exposed to the radiation environment, also included a reversing circuit that transposed the positive output conductor into the cable that contained the positive input conductor.

The expected radiation effect for cables in a radiation field is a decrease of insulation resistance caused by the effects of gamma radiation. The loss of insulation resistance in a transducer circuit will cause shunting of the bridge with output errors resulting. In the normal system, the shunting resistance is in parallel with the bridge input and output resistance resulting in a decrease in input voltage and an attenuation of the output signal. However, pretest analysis indicates that the output error, attributed to shunting of the input to the bridge, is a negligible factor because of the relatively low resistance values of the power supply internal impedance and bridge input resistance; compared to the shunting resistance. Shunting of the bridge output will cause a significant error when shunt resistance is below 10^7 ohms because of the increase in bridge output current and corresponding decrease in output voltage.

In the reversed system, the shunting resistances are parallel across opposite arms of the bridge creating an unbalance that appears as an output signal. The pretest analysis indicates that significant output errors occurred with shunting resistances below 10^9 ohms.

The simulated output data for the three systems are shown in Figures 50, 51 and 52. The output data for System 1, normal and reversed conditions, show a variation during the test that resembles the profile of

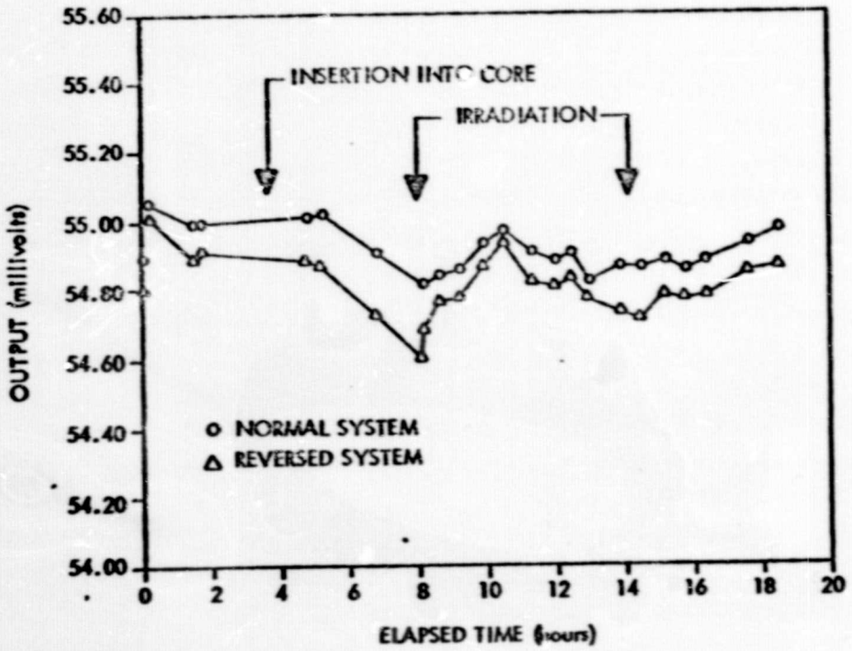

Figure 50 – Output, Simulated System 1

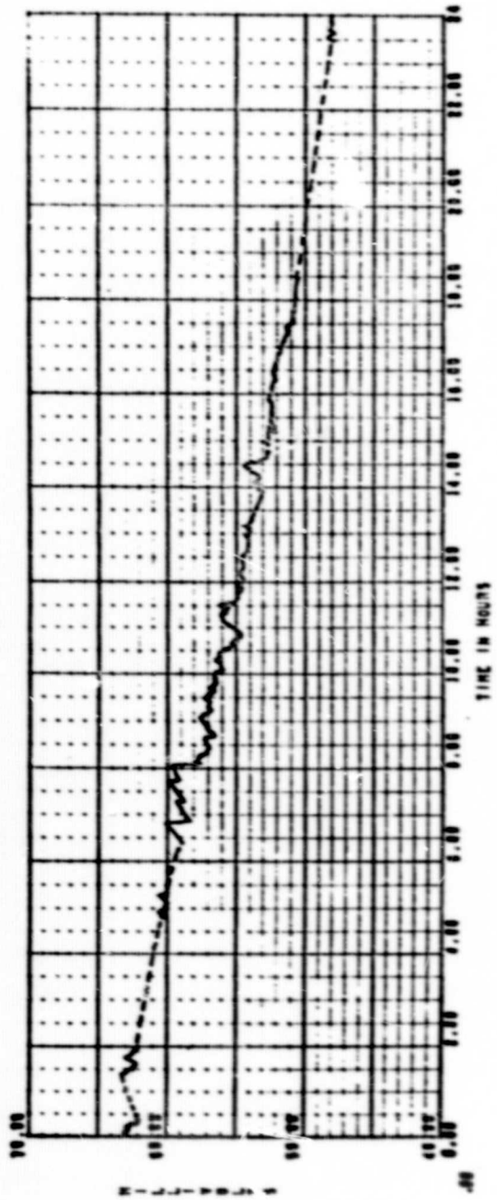

Figure 51 – Output, Simulated System 2

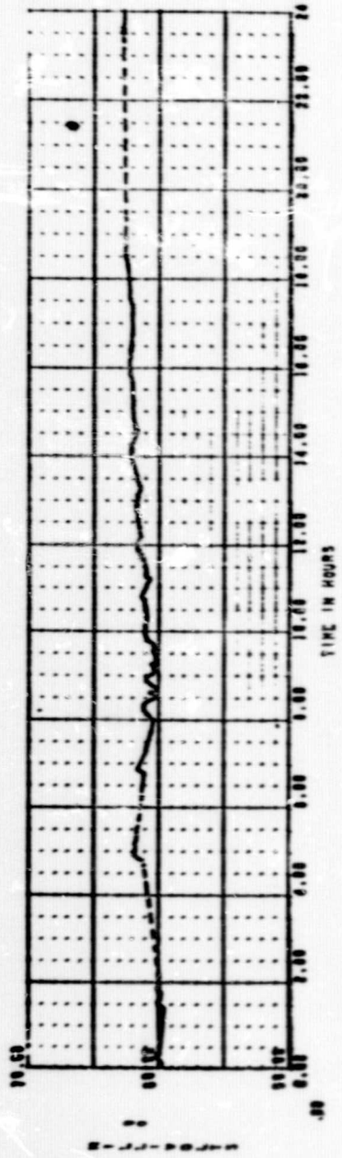

Figure 52 - Output, Simulated System 3

the simulated insulation resistance data shown previously in Figure 42. By comparison, it is apparent that the insulation shunting resistance does affect the output of the normal system and that the reversed system is more sensitive to the variations in the insulation resistance.

Pretest predictions, and the data obtained from the simulated system output and cable insulation resistance values during the test, are shown in Figure 53. The data for the reversed system agree with the pretest analysis. However, the data for the normal system decrease more rapidly than predicted. The difference may be attributed to a simplification assumed in the analysis. In the analysis it was assumed that the effects of leakage currents to ground and unsymmetrical shunting of the bridge through the ground were negligible. The data indicate that this assumption was not valid.

The output data for simulated Systems 2 and 3 show decreasing and increasing trends respectively throughout the test. These trends appear to be the result of unbalance caused by the individual bridge resistors changing by different amounts. Because of the drift of the bridge resistors, any radiation effects present in the data would be difficult to assess. As a result, no useful information regarding the radiation effects on the input and output cables independently can be extracted from the test data.

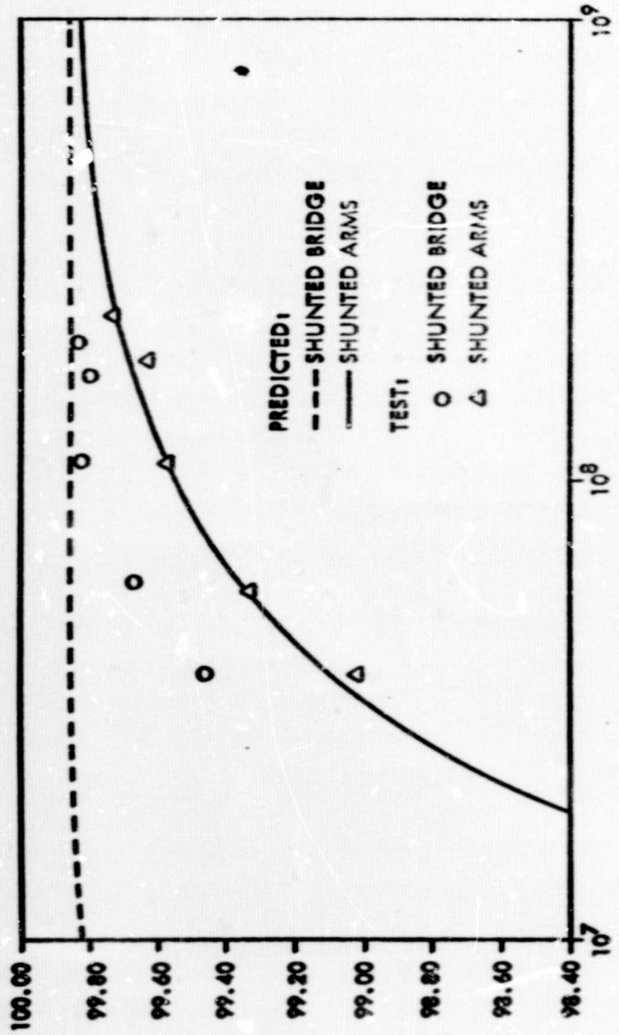

Figure 53 - Bridge Output vs Shunting Resistance

D. ACTIVE TRANSDUCERS

The overall performance of the active transducer systems was determined by calibrating the transducers throughout the test with a known pressure reference and monitoring the output. The data obtained are presented in Figures 54 to 58 for S/N 47, 50, 61, and 63. Each figure shows the transducer output for the pressure calibration steps of 0, 250, 500, and 750 psig. Each transducer exhibited moderate to severe changes in output during the test and all exhibit a permanent decrease in output at the end of the test. In terms of total error band, the output deviations for the transducers are:

S/N 47	$\frac{+9.0}{-6.9}$	% full-scale output
S/N 50	$\frac{+3.3}{-16.5}$	% full-scale output
S/N 61	$\frac{+1.0}{-2.6}$	% full-scale output
S/N 63	$\frac{+1.5}{-1.9}$	% full-scale output

While the total error band is indicative of the transducer uncertainty in the radiation temperature environment, it does little to define the effect of radiation on the transducer sensing element. A better understanding of transducer performance can be obtained by determining the effects of the radiation environment of the individual transducer characteristics such as bridge resistance, insulation resistance, linearity, sensitivity, and zero-point stability.

1. Insulation Resistance

The active transducer insulation resistance data, tabulated previously in Table 11, are shown plotted in Figure 58. These data exhibit the same characteristics during the pre and posttest periods as the simulated

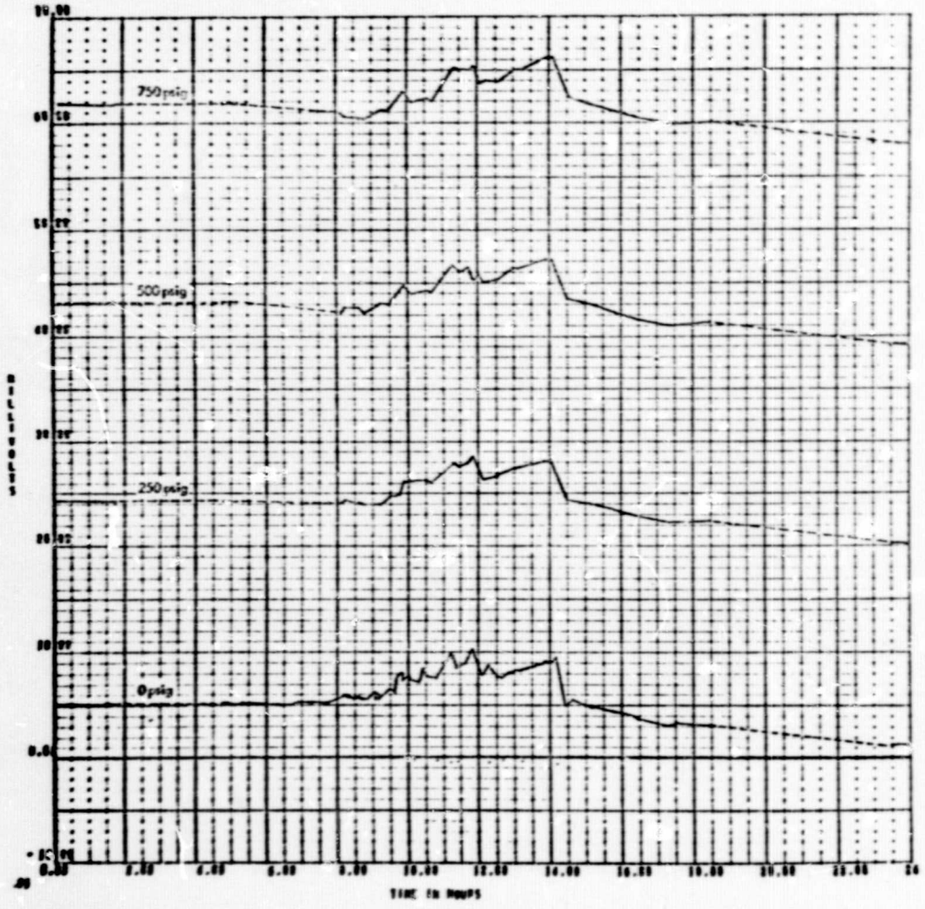

Figure 54 - Output, Transducer S/N 47

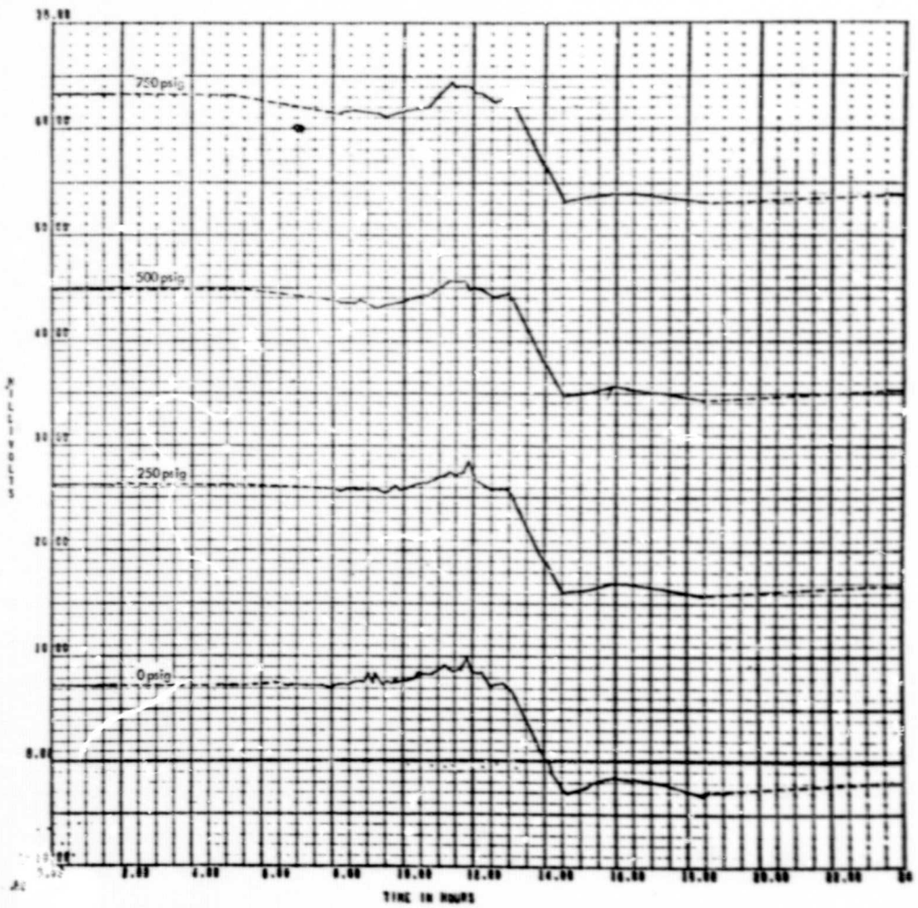

Figure 55 - Output, Transducer S/N 50

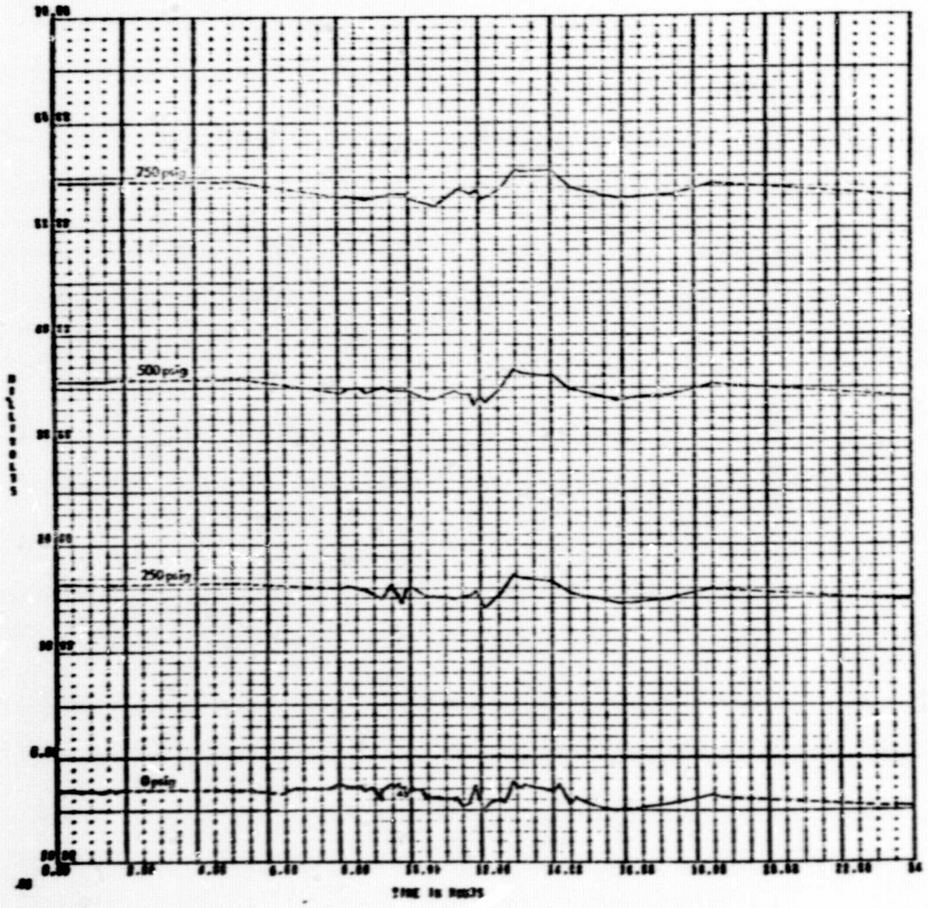

Figure 56 - Output, Transducer S/N 61

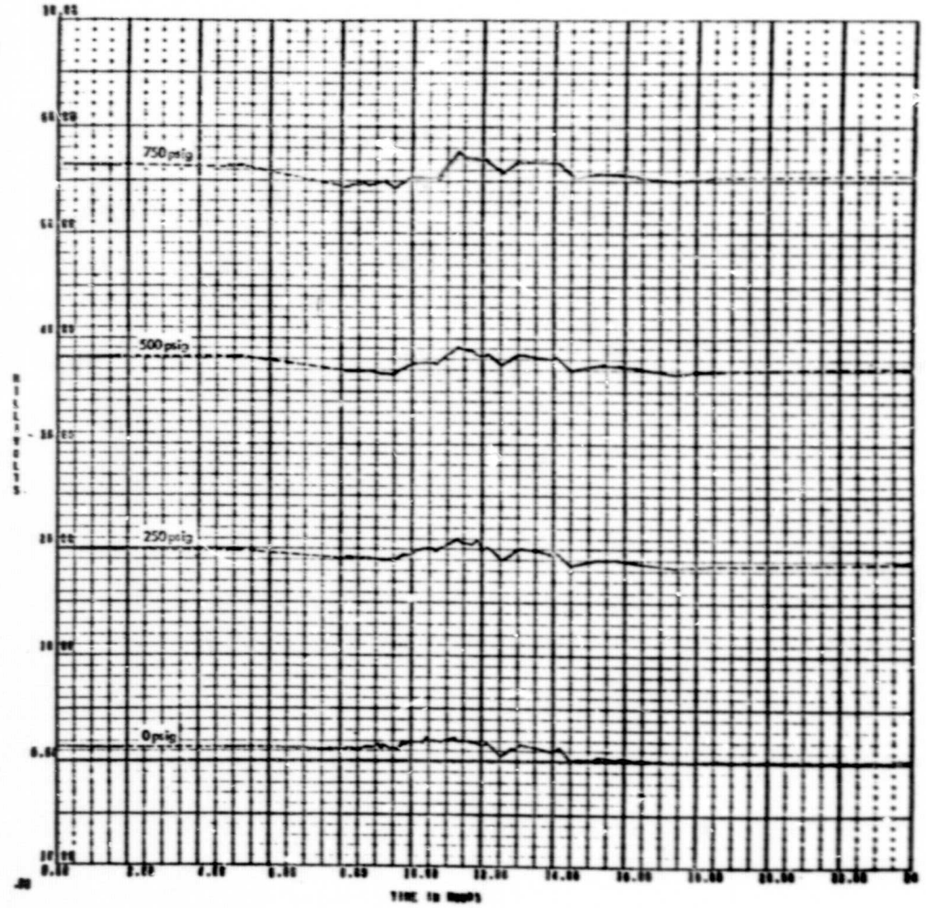

Figure 57 - Output, Transducer S/N 63

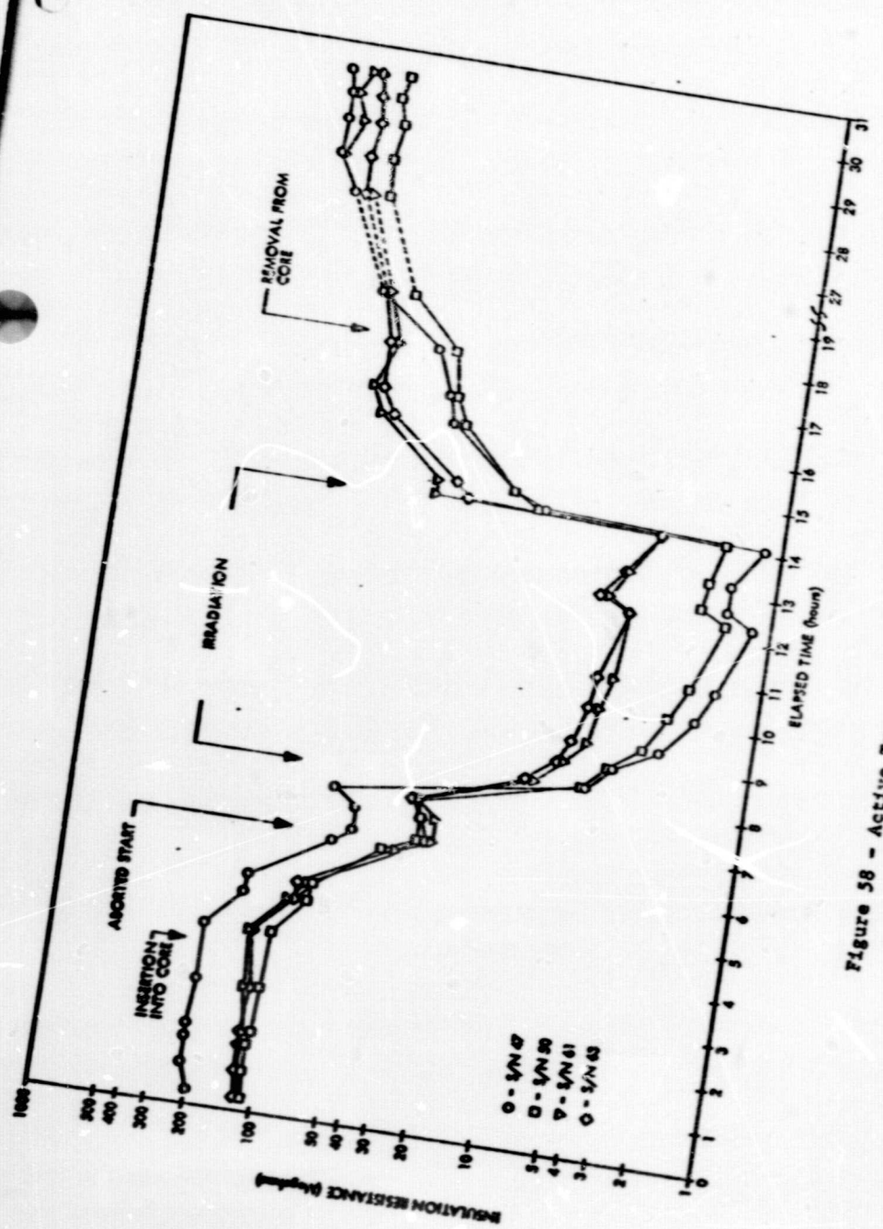

Figure 58 - Active Transducer Insulation Resistance

transducer-cable insulation resistance data presented in Figure 42. However, during the irradiation period, the insulation resistance of the active transducers continues to decrease with increasing radiation levels as expected. The most significant feature seen in the data is the similarity of insulation resistance values of transducer S/Ns 47-50 and 61-63.

In the analysis of the simulated transducer cable insulation resistance data, the data was found to be influenced by the cryogenic cooling of the fixture with the result that insulation resistances were in excess of 20 megohms throughout the test. Since the active transducer cables were also physically attached to the coolant manifold, similar masking of the radiation effects on the active transducer cables would also be expected. As a result, the observed values very nearly represent the insulation resistance of only the transducers. Since it is known that the two groups of transducers were manufactured in different lots, the data indicate that a variation in the deposition of ceramic substrate and strain-gage material may be responsible for the observed difference. This would imply that by control of the manufacturing process, an improvement in the insulation resistance at high gamma rates could be realized.

The negligible effect of the cable insulation resistance observed during the test may not be the case where a portion of the cable is exposed to higher temperatures, or gamma levels, than experienced by the transducer.

2. Bridge Resistance

Input and output bridge resistance data obtained during the test for the active transducers exhibited data spikes similar to those observed in the simulated transducer data. In addition, resistance changes were observed in the data that corresponded to the various pressurization cycles. To illustrate the trend of the resistance data during the test, the data were thinned

to include only those data corresponding to the zero-pressure cycles and normalized to show changes during the test as a percentage of the pretest resistance values. The resultant data are shown in Figures 59 through 66 for the input and output resistance deviations of transducer S/Ns 47, 50, 61, and 63.

The data show that the bridge input and output resistances increased permanently as a result of the irradiation. All resistance measurements exhibit fluctuations due to temperature effects during the test except for S/N 61 input resistance, which appears to be invalid because of the presence of spikes throughout the data. The spikes are similar to those observed during the zero-voltage calibration cycles and it is suspected that an intermittent contact in the channel selector stepping switch is the cause of the anomaly. No other data obtained from S/N 61 exhibits similar occurrences.

The net observed changes for the input and output resistances are tabulated in Table 16.

TABLE 16

INPUT-OUTPUT BRIDGE RESISTANCES NET CHANGE - PERCENT OF PRETEST

S/N	Input	Output
47	0.39	0.39
50	0.38	0.37
61	--	0.14
63	0.21	0.19

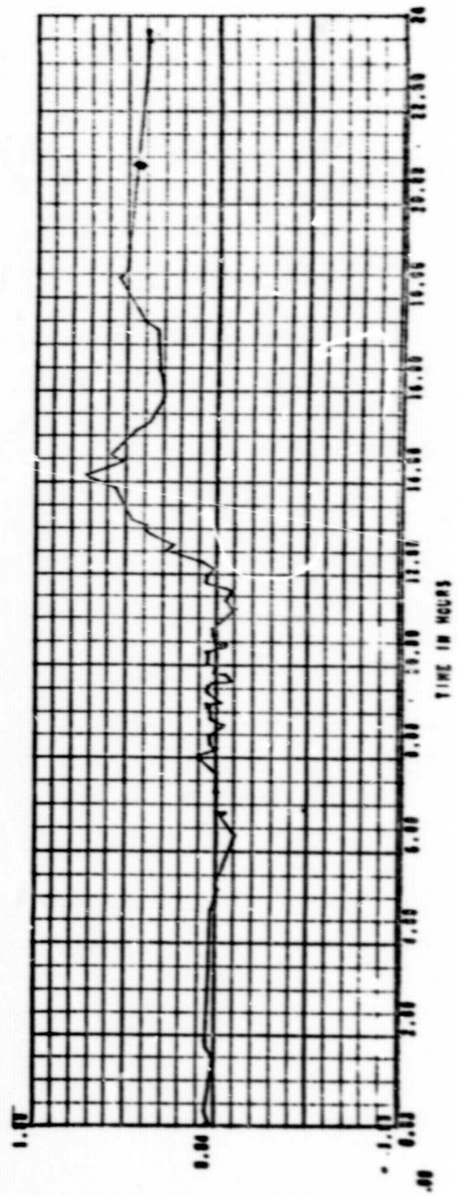

Figure 59 - Resistance Deviation - Bridge Input S/N 47

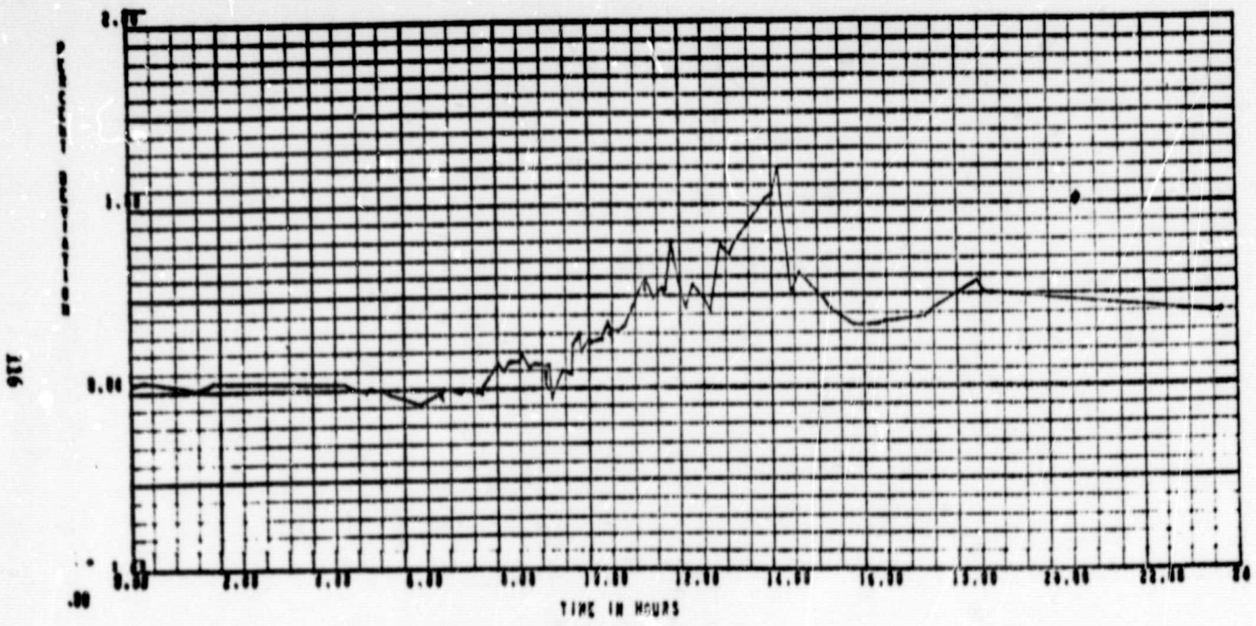

Figure 60 - Resistance Deviation - Bridge Output S/N 47

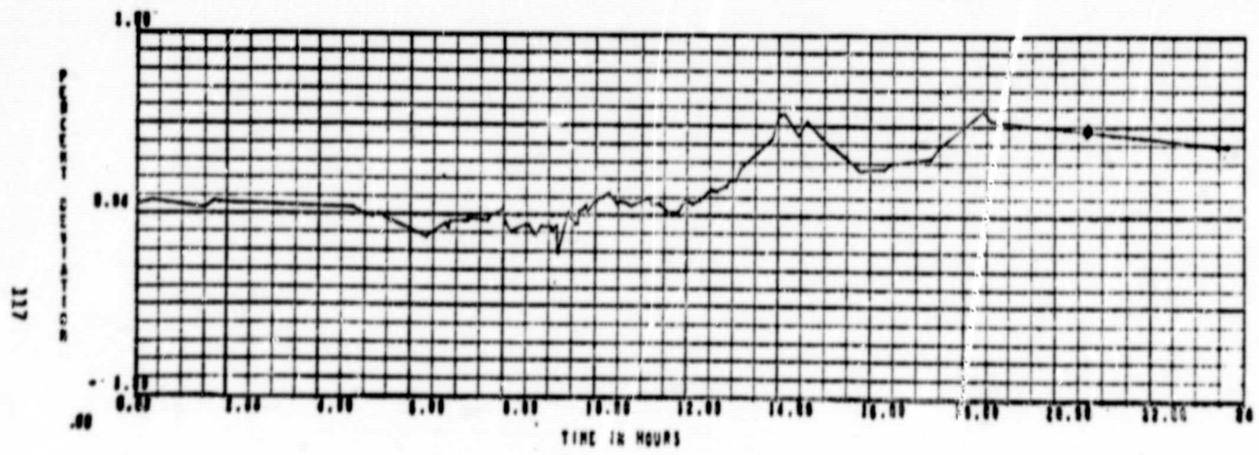

Figure 61 - Resistance Deviation - Bridge Input S/N 50

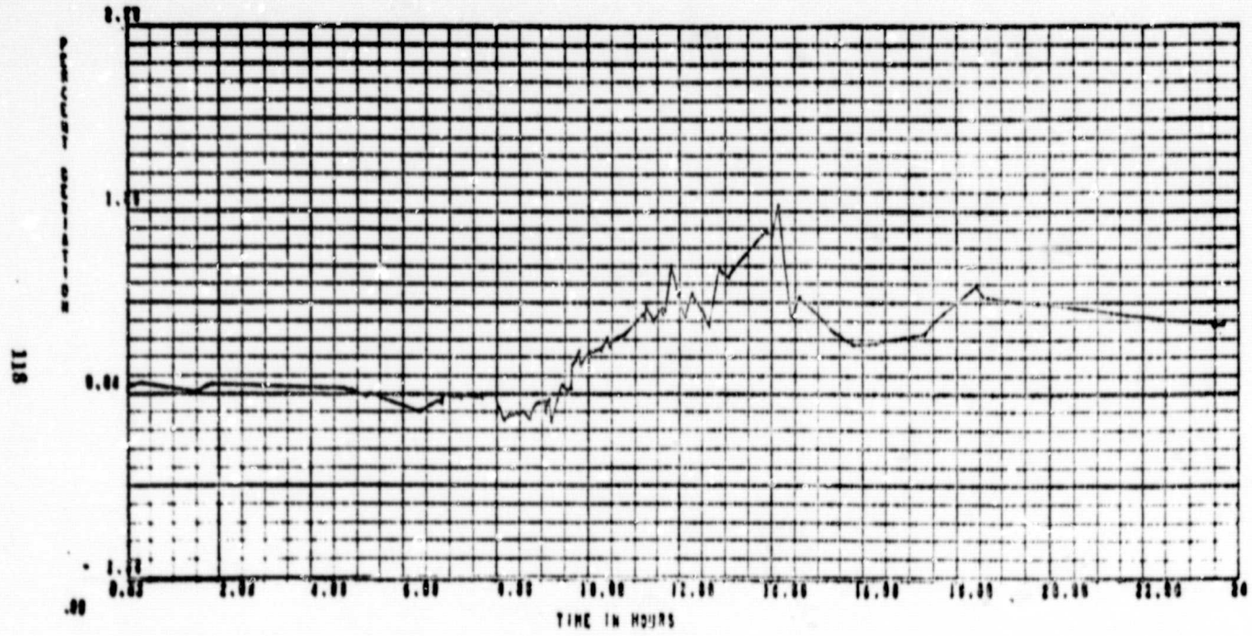

Figure 62 - Resistance Deviation - Bridge Output S/N 50

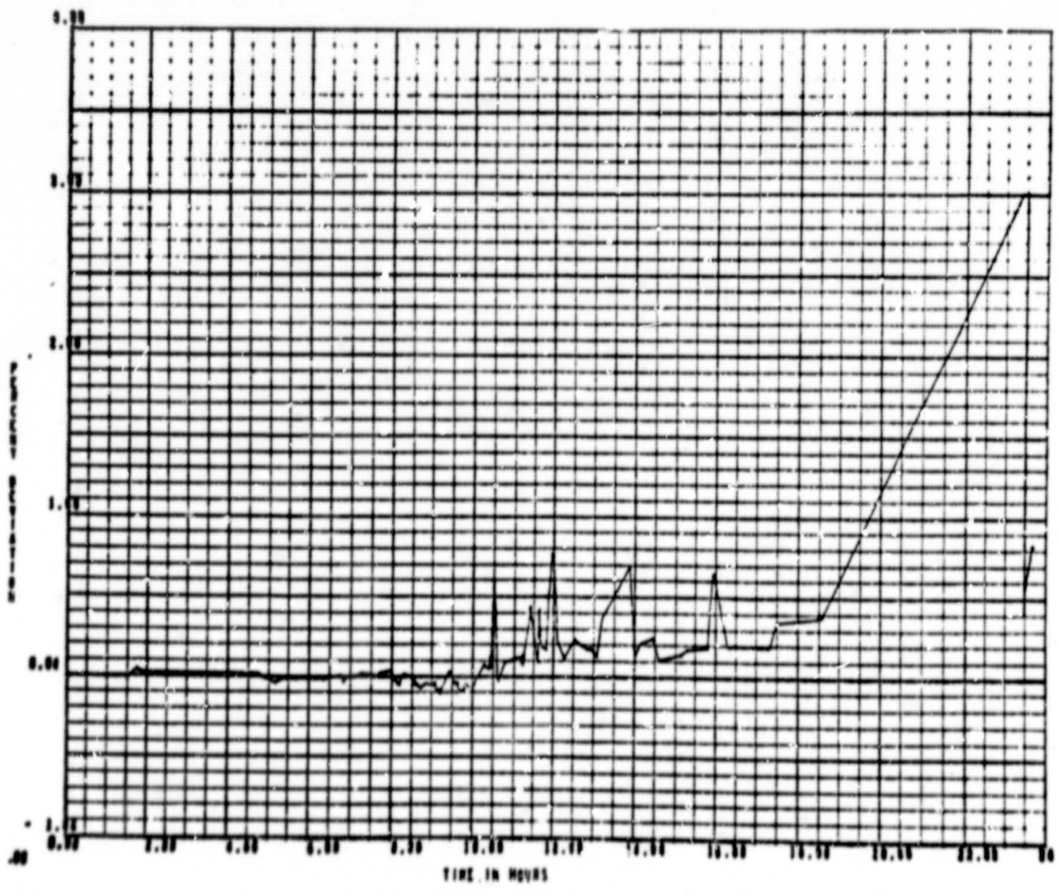

Figure 63 - Resistance Deviation - Bridge Input S/N 61

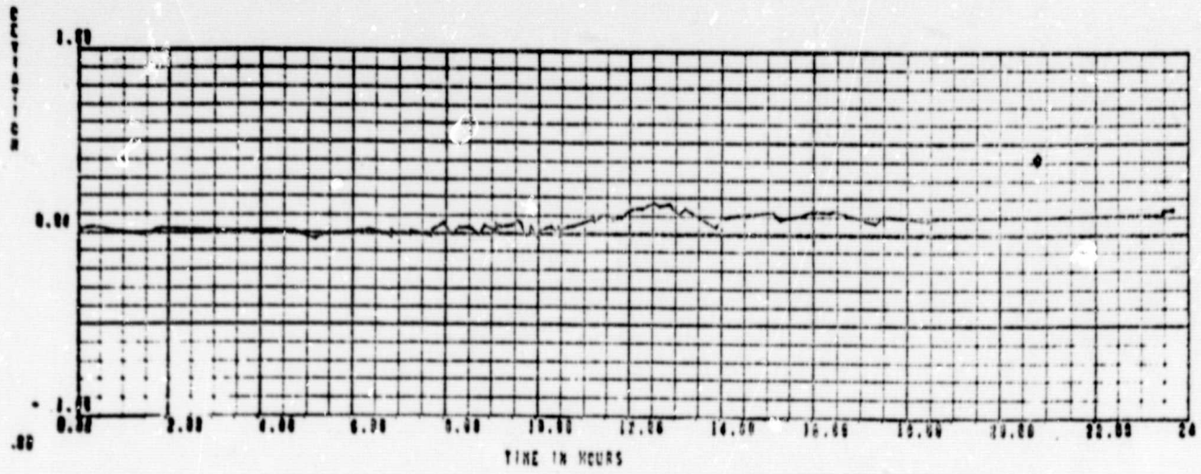

120

Figure 64 - Resistance Deviation - Bridge Ouptut S/N 61

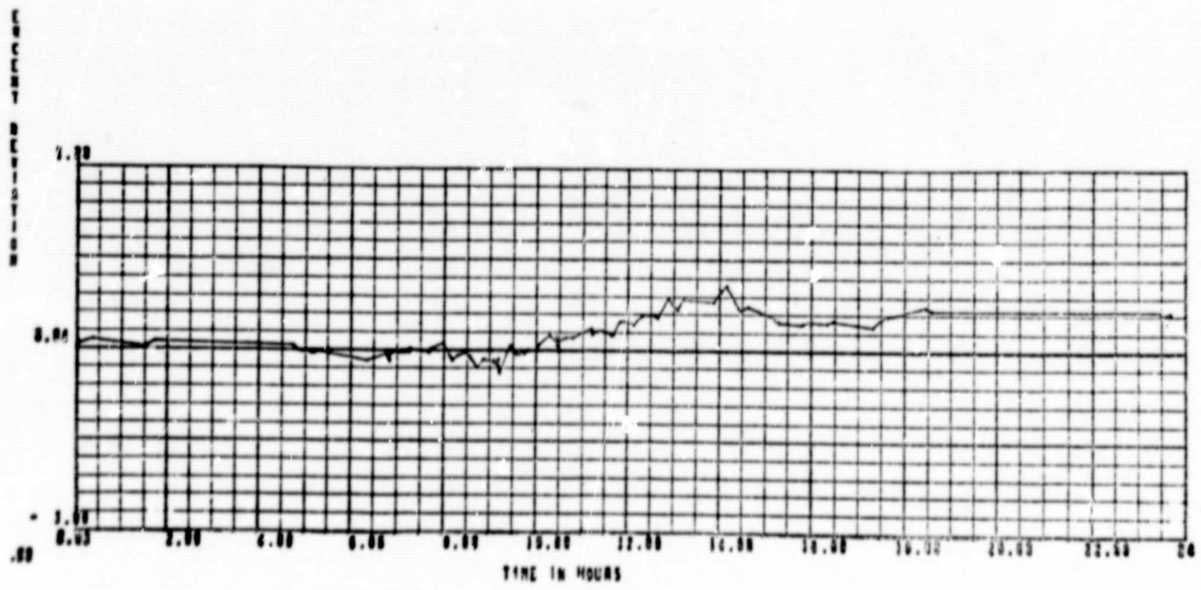

121

Figure 65 - Resistance Deviation - Bridge Input S/N 63

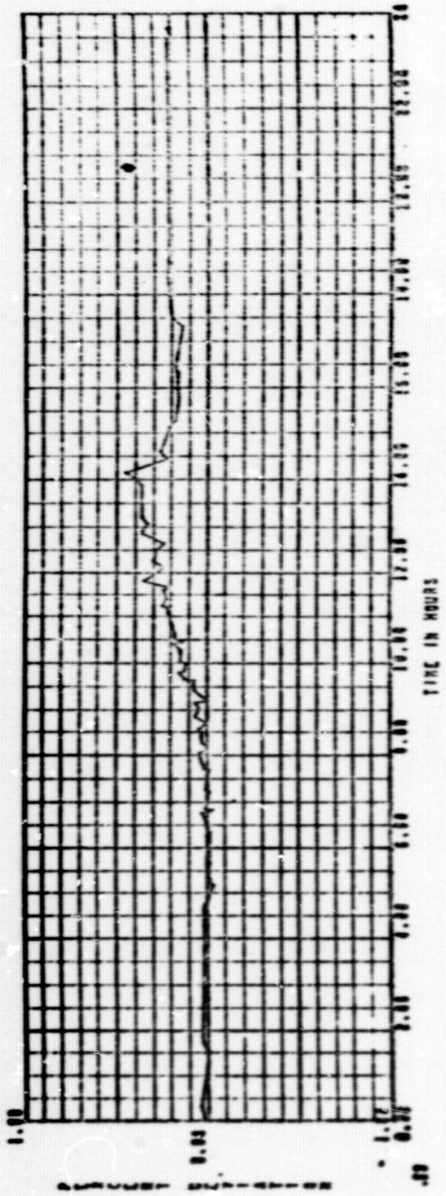

Figure 66 - Resistance Deviation - Bridge Output S/N 63

Temperature variations in the bridge resistances are expected and, as noted, all resistances reflect this effect. However, comparison of the input and output resistances of respective transducers indicates a divergence between the two during the irradiation period. In each case the input resistance deviations resemble the boss-temperature profiles showing the two phases of temperature control, i.e., constant temperature and increasing temperature. The output resistance deviations more closely resemble the hex-head temperature profiles. The similarity to the temperature profiles indicates a possible dependency upon the internal-temperature gradients.

Investigating this possibility, the difference between the input and output deviations were determined. The resultant data are shown in Figures 67, 68, and 69 for S/Ns 47, 50, and 63. Comparing the difference profiles and the diaphragm temperature gradients shown in Figure 70, shows a marked similarity that substantiates this possibility.

The mechanism causing the divergence is difficult to determine. The magnitude of divergence appears to be related to the temperature coefficient of resistance (TCR) of the bridge material, since it is minimal in S/N 63 that has a very low TCR (0.0006% F.S./°R), and greater for S/Ns 47 and 50 that have TCRs of 0.0024 and 0.0016% F.S./°R respectively. Attempts to synthesize the bridge-resistance divergence by correlating the observed temperature gradients, and the known transducer TCRs were unproductive. In the sensing element configuration used, the two tension arms of the bridge are located near the center of the diaphragm that, from the data, was approximately 20°R warmer than the two arms located on the diaphragm periphery. However, since the two tension arms are located in opposite arms of the bridge, changes in resistance are balanced in the bridge and, theoretically, the bridge input and output resistances would increase by equal amounts. The overall transducer TCR is the summation of the TCR's of the individual legs of the bridge. It is possible that the TCR's of the individual legs are significantly different from each other so that in the presence of gradients, the changes in resistance are unequal, resulting in the divergence of the measured input and output resistance values.

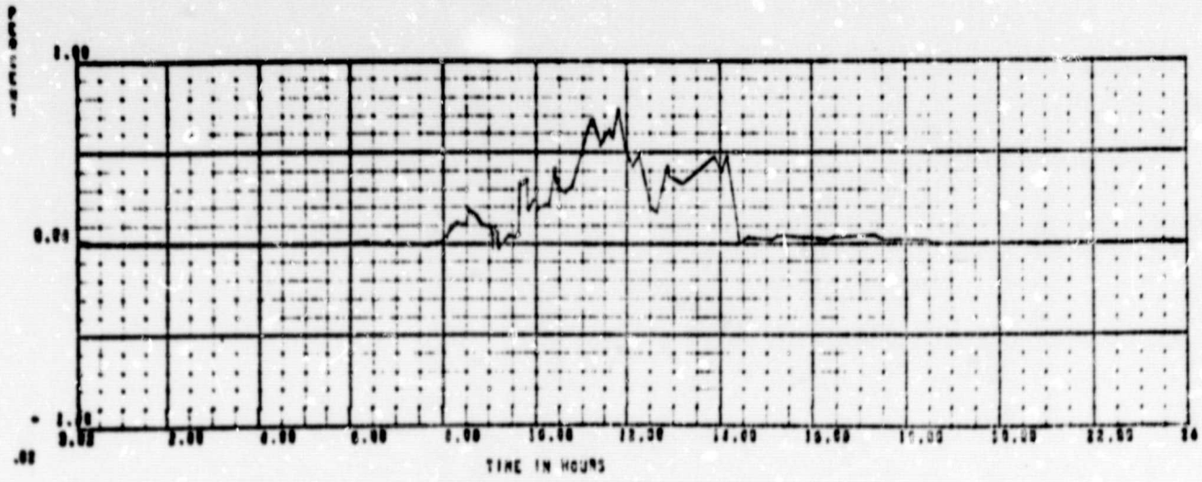

Figure 67 - Deviation - Bridge Input vs Output, S/N 47

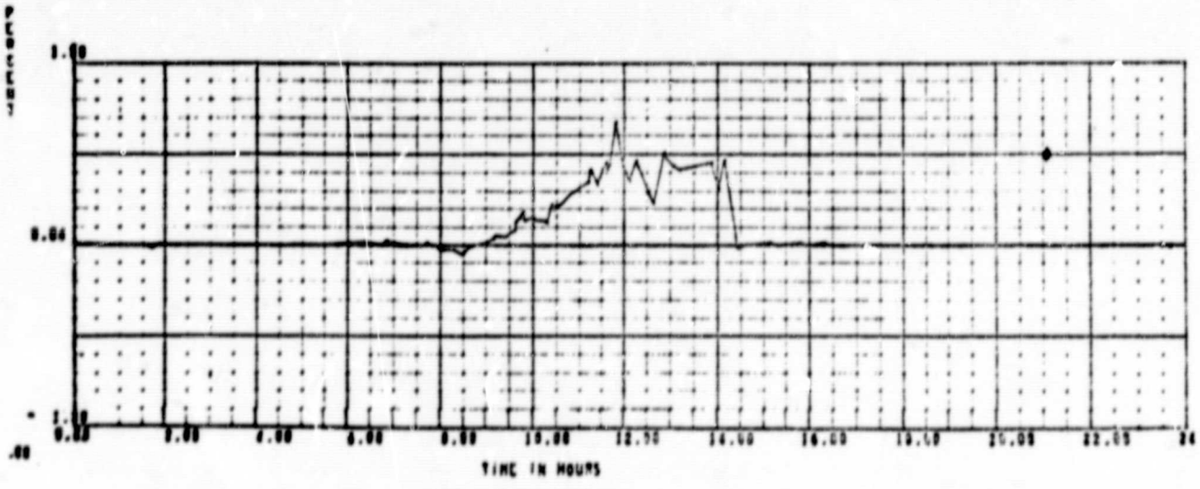

Figure 68 - Deviation - Bridge Input vs Output, S/N 50

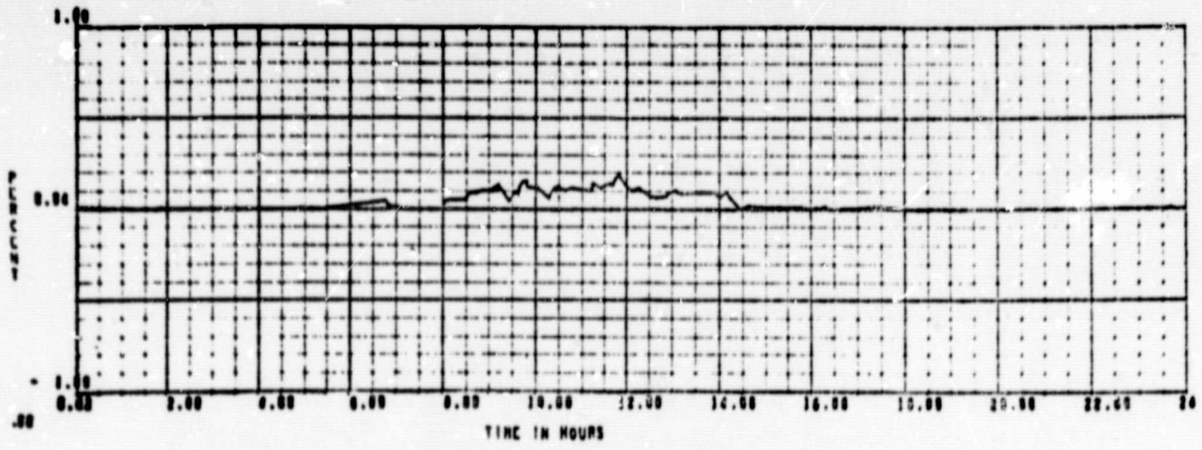

Figure 69 - Deviation - Bridge Input vs Output, S/N 63

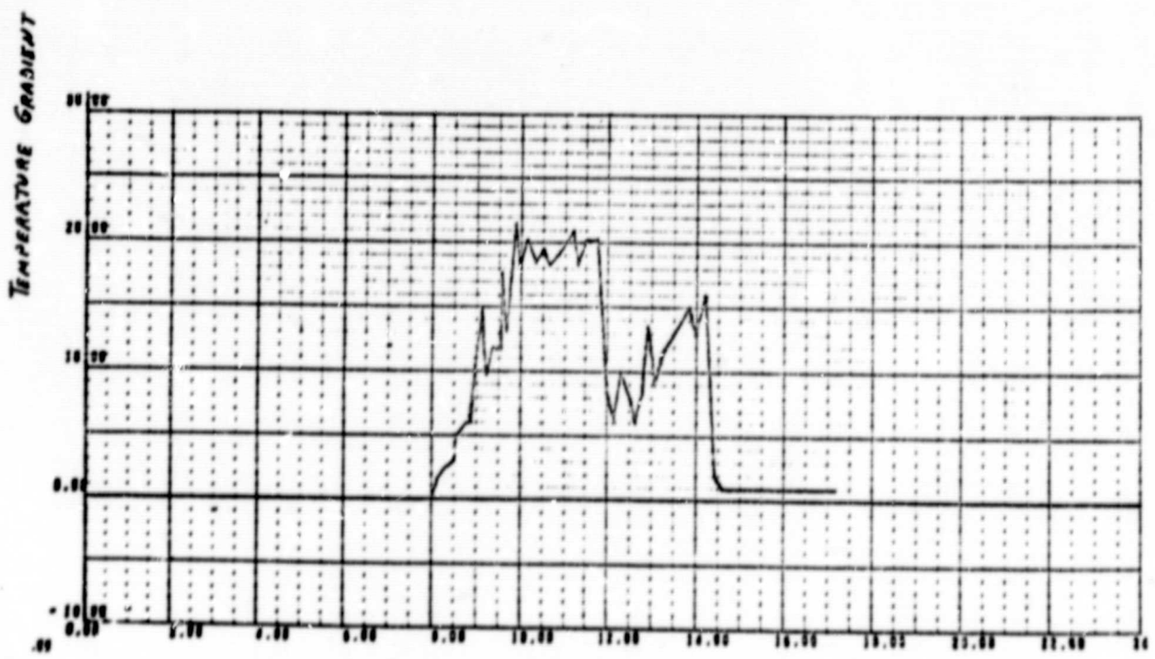

Figure 70 - Diaphragm Gradient - Instrumented Transducer

3. Nonlinearity

In a transducer, nonlinearity is defined as the difference between the actual instrument output and the expected output as defined by a straight-line reference between the zero and full-scale values and is presented in terms of a given percentage of the instrument full-scale output. The output data for the active transducers were reduced to nonlinearity data for the 250- and 500-psig calibration cycles, and are plotted in Figures 71 through 74 for transducers S/Ns 47, 50, 61, and 63 respectively.

Comparison of curves for the four transducers includes a uniformity in characteristics throughout the test. All transducers exhibit erratic values during the irradiation period with relatively stable values during the pre and posttest periods. Temperature effects are evident during the posttest data cycles immediately following the test when all fixture temperatures were in equilibrium. The period of erratic data is attributed to the fluctuations of the fixture temperature during the test. Although the data are erratic, an overall downward trend can be seen.

Comparison of the pre and posttest nonlinearity values for the four transducers indicates that a significant improvement in transducer linearity resulted from the irradiation of the sensing element. The percent change from pretest values for:

S/N 47	-38.3%
S/N 50	-22.5%
S/N 61	-21.7%
S/N 63	-21.6%

An interesting feature in the data is the apparent continuing improvement in linearity during the posttest calibration cycles after 23.0 hr. The decreasing

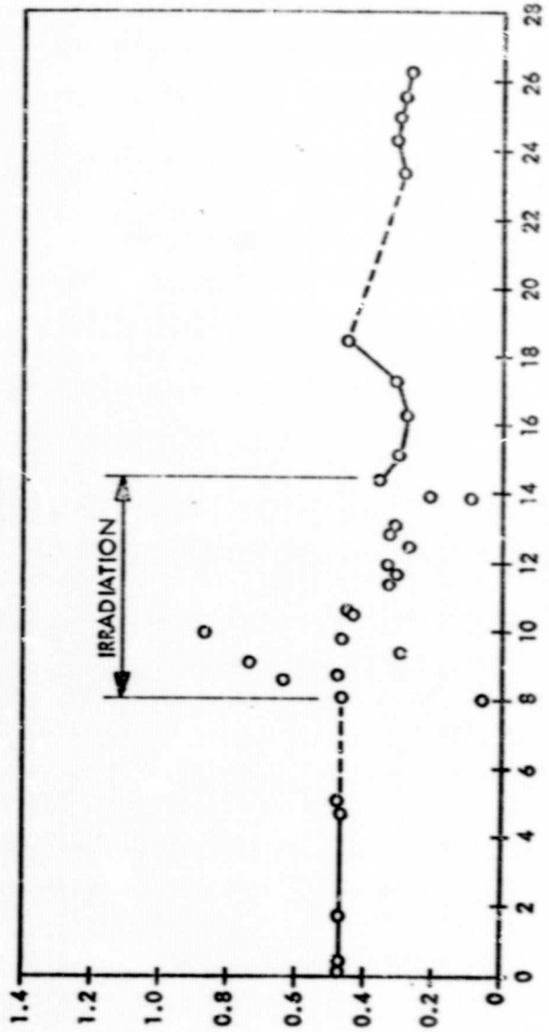

Figure 71 - Nonlinearity vs Time, S/N 47

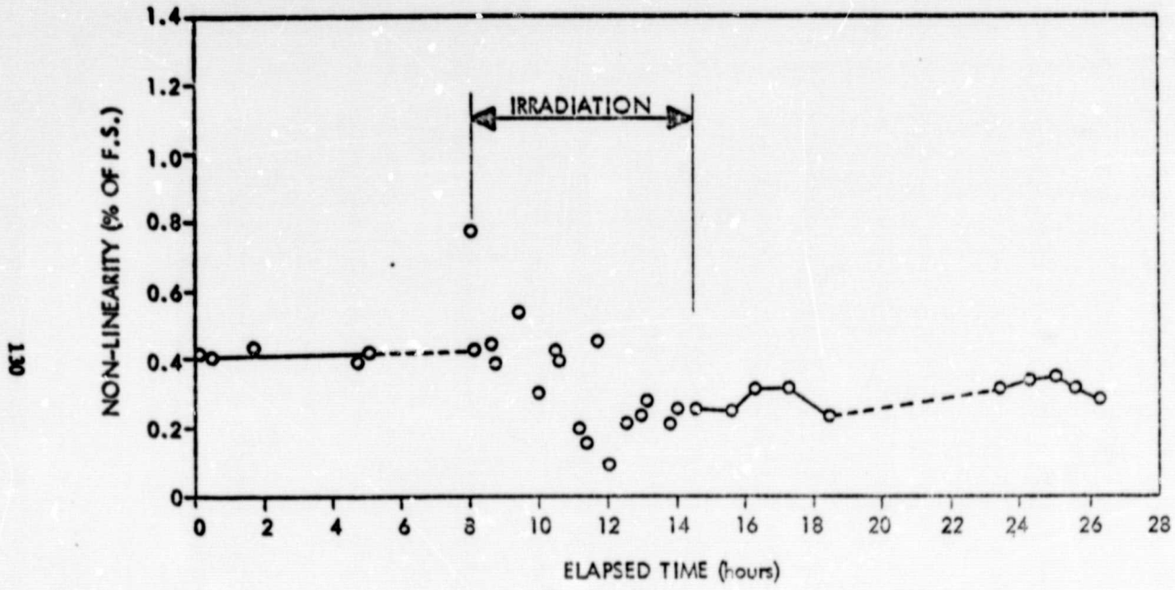

Figure 72 - Nonlinearity vs Time, S/.. 50

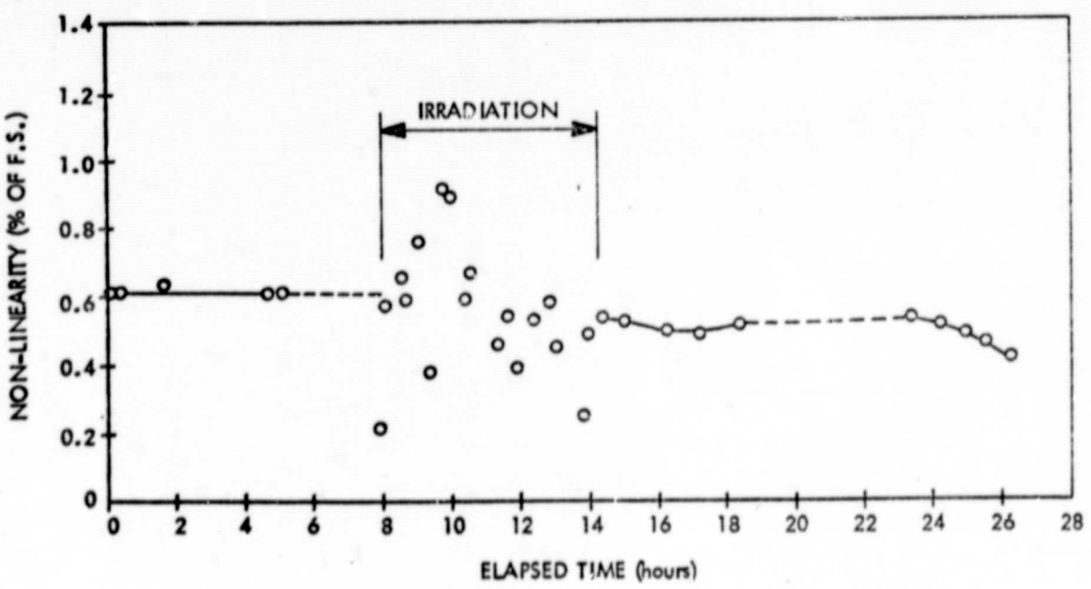

Figure 73 - Nonlinearity vs Time, S/N 61

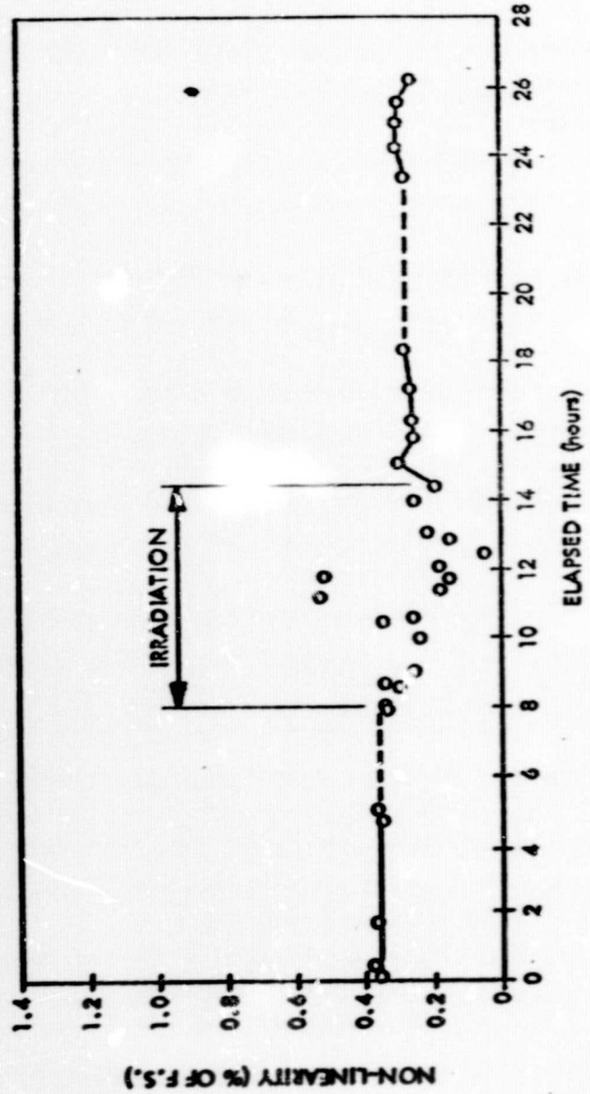

Figure 74 - Nonlinearity vs Time, S/N 63

trend exhibited by all transducers appears to be a function of the pressure cycling but may also be related to the residual activity in the strain material, and possible transmutation of elements since the improvement during the test is apparently the result of material changes in the bridge elements.

4. Sensitivity

The effect of nuclear radiation on the sensitivity of each transducer was investigated by calculating the sensitivity values of each transducer for each full-range pressurization cycle. The resultant reduced data are shown plotted in Figures 75, 76, 77, and 78 for transducers S/Ns 47, 50, 61, and 63. The sensitivity data curves are characterized by a decrease in transducer sensitivities, at the start of the irradiation period, to a relatively constant value of -3.0% of full scale. An apparent recovery occurs for all transducers, to near pretest values, between time 10.6 and 11.2 hr. During the posttest period, from time 27.5 to 27.3 hr, the sensitivity values are constant and except for S/N 50, are all slightly greater than the pretest values. The change between pre and posttest sensitivities for the four transducers is:

S/N 47	+ 0.28% FS
S/N 50	0
S/N 61	+ 0.36% FS
S/N 63	+ 0.60 FS

The observed sensitivity changes at the start of the irradiation period appear to be radiation-induced transient effects. However, the subsequent apparent recovery of the sensitivities during the test, instead of at the end of the test as expected, raises the question of whether the observed change is radiation induced or caused by external factors. From available test data, known factors that could affect sensitivity were investigated and found to be insignificant or shown to be uncorrelatable. Figure 79 presents the average deviation of the four transducers along with a typical mounting-boss temperature

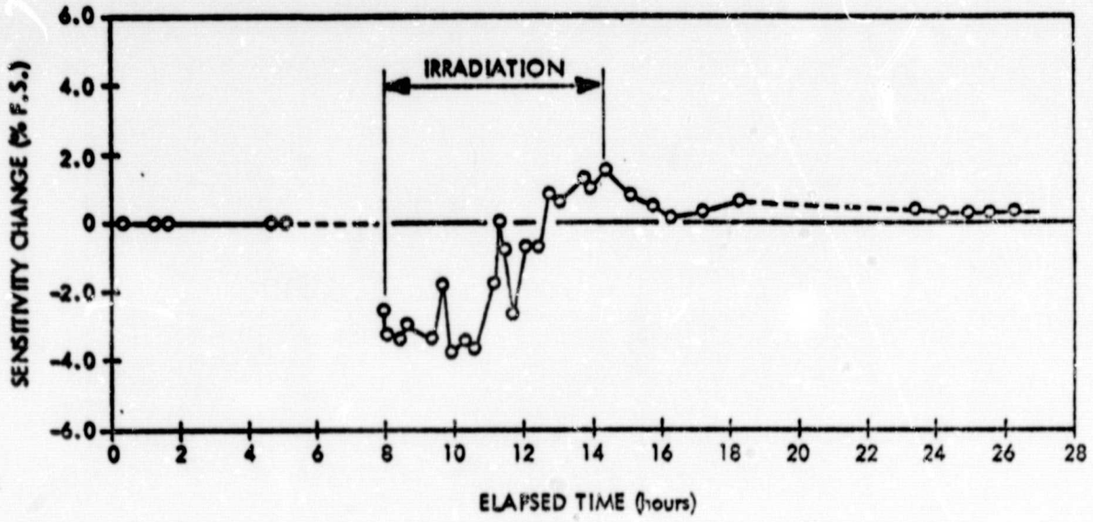

Figure 75 - Sensitivity vs Time, S/N 47

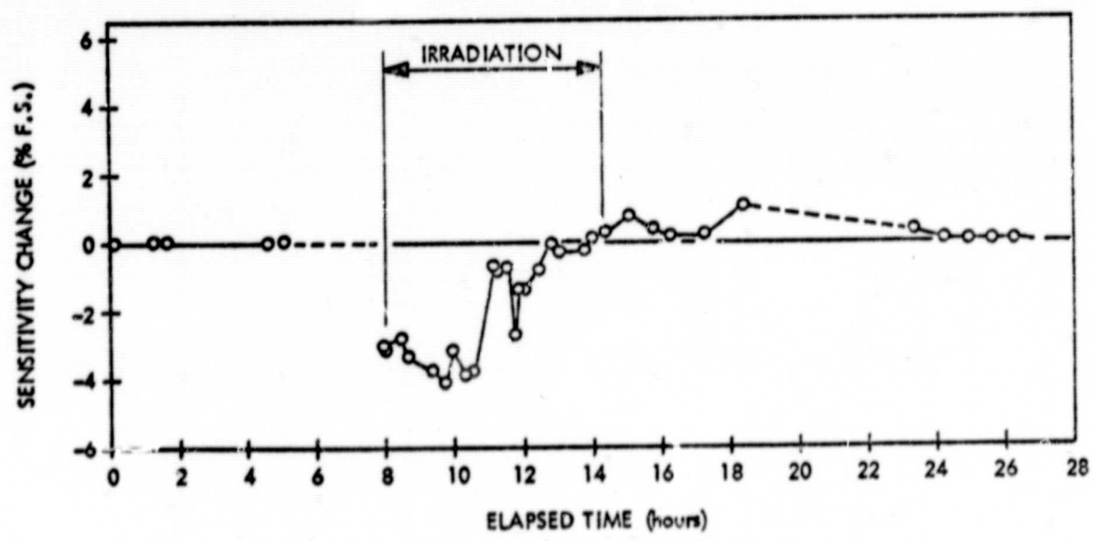

Figure 76 - Sensitivity vs Time, S/N 50

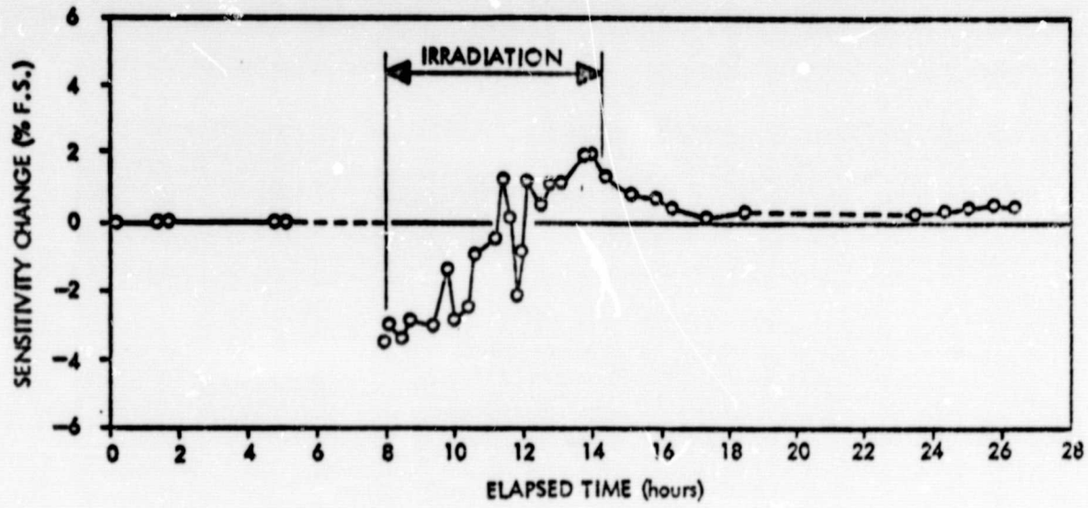

Figure 77 - Sensitivity vs Time, S/N 61

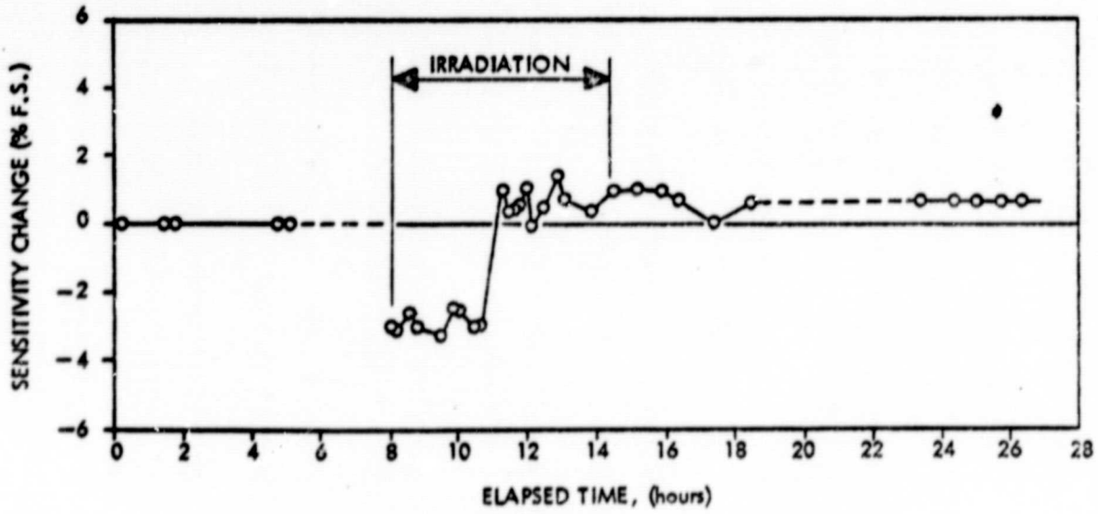

Figure 78 - Sensitivity vs Time, S/N 63

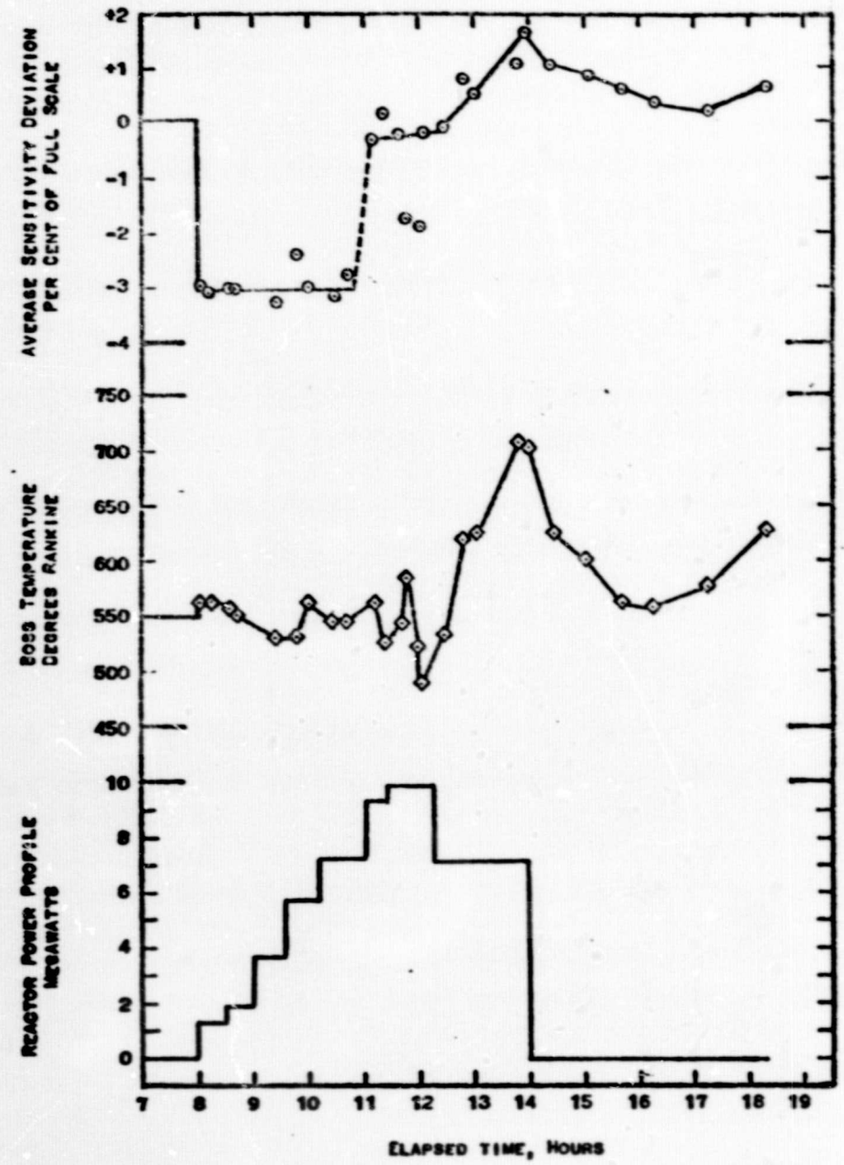

Figure 79 - Correlation of Average Sensitivity Deviation, Boss Temperature and Reactor Power Profile

and the reactor-power profile that corresponds to the relative gamma rates of the test. The effects of the temperature perturbations on the sensitivity can be readily observed. However, no correlation appears to exist that would cause the decrease in sensitivity. Correlation of the reactor power level and the sensitivity also shows a lack of gamma-rate dependency of the observed change.

With regard to the radiation environment, the recovery of all sensitivities coincidentally occurs at gamma and neutron fluences of 1×10^{11} ergs/gm(C) and 1×10^{17} nvt (E>1.0 Mev) respectively.

5. Zero Shift

The effects of nuclear radiation on the zero-point stability of each transducer were investigated by comparing the zero-pressure output value of successive calibration cycles with the pretest average and expressing the difference as a percent deviation of the pretest full-scale output of each transducer. The resultant reduced data are shown in Figures 80, 81, 82, and 83 for S/Ns 47, 50, 61, and 63 respectively.

The zero-shift curves for the four transducers are uniquely different from each other, indicating varying degrees of response to the test environment. The observed zero-shifts reflect the summation of individual contributing factors, the major ones being:

a. Cable-generated emfs
b. Gamma-gradient generated voltages
c. Strain gage thermal sensitivity
d. Neutron damage

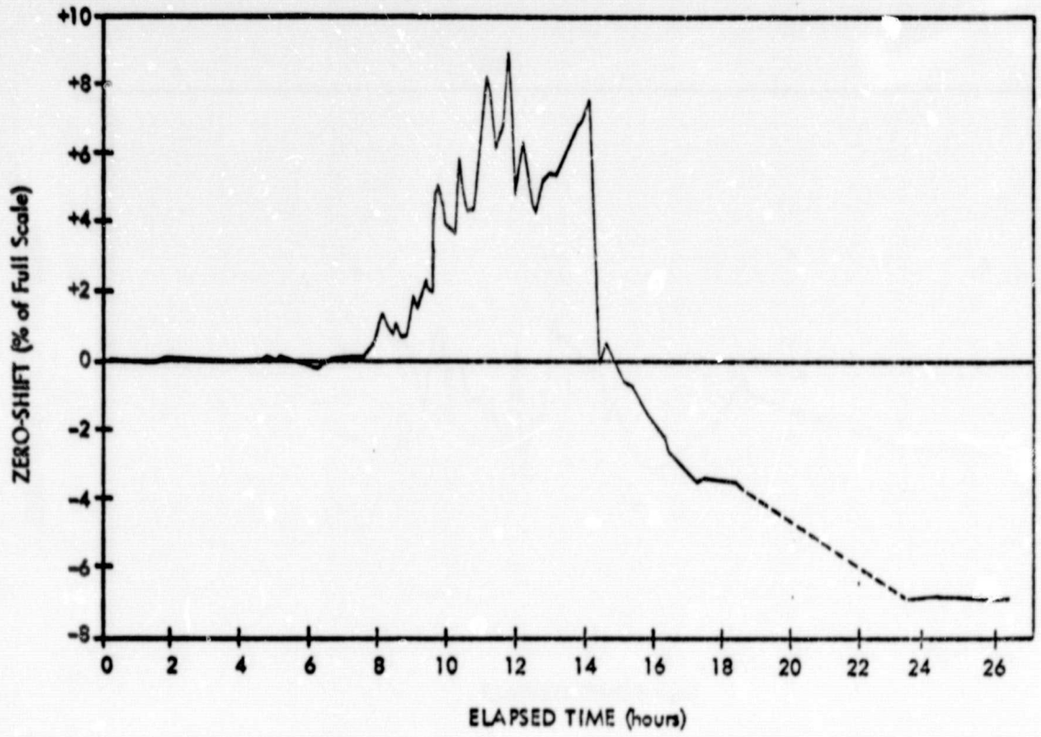

Figure 80 - Zero-Shift vs Time, S/N 47

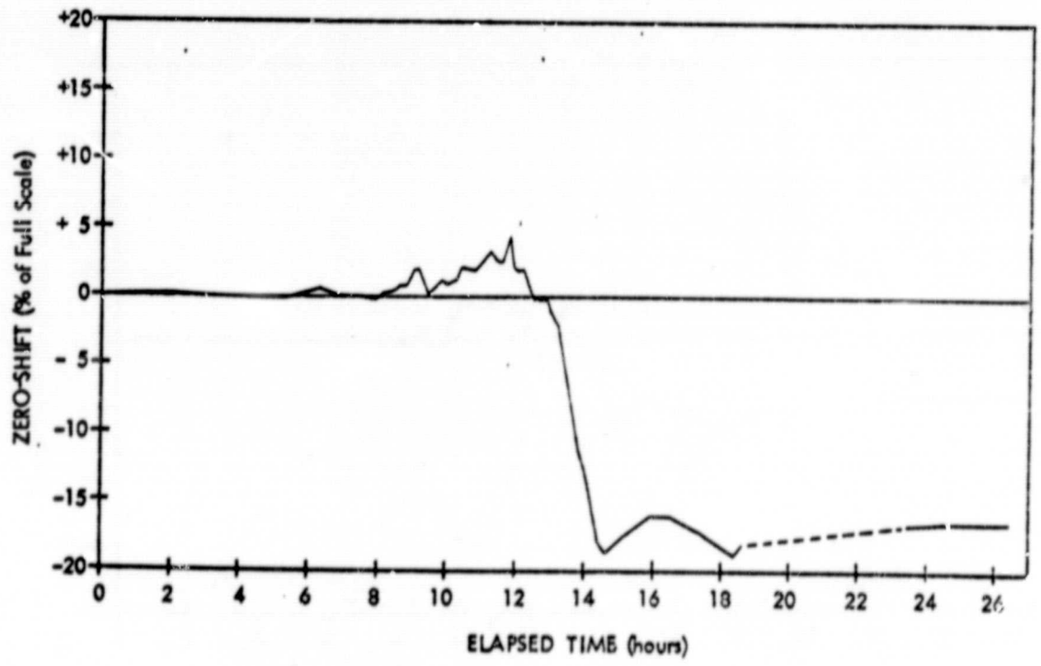

Figure 81 - Zero-Shift vs Time, S/N 50

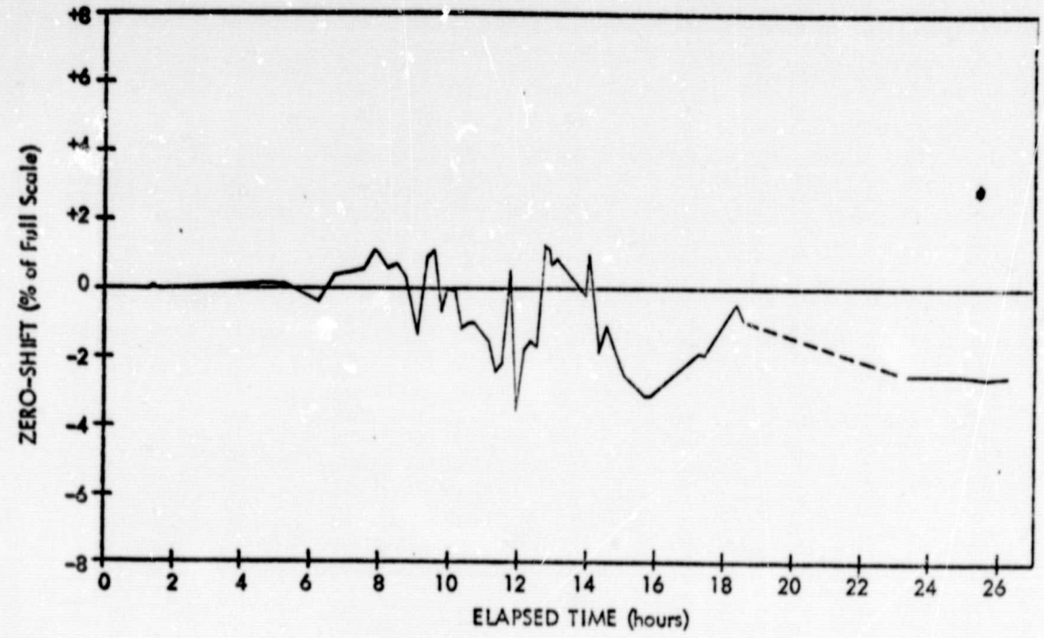

Figure 82 - Zero-Shift vs Time, S/N 61

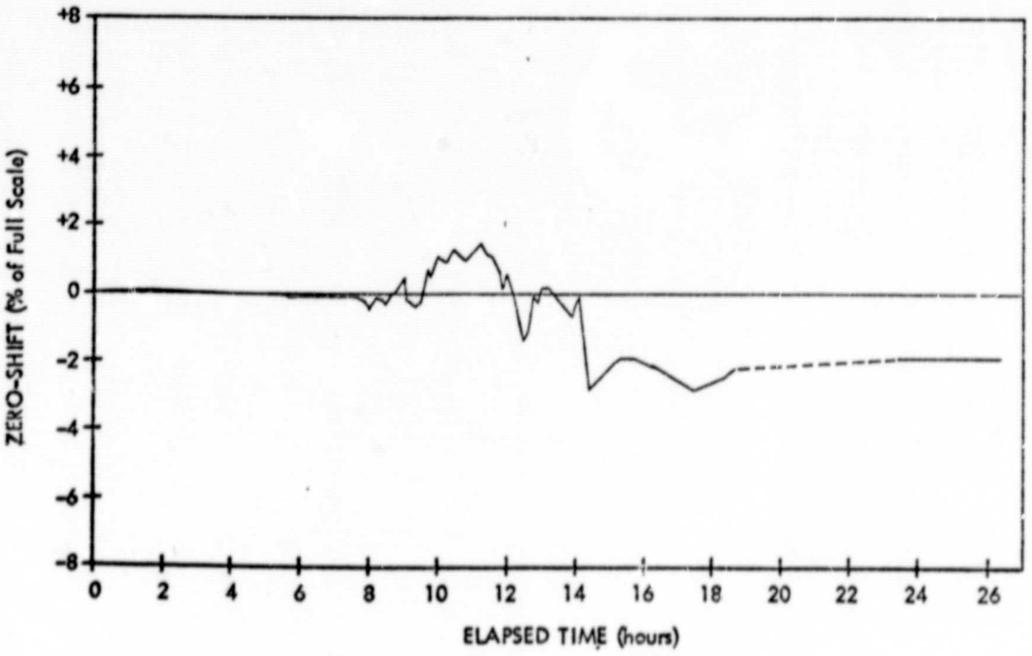

Figure 83 - Zero-Shift vs Time, S/N 63

a. Cable-Generated Emf's

The output error voltage generated by the nickel-cladding on the copper conductors was discussed previously. The error voltage was subtracted from the output voltage of S/Ns 47, 50, and 63, and added to the output of S/N 61. In effect, for three of the transducers, the generated emf acted as a form of temperature compensation, reducing the total zero-shift value. However, for S/N 61 the emf added to the output increased the zero-shift value. Zero-shift data from part 1 of the test was corrected for the cable emf error in the subsequent analysis by adding or subtracting the emf values from Table 14 from the averaged zero-shift error values determined for each of the gamma-rate hold periods.

b. Gamma-Gradient Generated Errors

In the pretest electrical analysis of the transducer, the presence of temperature gradients from the center to the edge of the diaphragm will generate an output voltage that is proportional to the temperature gradient and the temperature coefficient of resistance (TCR) of the strain material. The higher temperature at the center of the diaphragm will cause a larger increase in resistance in the tension arms of the bridge than in the compression arms that are located near the edge of the diaphragm. By design, a positive increase in the tension arm resistances will produce a positive output signal. The magnitude of the error signal will be proportional to the TCR of the bridge and the temperature gradient.

Representative zero-shift values during the respective heating-rate holds in part one of the tests were determined by averaging the data for 5 to 15 successive data cycles for each of the transducers. The resultant values are tabulated in Table 17 and are shown in Figure 84 as a function of the corrected gamma heating rates from Table 7. Gamma correlation is used because the temperature gradient across the diaphragm could not be

measured for the active transducers but would be proportional to the different gamma-rate levels for each transducer location. Also shown is the pretest prediction for S/N 47.

TABLE 17

AVERAGE ZERO DEVIATIONS
(PERCENT FULL-SCALE OUTPUT)

Reactor Power Level (MW)	Transducer S/N 47	S/N 50	S/N 61	S/N 63
1.3	—	0.35	—	0.12
1.98	0.87	0.80	0.08	0.19
3.62	1.79	1.08	0.15	0.28
5.83	4.19	1.77	0.26	1.21
7.3	5.39	2.85	-1.04	1.71
9.4	8.21	3.89	-1.62	1.73
9.9	7.45	3.79	-1.47	0.74

The S/N 47 predicted output error assumed a simplified linear relationship between the increase in tension-arm resistance and temperature gradient. Comparing the S/N 47 zero-shift curve with the prediction shows that the output error is much less than predicted and obviously not a linear function of the heating rate (temperature gradient). The distribution of the output curves is as expected and corresponds to pretest TCR values of 0.000024, 000016, 0.000006, and 0.000002 ohms per ohm per degree Rankine for S/Ns 47, 50, 63, and 61, respectively. All curves also show an abrupt change in profile between the last two data points that correspond to the 9.4 and 9.9 MW reactor power levels. A similar change can be seen between the last two data points in Figure 39 that represent the temperature gradient across the diaphragm in the Boss 4 instrumented transducer. It is believed that the observed changes are attributed to a decrease in the diaphragm gradient caused by heat

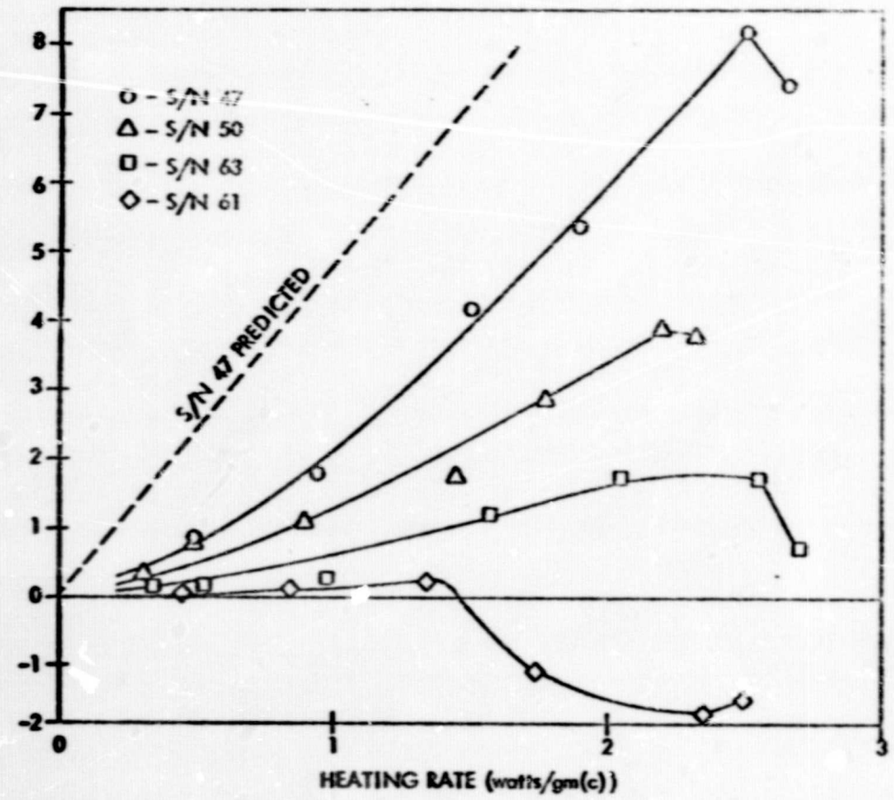

Figure 84 - Zero-Shift vs Heating Rate

loss to the pressurizing gas. S/Ns 61 and 63 curves both show changes between 1.5 and 2.5 watts/gm that are apparently neutron damage related. The observed changes in the curves indicate that the zero balance point of the transducers changed.

Since the distribution of the data for the four transducers appears uniform and correlates well with the TCR distribution of the transducers, the data were input into a multiple regression and correlation analysis computer program to determine if a mathematical relationship existed between the observed zero shift, the heating rate and the transducer TCR. The results of the program indicate that a correlation coefficient of 99.4% exists between the variables and that the observed zero-shift can be expressed mathematically by the following expression:

$$Z = [0.00738 + 0.3853\ (\gamma) + 21079\ (TCR) + 22865\ (\gamma \cdot TCR)]^{2} \quad (1)$$

where: Z = Zero-shift in percent of full-scale output
TCR = Temperature coefficient of resistance
γ = Heating rate in watts/gm (C)

c. Thermal Sensitivity

Although the thermal sensitivity of the bridge is a function of the TCR of the bridge material, it is more indicative of the initial bridge balance. Ideally, if all four arms of the bridge are equal in resistance, the increase in resistance, due to temperature, would be balanced with no resultant change in output. Since the arms of any bridge are not exactly equal, small unequal increases in resistance result in a change in output with temperature, that may be either positive or negative depending upon the relationship of the changes in the arms of the bridge to each other.

An anomaly in the data involves the apparent thermal sensitivity of the transducers during the test. S/Ns 47, 61, and 63 exhibit positive thermal sensitivities during the variable temperature portion of the test. However, only S/N 61 exhibits a positive sensitivity during the post-test period. Pretest calibration data show a negative sensitivity for S/N 47 and positive sensitivities for S/Ns 61 and 63. During the posttest period, S/N 63 sensitivity appears to have changed to negative. Only S/N 50, that exhibited a pretest negative thermal sensitivity, indicates a negative value throughout the test.

From the test results it is concluded that pretest thermal sensitivity data is of little value for the purpose of correcting test data for observed temperature shifts. The thermal sensitivities of the transducers are influenced by the presence of internal temperature gradients and changes in the transducer TCR caused by neutron-related bridge-material changes.

d. Neutron Damage

The data in Figures 80 to 83 show that all four transducers exhibit a change in the zero balance after the test. The zero-balance change, called the zero-set, is a permanent change in the transducer characteristics and differs from the previously discussed zero-shift mechanisms that were transient in nature. The time when an obvious zero-set change occurs is not consistent for the four transducers but does appear to have a relationship to the TCR value for each transducer. In Figure 80, S/N 47 shows that the change occurred very near the end of the test and continued through the first posttest period. Whereas in Figure 81, S/N 50 exhibits a major change occurring at the beginning of the variable temperature portion of the test with equilibrium attained before the first posttest period. In Figure 84, S/N 63 and 61 show the change occurring during the variable heating rate portion of the test, after the 7.3 and 5.83 MW reactor power level holds,

respectively. The consistency exhibited is that the smaller the TCR of the transducer, the sooner the zero-balance change occurs. Interpolated neutron fluences and TCR values for the four transducers at the time the change occurs are noted as follows:

Transducer	TCR	Neutron Fluence (E>1.0 MEV)
S/N 47	0.000024	5.7×10^{17} NVT
S/N 50	0.000016	3.3×10^{17} NVT
S/N 63	0.000006	1.7×10^{17} NVT
S/N 61	0.000002	1.3×10^{17} NVT

Based on the limited data from the four transducers, the threshold damage level appears to be a function of the fast neutron fluence instead of the thermal neutron fluence. Figure 85 shows the threshold levels plotted as a function of the transducer TCR values. The correlation between TCR and threshold damage level is given by the following expression for the interval of 1 to 10×10^{17} n/cm^2 (E > 1.0 Mev):

$$\phi t = 1.14 \times 10^{17} e^{6.7 \times 10^{4} TCR} \qquad (2)$$

where: ϕt = neutron fluence (E > 1.0 Mev) n/cm^2

TCR = temperature coefficient of resistance ohms/ohms/°F

The damage mechanism associated with the TCR and threshold level appears to be caused by a fast-neutron induced chemical reaction. Change in other transducer characteristics such as bridge resistance and sensitivity appear to be dependant on the thermal neutron flux.

The final posttest zero-set values for the four transducers are:

S/N 47 -6.85% of full-scale output
S/N 50 -16.50 of full-scale output
S/N 61 -2.61 of full-scale output
S/N 63 -1.91 of full-scale output

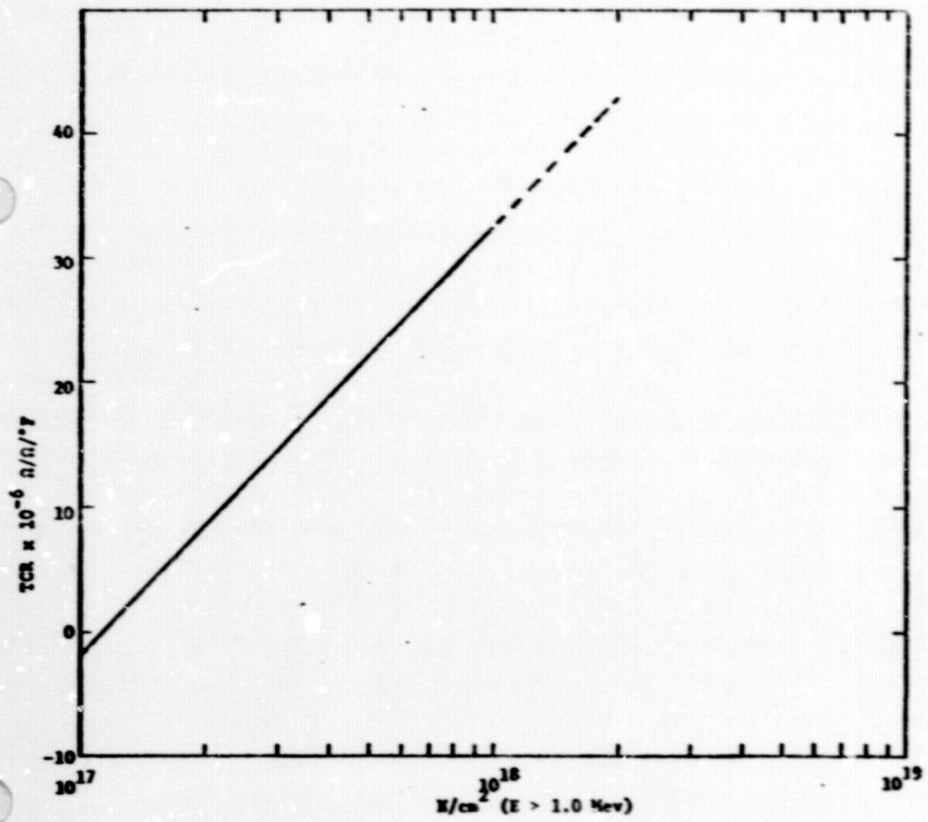

Figure 85 - Threshold Level - Neutron Related Change

VI. CONCLUSIONS

Data obtained during the ASTR 23/K512 test were good, and enabled good resolution and correlation of radiation effects for various transducer and system performance characteristics. Amended heating-rate data provided by CD/FW significantly improved the correlation of nuclear heating-rate effects on transducer performance. All primary and secondary test objectives were met with the exception of the determination of operating temperature extremes at 2 watts/gm(C) and the verification of the transducer analytical thermal model.

A. PRIMARY OBJECTIVES

1. Gamma-Rate Effects

The most significant gamma-heating effect was the presence of excessive zero-shift errors in all transducer outputs during the test. The cause of the zero-shift error is known to be a function of the temperature gradient between adjacent arms of the bridge and the TCR of the strain material. However, the observed zero shifts were nonlinear and less than pretest predictions, that assumed a simplified relationship between the nuclear heating rate and the transducer TCR characteristic. The developed expression (equation (1)) pg. 156 correlating the parameters of zero shift, nuclear heating rate and transducer pretest TCR is a significant result of the test. The expression provides a means for predicting zero-shift error for an engine mounted transducer based on the pretest TCR value and the anticipated nuclear heating rate. Secondly, the correlation can be used to generate limits on transducer specifications to minimize nuclear heating errors.

Gamma-rate effects were also observed in the input and output bridge resistance measurements of each transducer. The divergence between the two parameters during the test was an unexpected phenomenon that appears to be a function of the nuclear heating rates and the transducer TCR values. The

data obtained are inconclusive as to the direct effects of the divergence of the bridge-resistance values but because of the dependency on the TCR value it may be a contributing factor to the nonlinearity of the zero-shift error.

Transducer insulation resistance values, that are also gamma-rate dependent, decreased during the test as expected but were greater than 1 megohm at the maximum heating rate of 2.8 watts/gm(C). The effect of the decreased resistances could not be distinguished in the output data. Although the insulation resistance values are dependent on the irradiation temperature and gamma rate, a third factor appears to be present that accounts for the threefold increase in resistance values of the S/N 61, 63 group compared to the S/N 47, 50 group at the maximum gamma rate.

2. Neutron-Damage Effects

Neutron-damage effects were observed in all posttest transducer characteristics. Since the measured transducer characteristics are indicative of the vapor-deposited strain-material composition it can be concluded that the material composition of the strain bridges were altered through transmutation and fast-neutron damage. The net changes in the transducer characteristics were less than 1% and did not produce significant output errors with the exception of the transducer zero-sets. The zero point is indicative of the bridge balance and small inequalities in the arms are readily observable. The neutron-damage effects were beneficial, as evidenced by the improvement in linearity, as well as degrading to the transducer performance.

The threshold damage level of the transducers appears to be dependent on the TCR value of the transducer within the fast neutron fluence range of 10^{17} to 10^{18} n/cm^2. Based on the limited data from four transducers, the threshold damage level appears to be a function of the fast neutron fluence instead of the thermal neutron fluence. The developed expression (equation (2)) correlating the threshold damage fluence with the transducer TCR value implies

that the radiation tolerance level of the transducers can be significantly improved by increasing the TCR value. However, it would be hazardous to extrapolate the data beyond the 10^{18} n/cm^2 limit based on the data from four transducers.

The gamma and neutron effect on thin-film transducers can be controlled by manufacturing the transducer with a TCR that permits the level of threshold damage to be above 10^{17} n/cm^2 yet not be too large to cause a large zero shift due to gamma heating. Transducers can be tailored made with low TCR's for high gamma flux and low-neutron fluences or with a high TCR for high neutron fluences and low gamma-flux rates. A TCR value can be selected to optimize the transducer to best fit the operating requirements.

3. Operating Temperature Extreme

The transducers were evaluated at 100°F, 200°F and 300°F at 2 watts/gr(C). The ASTR test facility had a limitation of 40 megwatt-hr and time did not permit test at higher temperatures. Temperature limitations of the transducers could not be determined from the limited data obtained.

B. SECONDARY OBJECTIVES

1. Cable shunting effects on transducer performance were minimal due to cryogenic cooling of the cable during the test. However, at high temperature (600°F) the shunting effect can introduce a significant error in the transducer. The shunting can be minimized by incorporating a shunt resistance in the signal conditioner, lower than any expected cable shunting value. Precalibrating the transducer with the built-in shunt will permit a wider temperature variation on the sheath cable without introducing appreciable error in the transducer data.

2. Radiation induced photo currents in the transducer and cable can be eliminated by monitoring voltage on the bridge continuously during the test, or by allowing sufficient data sampling time to stabilize the excess charge on the instrument system.

3. Conductor orientation was important in this test since two double-conductor sheath cables were used. A symmetrical shunting of the bridge occurred when two double-conductor sheathed cables were used. It is recommended that either four single-conductor sheath cables or a single four-conductor sheath cable be used to obtain the minimum shunting effect.

REFERENCES

1. RN-S-0291, Evaluation of Test Results for Strain Gages and Pressure Transducers, Ground Test Reactor (GTR) Irradiation Test No. 15, Aerojet-General Corporation, Sacramento, California, July 1966.

2. RN-S-0369, NRX-A5 Qualification Test of Engine Mounted Pressure Transducers, Aerojet-General, NERVA Program Contract SNP-1, July 1967

3. RN-S-0325, Final Data Report, Strain Gage Pressure Transducer Experiment 23/R511, Aerojet-General, NERVA Program, Contract SNP-1, February 1967.

4. RN-S-0406, Revision A, Final Test Specification, Pressure Transducer Test for General Dynamics-ASTR Facility (23/R512), Aerojet-General Corporation, NERVA Program, Contract SNP-1, 8 August 1967.

5. FZK-343, Mapping of the Radiation Field Within the In-Pile Tube of the Aerospace Systems Test Reactor, General Dynamics, Fort Worth Division, 15 November 1967.

6. RN-TM-0556, Radiation Mapping of the ASTR In-Pile Irradiation Facility with Thermoluminescent Dosimetry, Aerojet-General Corporation, NERVA Program, Contract SNP-1, November 1967.

7. FZK-344, NERVA Irradiation Program, ASTR In-Pile Tube Test 1, Pressure Transducers (Test 23/R512A), General Dynamics, Fort Worth Division, 26 February 1968.

8. FZK-344, Addendum, NERVA Irradiation Program, ASTR In-Pile Tube Test 1, Pressure Transducers (Test 23/R512A), General Dynamics, Fort Worth Division, 2 December 1968.

9. Huth, Gerald C., Conductivity Induced in Solid Insulating Materials During Gamma Irradiation, General Electric Company, Aircraft Nuclear Propulsion Department, Cincinnati, Ohio, Report 58-331.

10. Glasstone, S. and Sesonske, A., Nuclear Reactor Engineering, D. Van Nostrand Company Inc., p. 47.

APPENDIX

HEAT TRANSFER ANALYSES

I. INTRODUCTION

Thermal analyses were performed to predict the temperature distributions and associated cooling requirements for flush-mounted, Statham, pressure transducers. These analyses were performed in two iterations using two different computer codes. Initially, Job 2785[1] was used to determine flow rates and temperature distributions in the 23/R512 test fixture. Concurrently, FEM[2], an alternate heat transfer analytical code, was being made operational. Subsequent to the Job 2788 work, a final analytical iteration was performed using FEM.

With these methods, cooling requirements to hold transducer boss temperatures to 100°F for gamma heating rates of up to 4 watts/gm were determined (100°F is the estimated pressure-transducer-boss temperature on the XE Engines). When flow rates and pressure drops compatible with existing or obtainable on-site test equipment were determined, temperature distributions in the transducer were calculated and found to be acceptable. Based on this analytical information, the test-fixture design was finalized and the test fixture was fabricated. The irradiation test was performed in August, 1967. Using a variety of thermocouples located on the transducers and test fixture, temperature data were obtained during the test. The temperature data obtained will be compared to the analytical data in the text. Because of the bulk and extent of the data, comparisons will be made at selected heating rates with anomalies noted and explanations attempted.

(1) Network Generator and Thermal Analyses. The steady state heat transfer analysis by finite difference method.
(2) Finite Element Analysis. The steady state heat transfer analysis by finite element method.

II. DISCUSSION

In the following section, discussions concerning test fixture thermal design requirements, coolant system design requirements, and predicted and measured temperature distributions are presented.

A. ANALYTICAL TEMPERATURE DATA

Based on analyses, the following thermal-system requirements were specified.

1. Mode of Cooling

The coolant used for the test was cold GN_2. A source of LN_2 was available at the test facility. However, pretest analysis indicated that if LN_2 were used as the coolant, it would be in the film-boiling region in the test fixture. This situation was undesirable since heat transfer in this region is difficult to predict and to control. It was necessary to install a heat exchanger, or evaporator, upstream of the test fixture in order to vaporize the LN_2 to produce cold GN_2 prior to entering the test fixture.

The evaporator utilized water as the heat source in a single-pass parallel-flow unit 44-ft long. The nitrogen flowed through a 2.75-in. dia aluminum tube located concentrically within the 4-1/2 in. dia aluminum water tube. The nitrogen was forced through the inner pipe by storage tank pressure and, when required, by a 100 gpm, 265 psig centrifugal pump.

2. Pressure-Drop Analysis

A detailed pressure-drop and heat-balance analysis was performed on the cooling fluid for the 2 and 4 watt/gm(C) gamma heating-rate conditions. In this analysis, the nuclear heating was assumed constant for all of the test

fixture, and the inlet and outlet plumbing within the reactor at 2 and 4 watt/gm(C), respectively. For the inlet and outlet plumbing outside of, and within one foot of the reactor, a value of 1/2 of the nominal heating rate was used, i.e., 1 and 2 watt/gm(C). For all other plumbing, no nuclear heating was considered. It was further assumed that all nuclear heating of the test fixture, transducers, and associated plumbing was removed by the coolant fluid. The equivalent length of 23 ft was assumed for the portion of the exhaust piping outside the reactor (included fittings and bends, of two parallel, 1-in. OD x 0.035 in.-thick wall, 6061 aluminum tubes). Several computer runs were made holding flow rate and heating rate constant, and varying inlet pressure and temperature to the test fixture (inlet temperature equal to saturation temperature for the corresponding pressure), to determine the minimum inlet pressure.

3. Temperature Distributions

The temperature distributions predicted initially at 2 and 4 watts/gm(C) of gamma heating using computer Job 2788 are shown in Figures 1 and 2. Pertinent locations are the transducer boss, center, and edge of the transducer diaphragm, and the center of the outside surface of the hexagonal heat of the transducer. These locations correspond to the thermocouple locations on the test fixture.

Figures 3 and 4 list the temperatures obtained at 2 and 3 watts/gm(C) using FEM. A maximum of 3 watts/gm(C) was used to be consistent with the gamma mapping run, subsequent to the 2788 analysis but prior to the FEM analysis, that showed a maximum capability of approximately 3 watts/gm(C) at ASTR.

In Figure 1, the 2 watt-per-gram heating rate, of the 2788 values correspond well (±20°R) with the FEM values (Figure 3) at the boss, and the center and edge of the diaphragm. However, the hex-head temperatures show a discrepancy of approximately 180°R.

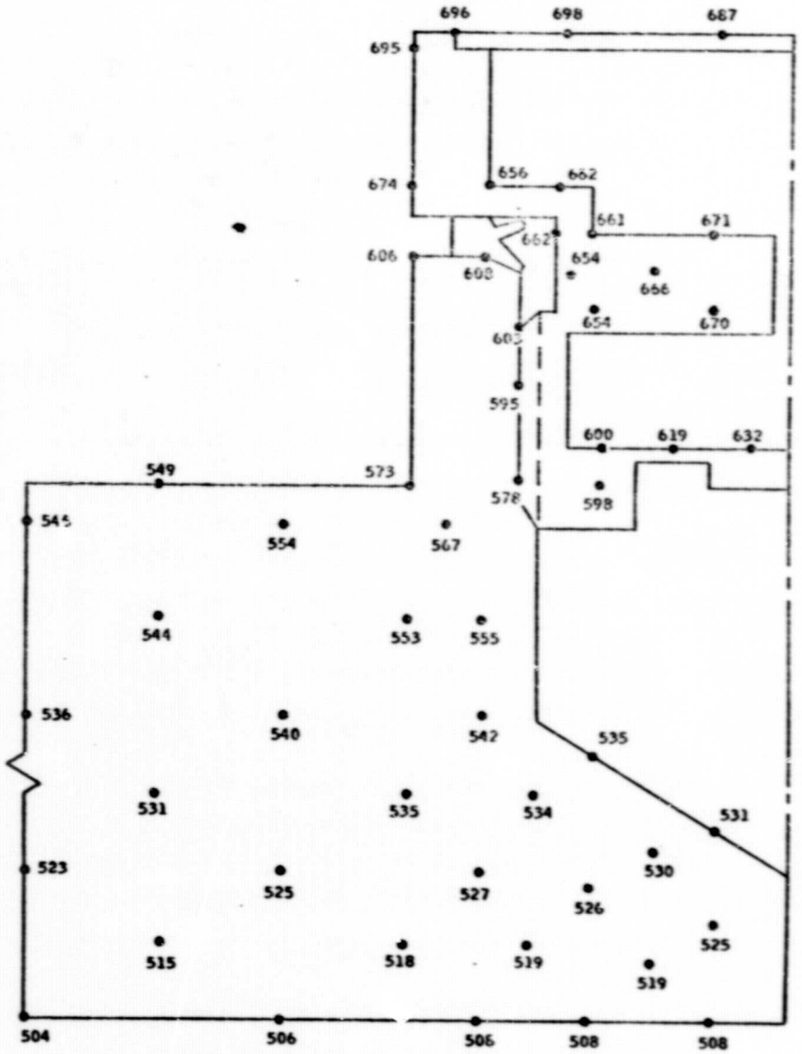

NOTES:
1. TEMPERATURES, °R
2. STEADY STATE
3. COOLANT FLOW RATE = 1.87 LB/SEC N$_2$

Figure 1 - Temperature Distribution Flush-Mounted Pressure Transducer Irradiation Test Conditions, 2 Watts/gm(C)

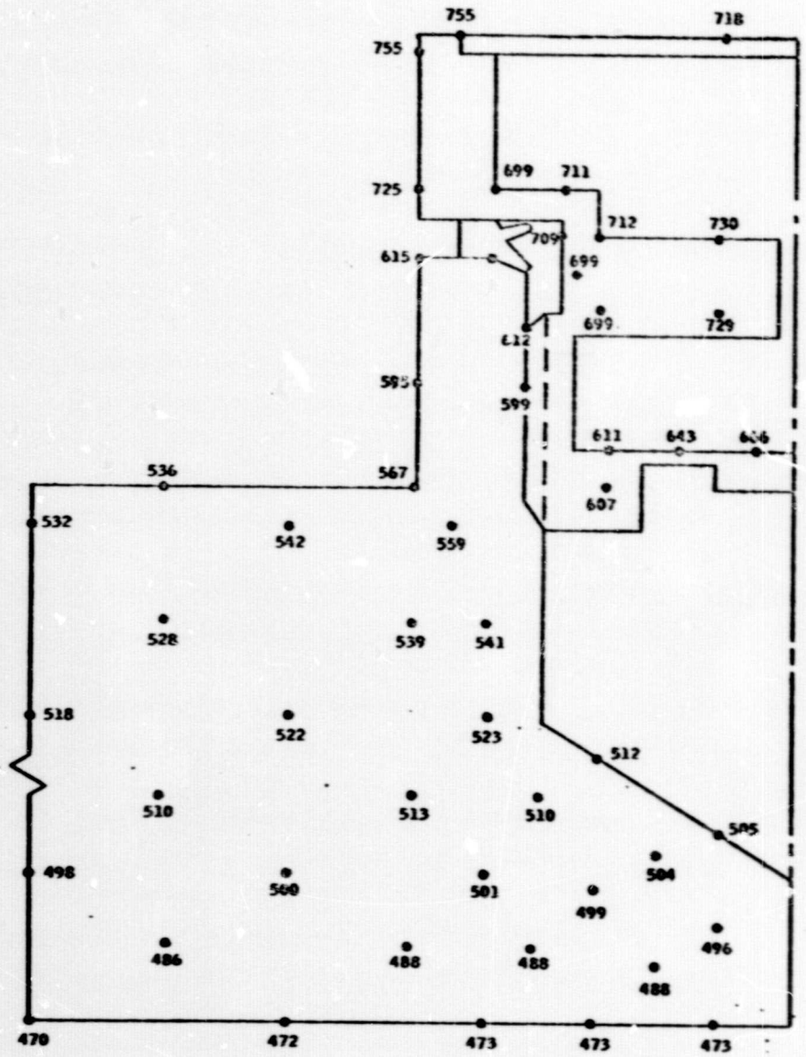

NOTES:
1. TEMPERATURES, °R
2. STEADY STATE
3. COOLANT FLOW RATE = 3.42 LB/SEC H_2

Figure 2 - Temperature Distribution Flush-Mounted Pressure Transducer Irradiation Test Conditions, 4 Watts/gm(C)

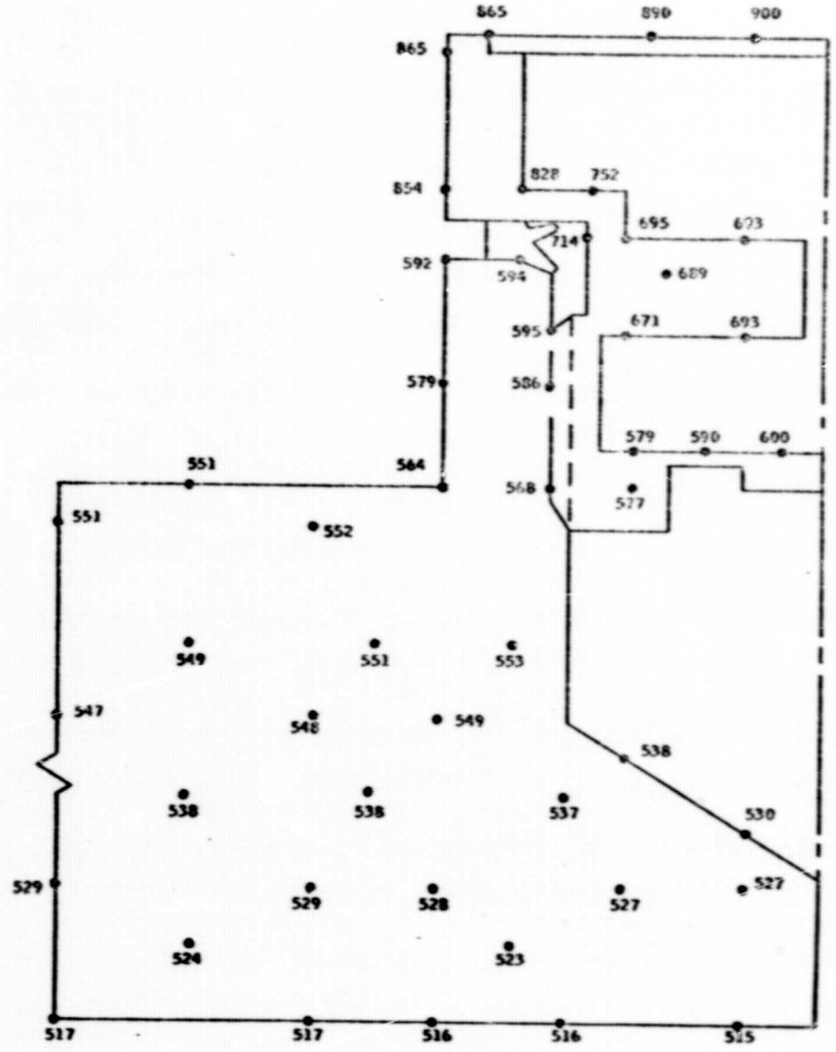

NOTES:
1. TEMPERATURE, °R
2. STEADY STATE
3. COOLANT FLOW RATE = 1.41 LB/SEC

Figure 3 - Temperature Distribution Flush-Mounted Pressure Transducer Irradiation Test Conditions, 2 Watts/gm(C) Run No. 2

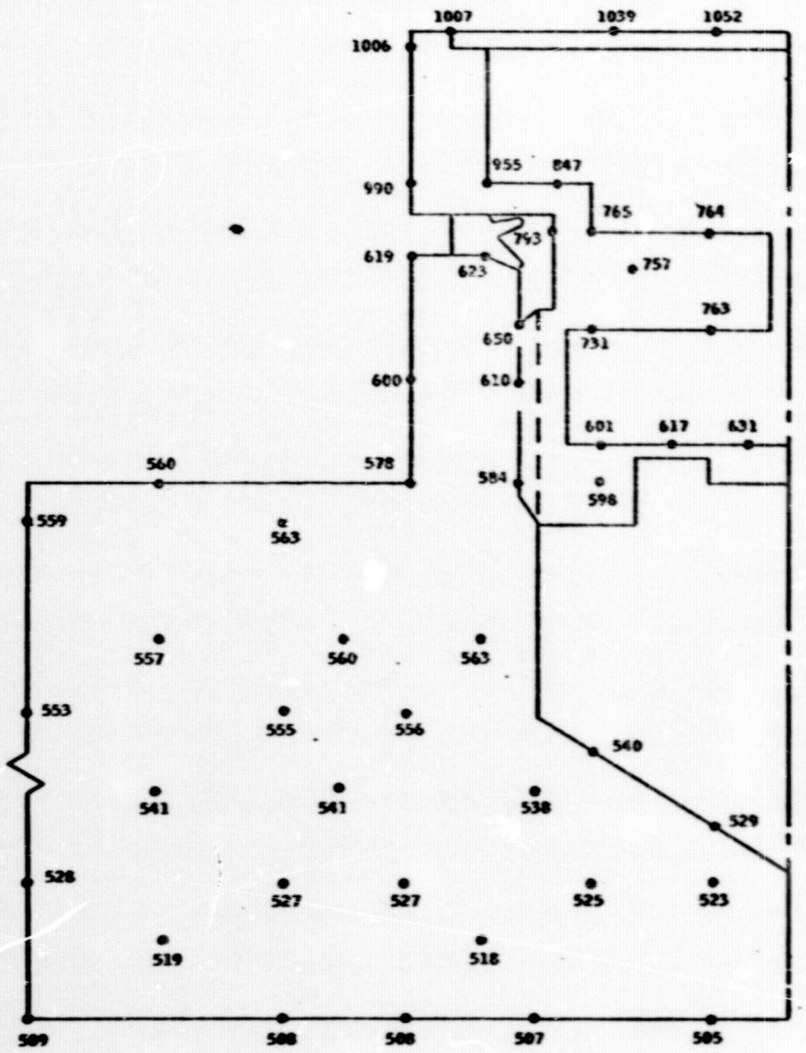

NOTES:
1. TEMPERATURES, °R
2. STEADY STATE
3. COOLANT FLOW RATE = 2.7 LB/SEC

Figure 4 – Temperature Distribution Flush-Mounted Pressure Transducer Irradiation Test Conditions, 3 Watts/gm(C)

This discrepancy is attributed to th inadequacy of the 278B computer code. A shortcoming of 278E is that it is a finite difference iterative type code, and does not work well with small mesh points and small delta's in temperature from one mesh point to the next. As the distance from the coolant increases, the treatment of conduction in the model is paramount. FEM is also an iterative code, but uses an entirely different and much more accurate approach. Since FEM results are believed to be more accurate than 278B, analytical and measured comparisons will be made using FEM temperature values.

4. Required Coolant Flow Rates

A series of two-dimensional conductive analyses were performed using IBM Computer Job 278B for heat deposition rates of 2 and 4 watts/gm(C) to determine the corrective film coefficient required to produce a temperature of 100°F (560°R) at a thermocouple imbedded in the transducer mounting boss. At least two computer runs were made at each of two heat deposition rates (2 and 4 watts/gm(C)) with varying convective film coefficients to bracket the required value). A final verification run was then made for the two cases. In the analyses the following assumptions were made:

a. Two-dimensional conduction using cylindrical coordinates.

b. Ambient surface of transducer and fixture cooled by thermal radiation with a view factor of 1, an emissivity of 0.3, and a sink-temperature of 125°F (the temperature of the ASTR In-Pile Tube).

c. Uniform heat deposition rates in alumium and steel, i.e., no self attenuation.

APPENDIX

The required coolant flow rate to produce the required convective film coefficient for each heating rate was then calculated, based on test fixture inlet conditions of 100-psia static pressure and 176°R. The following correlation was used for computing the convective film coefficient:*

$$h = 0.036\ K_b/D_h\ (N_{Re})_b^{0.8}\ (N_{Pr})^{0.4}\ (T_w/T_b)^{-0.5}$$

where

h = convective film heat-transfer coefficient

K = fluid thermal conductivity

D_h = hydraulic diameter of coolant channel

N_{Re} = Reynolds number

N_{Pr} = Prandtl number

Subscript b = bulk temperature conditions

Subscript w = wall temperature

Subsequent to the above analyses and after a determination by an in-core mapping run that the In-Pile Tube maximum gamma heating rate was approximately 2.7 watts/gm(C), further analyses using FEM were made at 2 and 3 watts/gm(C). These coolant requirements and the temperature distributions are shown in Figures 3 and 4.

* Simoneau, R. J., and Hendricks, R. J., "A Simple Equation for Correlating Turbulent Heat Transfer to a Gas", NASA TM X-52011, August 1964